
Spin-polarized transport through 2-D quantum materials

Deepti Rana

**A thesis submitted for the partial fulfilment of the degree of
Doctor of Philosophy**



**Department of Physical Sciences
Indian Institute of Science Education and Research Mohali
May, 2024**

**Dedicated to
my papa and mummy**

Certificate of Examination

This is to certify that the thesis titled ‘Spin-polarized transport through 2-D quantum materials’ submitted by Deepti Rana (PH18062) for the partial fulfillment of Doctor of Philosophy programme of the Institute, has been examined by the thesis committee duly appointed by the Institute. The committee finds the work done by the candidate satisfactory and recommends that the report be accepted.

Dr. Goutam Sheet

Prof. Sanjeev Kumar

Dr. Abhishek Chaudhuri

Dated: May, 2024

Declaration

The work presented in this thesis has been carried out by me in the guidance of Dr. Goutam Sheet at Indian Institute of Science Education and Research (IISER) Mohali. This work has not been submitted to any other institution or university in part or in full for a degree, a diploma, or a fellowship. Whenever contributions of others are involved, every effort is made to indicate this clearly, with due acknowledgment of collaborative research and discussions. This thesis is a bonafide record of original work done by me and all sources listed within have been detailed in the bibliography.

Date:

Place:

Deepti Rana (PH18062)
(Candidate)

In my capacity as the supervisor of the candidate's doctoral thesis, I certify that the above statements by the candidate are true to the best of my knowledge.

Dr. Goutam Sheet
(Supervisor)

Acknowledgements

As I reach the culmination of my Ph.D. thesis work, I would like to take this chance to express my sincere thanks to people who have played a significant role in the last five years.

I would like to begin by expressing my gratitude toward my thesis supervisor, Dr. Goutam Sheet, for his unwavering support. I am honored to have worked under his supervision. I am grateful to him for providing the best low-temperature experimental facilities possible and for giving me the opportunity to work on exciting theoretical problems along with my experimental projects. Dr. Sheet consistently welcomed discussions and patiently addressed all my inquiries. His dedication, tireless efforts, and scientific rigor have always inspired and motivated me to go that extra mile. I sincerely acknowledge his genuine concern for the well-being of his students. I am indebted to him for his support and valuable guidance.

I would like to thank my doctoral committee members Dr. Sanjeev Kumar and Dr. Abhishek Chaudhuri for their insightful comments and suggestions that helped me improve. I would also like to express my gratitude towards my collaborators Dr. R.P. Singh (IISER Bhopal), Dr. Mukul Kabir (IISER Pune), Dr. Mintu Mondal (IACS Kolkata), Prof. G.U. Kulkarni (JNCASR Bangalore) and Dr. Sanjeev Kumar (IISER Mohali) for their contribution to my research.

I want to thank my SpIN lab members, Dr. Anshu Sirohi, Dr. Aastha Vasdev, Dr. Soumyadip Halder, Dr. Ritesh Kumar, Sandeep Howlader, Dr. Shekhar Das, Dr. Soumya Datta, and Dr. Suman Kamboj for helping me learn the art of scanning probe microscopy. I thank Mona Garg, Nikhlesh Mehta, Mohd. Monish, and Ghulam Mohammad for being very helpful. Their determination kept me motivated in the lab. I want to thank Monika Bhakar for being a good friend. I want to thank Dr. Monika Moun and Dr. Pooja Bhardwaj for being so encouraging and the MS project students, Aswini, Anmol, Neeraj, Nikhil, Ranjini, Sandra, and Shivam for their help during the experiments.

I made few but special bonds during the last five years. I thank Shivam, Aswini, and Shubham for being good friends. I want to thank Taseng for the cheerful moments. I want to thank Anshika, immensely, for being the driving force throughout. She was my pillar of strength during the challenging times and my greatest cheerleader during the happy times. I thank her once again for taking care of me like her family. It is possible to conquer anything if you have good company by your side. I want to thank them for making IISER feel like home on most days. Special mention to Julie and her family for always accompanying me to the hostel when I used to come late from the lab.

I spent some of the best moments of my life at Panjab University with my four friends Parit, Simran, Anshu, and Pankaj. I thank Parit for his constant support. I thank Simran and Anshu for their love. I thank Pankaj for helping me stay confident. I really appreciate everything they have done for me. I would also like to thank Payal Di, whom I met during

my short stay at IIT Ropar, for always being a well-wisher.

I would finally like to acknowledge my family who have always encouraged me to follow my dreams. They have supported every decision of mine. I have learned the importance of learning from my father's immense passion for books. He has been a great mentor and has played a pivotal role in shaping my journey. Equally influential, my mother has taught me the meaning of perseverance which helped me a lot during my research. I am grateful for their motivation and blessings. Next, I thank my two lovely sisters, Preeti and Samriti, for always showering me with lots of love. They have encouraged and inspired me in many ways. I love my little rays of sunshine-my nieces: Vedica, Kimrit, and Gargi. A little thanks to myself as well for keeping on going when the clouds were grey.

List of publications:

1. Tunneling characteristics of weakly coupled Majorana wire arrays ,
Deepti Rana and Goutam Sheet, *Journal of Applied Physics* **131**, 084301 (2022)
2. Spin-polarized supercurrent through the van der Waals Kondo lattice ferromagnet Fe_3GeTe_2 ,
Deepti Rana, Aswini R, Basavaraja G, Chandan Patra, Sandeep Howlader, Rajeswari Roy Chowdhury, Mukul Kabir, Ravi P. Singh, and Goutam Sheet, *Physical Review B* **106**, 085120 (2022).
3. Fully gapped type-II superconductivity in Pt-doped IrTe_2 near critical doping,
Aastha Vasdev, **Deepti Rana**, Amit Vashist, Yogesh Singh, and Goutam Sheet, *Physical Review B* **105**, 094509 (2022).
4. Weakly coupled Majorana wire arrays under tilted magnetic fields,
Deepti Rana and Goutam Sheet, *Journal of Applied Physics* **133**, 224301 (2023).
5. High transport spin polarization in the van der Waals ferromagnet Fe_4GeTe_2 ,
Deepti Rana, Monika Bhakar, Basavaraja G., Satyabrata Bera, Neeraj Saini, Suman Kalyan Pradhan, Mintu Mondal, Mukul Kabir and Goutam Sheet, *Physical Review B* **107**, 224422 (2023).
6. Skyrmions and ferromagnetic bubbles in spin-orbit coupled itinerant magnets,
Deepti Rana, Soumyaranjan Dash, Monika Bhakar, Rajeshwari Roy Chowdhury, Ravi Prakash Singh, Sanjeev Kumar, and Goutam Sheet, *Physical Review B* **108**, 184419 (2023).

Abstract

Due to the growing demand for the miniaturization of electronic devices, there is an urgent requirement to develop novel materials that can facilitate the design of energy-efficient nano-scale electronic circuits. Two-dimensional (2D) quantum materials, owing to their unique electronic properties, have emerged as promising candidates for future electronic devices. Understanding the spin-polarized transport phenomena in these materials is crucial for the development of spintronics, offering potential advantages in spin-based information processing and storage. This thesis investigates the spin-polarized transport characteristics of various 2-D quantum materials through theoretical modeling and low-temperature-based scanning probe techniques.

The thesis is divided into two parts: The first part contains our work on a family of vdW 2-D ferromagnets particularly those with the general formula Fe_nGeTe_2 (where $n=3,4$) which possess desirable characteristics such as large electrical conductivity, a high ferromagnetic Curie temperature, and strong saturation magnetization for application in next-generation spintronic devices. We have investigated the interplay of various quantum phenomena in the aforementioned vdW ferromagnets using low-temperature-based scanning probe techniques. Furthermore, to enable efficient detection of Majorana modes in topological superconductors, crucial for fault-tolerant quantum computing, in the second part of the thesis we have proposed a tunneling setup with weakly coupled Majorana nanowires. The setup offers controlled detection by manipulating the presence of a zero-bias conductance peak (ZBCP) based on wire parity. The major results, procured in this work are highlighted below.

Measurement of transport spin polarization of the vdW ferromagnets Fe_3GeTe_2 and Fe_4GeTe_2 : We performed spin-resolved point contact Andreev reflection spectroscopy of the mesoscopic junctions of these ferromagnets with conventional superconductors. The results revealed a very high degree of transport spin polarization exceeding 50% in both the ferromagnets which is more than the conventional elemental ferromagnets, making them possible candidates for power-saving spintronic devices.

Signatures of Kondo hybridization in Fe_3GeTe_2 and Fe_4GeTe_2 : We investigated the point contact spectroscopic features of the mesoscopic junctions of these ferromagnets with conventional superconductors, in the normal state and over high bias. A temperature-dependent asymmetric double-peak structure in the conductance spectra, indicating the opening of a gap structure, along with characteristic features for a Fano resonance was found. Similar features were observed in the scanning tunneling spectroscopic (STS) measurements establishing a significant role of strong electron correlations leading to a coherent Kondo-lattice state in the ferromagnets.

Stripes and bubbles in Fe_3GeTe_2 and Fe_4GeTe_2 : To study the effect of an external

magnetic field on the local magnetic properties of these systems, we imaged the ferromagnetic domains using low-temperature magnetic force microscopy(MFM). Interestingly, we observed a field-induced transition from a stripy magnetic phase to magnetic bubbles in both the ferromagnets. The MFM results were found to align well with a microscopic model of itinerant 2-D ferromagnets with Rashba spin-orbit coupling and magnetic anisotropy.

Tunneling characteristics of weakly coupled Majorana wire: The experimental detection of Majorana modes in the topological superconductors has yet remained elusive. To address this issue, we have proposed a tunneling setup that consists of an array of weakly coupled Majorana nanowires, which are part of a quasi-two-dimensional topological superconductor. This setup allows for a more controlled and effective detection of these topologically non-trivial modes. In our proposed setup, the presence or absence of the ZBCP can be switched on and off based on the parity of the transport active wires, leading to an odd-even-like effect in the tunneling conductance. This provides a more comprehensive signature of the Majorana modes. Additionally, we have studied the effect of the magnetic field angle on the odd-even effect, where the tilt angle of the magnetic field can serve as another tuning parameter to confirm the Majorana origin of the ZBCP.

Contents

1	Introduction	1
1.1	Two-dimensional materials	1
1.2	vdW magnets	3
1.2.1	Magnetism in 2-D	3
1.2.2	Fe_nGeTe_2	5
1.3	Spin polarization of ferromagnets	6
1.3.1	Point contact Spectroscopy (PCS)	7
1.3.2	Point contact Andreev reflection spectroscopy	10
1.3.3	BTK formalism	11
1.3.4	PCAR as a probe of spin polarization of ferromagnets	14
1.4	Heavy Fermion systems	18
1.4.1	The single impurity Anderson Model	19
1.4.2	Kondo effect	20
1.4.3	Kondo lattice	21
1.5	Topological Superconductivity	23
1.5.1	Majorana Zero energy modes.	24
1.5.2	Kitaev model of topological superconductivity	25
1.5.3	Physical Realization of Kitaev Model	29
2	Experimental Techniques	40
2.1	PCS experimental setup	40
2.1.1	Fabrication of point contacts	40
2.1.2	PCS probe and data acquisition	42
2.2	Scanning Tunneling Microscopy	43
2.2.1	Basic Principles	43
2.2.2	Modes of operation	46
2.2.3	UHV-STM	48

2.3	Magnetic force microscopy (MFM)	52
2.3.1	Modes of operation	53
2.3.2	LT-MFM	55
3	The vdW ferromagnet Fe_3GeTe_2	59
3.1	Measurement of transport spin polarization	60
3.1.1	PCARS on Nb / Fe_3GeTe_2 junctions	61
3.1.2	Bandstructure calculations	63
3.1.3	Emergence of Kondo-lattice behavior in dI/dV spectra	66
3.2	Stripes and bubbles	68
3.2.1	The model	68
3.2.2	MFM results on Fe_3GeTe_2	70
3.3	Conclusion	74
3.4	Contributions	74
4	The near room temperature vdW ferromagnet Fe_4GeTe_2	79
4.1	Sample details	81
4.2	Measurement of transport spin polarization	81
4.2.1	PCARS on junctions of Fe_4GeTe_2 with Nb and Pb	81
4.2.2	Bandstructure calculations	82
4.3	Emergent Kondo lattice behavior in Fe_4GeTe_2	86
4.4	Stripes and bubbles	89
4.4.1	MFM results on Fe_4GeTe_2	89
4.5	Conclusion	90
4.6	Contributions	90
5	Tunneling into a weakly coupled array of Majorana wires	94
5.1	The Model	95
5.2	Tunneling Conductance	98
5.2.1	Tunneling conductance of uncoupled wires:	100
5.2.2	Tunneling conductance of weakly coupled wires:	100
5.2.3	Effect of finite temperature and dissipation	100
5.3	Role of t_y and β in odd-even effect	102
5.4	Relevance of bonding and anti-bonding	104
5.5	μ - V_z phase diagram	105
5.6	Effect of tilted magnetic field	106
5.6.1	Single nanowire	107
5.6.2	Array of nanowires	109
5.7	Conclusion	116

6 Summary	119
6.1 Future Prospects	120

List of Figures

1.1	The progression of 2-D magnetism over the past few decades is shown in a timeline [30].	2
1.2	The diagram illustrates the variation in the preferred spin orientation with different spin dimensionality. In this context, (a) $n = 1$ correlates to the Ising Hamiltonian with strong uniaxial anisotropy, while (b) $n = 2$ and (c) $n = 3$ correspond to systems with easy-plane anisotropy (XY Hamiltonian) and isotropic Heisenberg Hamiltonian, respectively.	4
1.3	(a) Schematic depicting transport through a point contact formed in a ballistic regime ($a \ll l$). (b) The electron distribution in the ballistic regime at the center of the contact is shown.	7
1.4	Point contact studies for a Cu-Cu point contact with a contact resistance of 3.3Ω at a temperature of 1.5K where a) I-V. (b) The differential resistance, $\frac{dV}{dI}$. (c) The second derivative, $\frac{d^2V}{dI^2}$. The dashed curve depicts the phonon density of states, $F(\epsilon)$, obtained through neutron scattering experiments [68].	8
1.5	(a) Schematic showing transport in the thermal regime. The electrons can undergo inelastic scattering within the contact region leading to Joule heating. (b) The FS is shifted slightly by eEl , where E is the applied electric field and l is the mean free path of electrons.	10
1.6	(a) Schematic showing transport in the diffusive regime. The electrons can undergo elastic scattering within the contact region. (b) The process of elastic scattering redistributes the electrons across a spherical region, but this redistribution is limited to an energy shell characterized by a width equal to eV	11
1.7	Schematic showing Andreev reflection in a junction formed between unpolarized ($P_f = 0$) metal and a conventional superconductor.	12
1.8	Evolution of the $\frac{dI}{dV}$ spectrum with change in the value of Z . The conductance at zero bias becomes suppressed with an increase in the value of Z . The other fitting parameters used are $T = 2K$, $\Delta = 1.5 \text{ meV}$, and $\Gamma = 0$	15

1.9	(a) Schematic showing Andreev reflection in a point contact junction formed between fully polarized ($P_f = 100\%$) metal and a conventional superconductor.	16
1.10	PCAR spectra for different values of transport spin polarization P_f and Z .	18
1.11	Schematic depicting the hybridization (screening) of the localized moments (red arrows) with the conduction electrons (blue arrows) in (a) a single-impurity Kondo effect (b) and a Kondo lattice.	21
1.12	Schematic illustrating electron tunneling into a Kondo Lattice where t_c gives the direct tunneling amplitude into the sea of conduction electrons and t_f gives the tunneling amplitude into the composite state made from the hybridization of the localized moments and conduction electrons. Inset shows the typical Fano line behavior observed, in the tunneling conductance, for a Kondo lattice.	22
1.13	(a) For every state E in the superconducting gap there exists a state at $-E$ as a consequence of particle-hole symmetry. (b) The mid-gap excitations of the topological superconductor will lead to a topologically protected unpaired Majorana bound state at zero energy as it cannot be moved away from $E=0$ unless the gap closes.	24
1.14	Schematic illustrating N sites 1-D Kitaev chain, where each fermionic site can host two Majorana modes	25
1.15	Schematic illustrating pairing between Majoranas present at the same fermionic site for the case when $\mu \neq 0, t = \Delta = 0$.	26
1.16	Schematic illustrating pairing of Majoranas at adjacent neighboring sites for the case when $\mu = 0, t = \Delta \neq 0$ leading to unpaired Majorana modes $\gamma_{1,A}$ and $\gamma_{N,B}$ localized at opposite ends of 1-D Kitaev chain	27
1.17	Energy spectrum of Kitaev chain w.r.t to μ plotted for $ \Delta = 1, t=1$. Phase transition between the topological phases taking place at $ \mu = 2t$.	27
1.18	Schematic showing a semiconducting Rashba spin-orbit coupled nanowire lying along x -axis in proximity to an s-wave superconductor. The external magnetic field is applied along the z -axis.	28
1.19	The tunneling conductance setup consisting of Majorana nanowire (in red) connected to the normal leads (in blue) with a barrier potential (in green) existing at the interface of the junction. A bias V is applied to the normal leads.	30
1.20	The differential conductance (in units of $2\frac{e^2}{h}$) for a single nanowire in the topological regime. For calculations, the values used are $\alpha = 1t, \mu = -2t$, and $\Delta = 0.6t, V_z = 0.85 t$.	31
2.1	Schematic illustrating (a) needle-anvil and (b) soft point contact method.	41

2.2	PCS probe head.	42
2.3	Schematic illustrating the point contact spectroscopy data acquisition setup.	43
2.4	Schematic depicting two metal electrodes separated by a barrier of width d and height ϕ . Quantum tunneling of electrons between the two metals happens when a potential difference is established.	44
2.5	Schematic of tunneling from filled sample states to empty tip states when the sample is negatively biased.	45
2.6	(a) A typical schematic of STM illustrating a sharp metallic tip (W or Pt-Ir tip) and the conducting sample positioned a few Angstroms apart using an assembly of piezo-walkers (b)Atomically resolved topograph of $5 \text{ nm} \times 5 \text{ nm}$ area of turbostratic graphene for $V_b= 400 \text{ mV}$ and $I_t=450 \text{ pA}$	47
2.7	The density of states of (a) Pt-doped IrTe_2 , type-II superconductor, recorded at 330 mK . (b) a Kondo lattice ferromagnet Fe_4GeTe_2 recorded at 2K	48
2.8	(a) Tip etching setup. (b) Tungsten tip immersed in the KOH solution (c)Image of W tip, prepared by electrochemical etching, under an optical microscope. (d) Schematic showing tip heating setup.	49
2.9	(a) In-situ cleaving setup. (b) Sample just after cleaving.	51
2.10	Schematic illustrating the interaction of MFM cantilever with the stray field of the sample.	52
2.11	Range, as a function of tip-sample distance, over which the interaction forces dominate the MFM signal.	53
2.12	(a) Schematic illustrating the design of LT-MFM. The inset shows the optical cavity. (b) MFM microscope head.	55
2.13	MFM dual pass phase image taken on the cleaved single crystal of Fe_3GeTe_2 using Attocube LT-MFM at 1.6 K . The magnetic filamentary domains are clearly visible. The contrast in the image corresponds to the regions of opposite magnetization.	57
3.1	(a) Crystal structure of Fe_3GeTe_2 . (b) STM topograph of $9 \text{ nm} \times 9 \text{ nm}$ area taken on the cleaved surface of Fe_3GeTe_2 taken at sample bias $V_b= 0.6 \text{ V}$ and tunneling current $I_t = 200 \text{ pA}$	60

3.2	(a) Temperature dependence of ballistic spectra (shown by colored dots) and their corresponding BTK fits (shown by black line). All the spectra are normalised and equal vertical shift to spectra with respect to conductance spectrum at 1.7K is given for clarity. (h) Temperature dependence of the superconducting gap (shown by black dots). The error bars depict the range of Δ for which a reasonable fit could be obtained using a modified BTK theory. The expected variation of the gap from BCS theory is shown by solid red line.	63
3.3	(a)-(c) Three fitted ballistic spectra with different values of barrier strength (Z) and spin polarisation (P_t). (d) P_t vs Z . The extrapolated value of P_t (at $Z=0$) is around 61%. The error bars depict the range of P_t for which a reasonable fit could be obtained using a modified BTK theory.	64
3.4	(a)-(b) In-plane and out-of plane magnetic field angle dependence of resistance taken at zero bias and 11 K. The $\cos^2(\phi)$ and $\cos^2(\theta)$ fits are shown by solid black lines. All the resistance curves are normalised and equal vertical shift to resistance curves with respect to curve at lowest magnetic field is given for clarity.	65
3.5	(a)-(b) Band structure and the electronic density of states (DOS) is calculated for the ferromagnetic state respectively.	66
3.6	(a) The temperature dependence of high Z point contact. The inset shows the Fano lineshape fitting (shown by black line) of the conductance spectrum (shown by colored dots) taken at 10 K. (b) Temperature dependence of the normal state along with the Fano lineshape fits. Spectra are vertically shifted for clarity. (c)-(d) Two normalised conductance spectra (shown by colored dots) and their Fano lineshape fitting (shown by black line) taken at 12 K.	67
3.7	(Color online) Real-space view of spin configurations at low temperature ($T/t = 0.01$) for (a) $\lambda/t = 0.1$, (b) $\lambda/t = 0.5$ and (c) $\lambda/t = 1$	70
3.8	MFM dual pass phase images taken on the single crystals of Fe_3GeTe_2 , at different temperatures, showing contrast of ferromagnetic domains in the zero field cooled state. The sample temperature for the images is (a) 1.6 K (b) 93 K (c) 165 K and (d) 205 K. As the sample temperature is increased to 205 K the stripy domains vanishes.	71
3.9	(a)-(b) MFM dual pass phase images taken the field-cooled state in the presence of the stray field of the MFM cantilever. (Color online) Representative spin configurations at $T/t = 0.01$ and $\lambda/t = 0.5$ for (c) $h_z = 0.44$ and (d) $h_z = 0.84$	72

3.10	(a)-(c) MFM dual pass images in the field-cooled state (FC) where an external field of 1.2 kOe was applied. The lift height was kept constant at 30 nm for all the images. (Color online) Representative spin configurations at $T/t = 0.01$, $\lambda/t = 0.1$ and $A_u = 0.08$ for (d) $h_z = 0.004$, (e) $h_z = 0.016$ and (f) $h_z = 0.028$	73
4.1	(a) Crystal structure of Fe_4GeTe_2 . (b) STM topograph of $7.7 \text{ nm} \times 7.7 \text{ nm}$ area taken on the cleaved surface of Fe_4GeTe_2 at sample bias $V_b = 0.82 \text{ V}$ and tunneling current $I_t = 200 \text{ pA}$. The atoms are clearly resolved. (c) STM topograph of area $80 \text{ nm} \times 80 \text{ nm}$ showing step taken at $V_b = 0.9 \text{ V}$ and tunneling current $I_t = 120 \text{ pA}$. The height of the step is shown in the inset. (d) Temperature dependence of the dc magnetization of Fe_4GeTe_2 in zero fields and field cooled state taken at $\mu_0 H = 1000 \text{ Oe}$ for $H \parallel c$. (e) Schematic showing a tip and sample forming point contact.	80
4.2	(a)-(f) Six fitted ballistic spectra using Nb tip with different values of barrier strength (Z) and spin polarisation (P_t).	83
4.3	(a)-(f) Six fitted ballistic spectra using Pb tip with different values of barrier strength (Z) and spin polarisation (P_t).	84
4.4	(a) P_t vs Z for point contact junctions of Fe_4GeTe_2 with Nb and Pb tips. The error bars depict the range of P_t for which a reasonable fit could be obtained using a modified BTK theory. (b) Spin-polarized band structure and (c) density of states calculated for the ferromagnetic state.	85
4.5	(a) The evolution of the conductance spectra, with temperature, obtained for a $\text{Fe}_4\text{GeTe}_2/\text{Nb}$ point contact junctions. A clear anti-symmetric double-peak structure below and above the superconducting transition temperature of Nb can be seen at a higher bias. (b) The temperature evolution of the normal state was obtained for the same point contact junction. The spectra are shifted vertically with respect to the spectrum at the lowest temperature for clarity.	87
4.6	(a) STM topograph of area $10.5 \text{ nm} \times 10.5 \text{ nm}$ area taken on the cleaved surface of Fe_4GeTe_2 at sample bias $V_b = -0.5 \text{ V}$ and tunneling current $I_t = 490 \text{ pA}$. Both dark and bright defects can be seen in the topograph. (b)-(d) dI/dV spectra taken at tip positions marked by the black arrows in (a). The spectra fit well with a Fano lineshape.	88

4.7	MFM dual pass phase images taken on a cleaved single crystal of Fe_4GeTe_2 where (a)-(b) was taken at 70 K in the zero field cooled and field cooled state. (c)-(f) were taken in the field-cooled state at sample temperatures of 80 K, 90 K, 100 K, and 110 K respectively. The field cooling was done in the presence of the stray field of the MFM cantilever.	89
5.1	(a) Schematic illustrating an array of parallel Rashba nanowires lying in proximity to s-wave superconductor and with Zeeman field V_z applied along z direction.	95
5.2	Energy dispersion for an assembly of five Majorana wires as a function of the momentum along the wires, (k_x): for uncoupled (in red) (a) trivial regime ($V_z = 0, t_y = 0, \beta = 0$) (b) topological regime ($V_z = 0.85t, t_y = 0, \beta = 0$) and coupled (in blue) (c) trivial regime ($V_z = 0, t_y = 0.3t, \beta = 0.3t$) (d) topological regime ($V_z = 0.85t, t_y = 0.3t, \beta = 0.3t$) is shown. The other parameters used for calculations are $\alpha = 1 t, \mu = -2 t$ and $\Delta = 0.6 t$	97
5.3	Plot of energy spectrum as a function of Zeeman field in the topological regime for : (a), (b) $N= 3$ and 4 uncoupled (in red) wires respectively, both hosting zero energy states beyond $V_z= 0.6t$ (c), (d) $N= 3$ and 4 coupled (in blue) wires where, for $N= 3$, a zero energy state can be seen beyond $V_z > 0.75t$ while no such state appears for $N=4$. The number of states near zero energy is equal to N in both cases. The lowest 48 levels have been plotted. The parameters used for plotting both uncoupled and coupled cases in the topological regime are mentioned in Fig. 5.2.	98
5.4	(a) Schematic for measuring tunneling conductance of array of Majorana wires. The normal leads (in blue) are connected to Majorana wires (red) with a tunnel barrier (green) at the interface of the junction. A bias V is applied to the normal leads. Using a mechanical switch, the number of transport active wires can be controlled. The plot of zero temperature differential conductance vs applied bias V of a different number of wires for (b) trivial uncoupled case (c) trivial coupled case (d) topological uncoupled case. . . .	99
5.5	Plots of differential conductance vs applied bias for $N = 2$ to 10 weakly coupled Majorana wires in the topological regime ($V_z= 0.85t; t_y = 0.3t; \beta= 0.3t$) is shown. Plots (b),(d),(f), and (h) show that the ZBCP peak appears only in the case of conductance of an odd number of wires (shown in green) while no such peak is observed at zero bias for the case of (a), (c), (e), (g) and (i) plots depicting the conductance of even number of wires (shown in black).	101

5.6	(a)-(b) Tunneling conductance of 2 and 3 weakly coupled wires respectively, at different temperatures without any dissipation. (c)-(d) The zero temperature tunneling conductance of 2 and 3 weakly coupled wires respectively, for different values of dissipation.	102
5.7	Plot of energy spectrum in the topological regime as a function of (a) t_y when $\beta = 0$ for an assembly of 4 wires (b) t_y when $\beta = 0$ for an assembly of 5 wires (c) β when $t_y = 0$ for an assembly of 4 wires (d) β when $t_y = 0$ for an assembly of 5 wires. The lowest 48 levels have been plotted. The even-odd effect can be predominantly seen when β is finite.	103
5.8	The differential conductance, on the color scale, map as a function of (a) t_y when $\beta = 0$ for an assembly of 4 wires (b) t_y when $\beta = 0$ for an assembly of 5 wires (c) β when $t_y = 0$ for an assembly of 4 wires (d) β when $t_y = 0$ for an assembly of 5 wires.	104
5.9	The differential conductance at zero bias, on the color scale, map as a function of a chemical potential μ and Zeeman field V_z (a) for an assembly of 4 uncoupled wires (b) for an assembly of 5 uncoupled wires (c) for an assembly of 4 weakly coupled wires (d) for an assembly of 5 weakly coupled wires.	106
5.10	Schematic showing a parallel array of semiconducting Rashba spin-orbit coupled nanowires lying in proximity to an s-wave superconductor.	107
5.11	(a) The evolution of the energy spectrum with ϕ for V_{Zeeman} being fixed at $0.85 t$ and θ being set to 90° is shown. The spectrum is symmetric for positive and negative values of ϕ . (b) The variation of the energy spectrum with θ for V_{Zeeman} being fixed at $0.85 t$ and ϕ being set to 0° is shown. A state at zero energy appears for all values of θ . The other parameters used for calculations are $t_x = t$, $\alpha = 1t$, $\mu = -2t$, and $\Delta = 0.6t$	108
5.12	(a) The energy dispersion of 1-D nanowire when field angles are $\phi = 0^\circ$ and $\theta = 90^\circ$. The bulk is fully gapped near zero energy. (b) The energy dispersion for critical angle $\phi_c = 44.5^\circ$ when $\theta = 90^\circ$. The gap is partially closed at this orientation, and (c) The energy dispersion for $\phi = 90^\circ$ and $\theta = 90^\circ$. The gap becomes fully closed at zero energy for this orientation of the magnetic field.	109

- 5.13 (a) The differential conductance (in units of $2\frac{e^2}{h}$) vs applied bias for different values of θ keeping ϕ fixed at 0° . The inset shows that the magnitude of the conductance remains the same for all values of θ . (b) The differential conductance (in the units of $2\frac{e^2}{h}$) of a 1-D nanowire, on the color scale, as a function of applied bias and field angle θ . (c) A plot of differential conductance (in units of $2\frac{e^2}{h}$) vs applied bias for different values of ϕ keeping θ fixed at 90° . The inset shows the variation of differential conductance with respect to field angle ϕ at zero bias. The conductance magnitude decreases from the quantized value of $2\frac{e^2}{h}$ at $\phi=0^\circ$ to nearly zero for $\phi=90^\circ$. (d) The differential conductance (in units of $2\frac{e^2}{h}$) of a 1-D nanowire, on the color scale, as a function of applied bias and ϕ 110
- 5.14 (a)-(b) The differential conductance on the color scale, as a function of applied bias and θ $N=2$ and $N=3$ for uncoupled nanowires respectively. The magnitude of conductance remains constant with variation in θ . (c)-(d) The differential conductance on the color scale, as a function of applied bias and ϕ for $N=2$ and $N=3$ wires respectively. Similar to the conductance of a single wire, the conductance magnitude drops to zero beyond the critical angle with variation in ϕ . (e) Conductance of multiple uncoupled wires at zero bias vs θ and (f) Conductance of multiple uncoupled wires at zero bias vs ϕ . The total conductance of $N 2\frac{e^2}{h}$ at zero bias, for N number of transport active wires, corresponds to each edge Majorana contributing a conductance of $2\frac{e^2}{h}$ 111
- 5.15 The variation of the energy spectrum with ϕ for V_{Zeeman} fixed at $0.85 t$ is shown in (a) and (c) for 2 and 3 wires respectively. It can be seen that a new critical angle exists in the weakly coupled case which is smaller than the critical angle for uncoupled wires. The evolution of the energy spectrum with θ for fixed V_{Zeeman} is shown in (b) and (d) for 2 and 3 wires respectively. 112
- 5.16 The plot of conductance vs the applied bias V for fixed θ and ϕ being set to 0° (shown in black), critical angle 40° (shown in green) and 90° (shown in blue) is presented for 2 and 3 weakly coupled wires in (a) and (b) respectively. For comparison, the variation of the same with fixed ϕ and for θ being set to 0° , 40° , and 90° has been studied for 2 and 3 weakly coupled wires in (c) and (d) respectively. For the weakly coupled regime the parameters used are $t_y = 0.3t$, $\beta = 0.3t$, and the rest of the parameters are the same as mentioned in Figure (1). 113

5.17	(a)-(b) Differential conductance, on the color scale as a function of applied bias and θ for $N=2$ and 3 weakly coupled wires respectively. (c)-(d) Differential conductance, on the color scale as a function of applied bias and ϕ for $N=2$ and 3 weakly coupled wires respectively.	114
5.18	(a)-(b) The differential conductance on the color scale, as a function of ϕ and β (when $t_y=0$) for $N=2$ and $N=3$ weakly coupled nanowires respectively. (c)-(d) The differential conductance on the color scale, as a function of θ and β (when $t_y=0$) for $N=2$ and $N=3$ weakly coupled wires respectively. Wires remain uncoupled when β is very small. As β increases the odd-even effect is seen only for certain angles when ϕ is varied keeping θ fixed while for variation with θ , with ϕ fixed, the odd-even effect is prevalent at all values of θ	115
5.19	(a)-(b) The differential conductance on the color scale, as a function of ϕ and t_y when $\beta=0$ for $N=2$ and $N=3$ weakly coupled nanowires respectively. (c)-(d) The differential conductance on the color scale, as a function of θ and t_y when $\beta=0$ for $N=2$ and $N=3$ weakly coupled wires respectively. An odd-even effect is seen for high values of t_y	116

List of Tables

1.1	A list of a few experimentally demonstrated and theoretically predicted vdW magnets.	5
1.2	Probabilities of Andreev reflection and normal reflection, as per BTK theory, for different energy scales. Here, $\varepsilon = \frac{E^2 - \Delta^2}{E^2}$	14
1.3	Probabilities $A_p(E)$ and $B_p(E)$	17

Introduction

1.1 Two-dimensional materials

With the onset of the "big data" era, the demand for power-saving data storage devices has increased tremendously. While complementary metal–oxide–semiconductor (CMOS)-based devices have contributed to society immensely, further down-scaling the size of such devices has become increasingly challenging and requires advanced fabrication techniques to be cost-effective [1]. However, the increasing demand for power-saving data storage and processing cannot be fulfilled without such down-scaling. In this context, the community has been engaged in realizing devices that use the "spin" degree of freedom of the conduction electrons instead of their charge for novel functionalities. These devices are termed "spintronic" devices [2–5]. The field of spintronics started with the discovery of giant magnetoresistance (GMR), in a magnetic heterostructure [6], the technology behind magnetic read heads in the hard disk drive (HDD). Since then, a rich variety of spintronic-based data storage devices have been developed. While a GMR device uses a nonmagnetic metal as a spacer between the two ferromagnetic (FM) layers, the idea that data storage density can be increased by using an insulating material as a spacer led to the development of a magnetic tunnel junction (MTJ) device [7]. Both GMR and MTJ devices attain magnetization reversal based on the magnetic field induced by passing large currents through wires. To overcome this, the next generation of magnetoresistive random access memory (MRAM) is based on the spin torque transfer (STT) effect [8] for accomplishing data writing and has the additional advantage of low power consumption and better performance over the earlier MRAM devices [9]. However, in STT-based MRAM, a large current is needed for magnetization reversal which may break the barrier layer, hence limiting their use. Recently, efforts have been made both theoretically and experimentally to have spintronic architecture built with 2-D van der Waals (vdW) materials [10–17] in order to realize low-power-consuming, high-performance, and beyond CMOS electronic devices.

vdW materials are a rich class of materials where the 2-D atomically thin layers are held together with strong in-plane covalent bonding and weak out-of-plane van der Waals forces, making it possible to isolate individual layers without damaging the crystallinity within each layer. Their layered structure offers a viable platform for the realization of complex functional devices through vdW heterostructuring [18, 19]. The successful exfoliation of monolayer graphene from the bulk graphite in 2004 [20], made these materials the central focus of the research in condensed matter physics. There are several novel attributes of the 2-D materials that give them an advantage over their 3-D bulk counterparts. The twist degree of freedom in these materials, where the twist angle between two 2D layers of the same or different materials can be tuned, has opened a new window to the observation of a number of exotic phenomena like Moiré physics [21–25], correlated insulator states [26], fractal Hofstadter’s butterfly [27, 28], topologically non-trivial states and unconventional superconductivity [29]. The 2-D materials can also exhibit long-range magnetic order at finite temperatures, persisting down to the monolayer limit. The magnetic genome of these materials is often termed the 2-D vdW magnets.

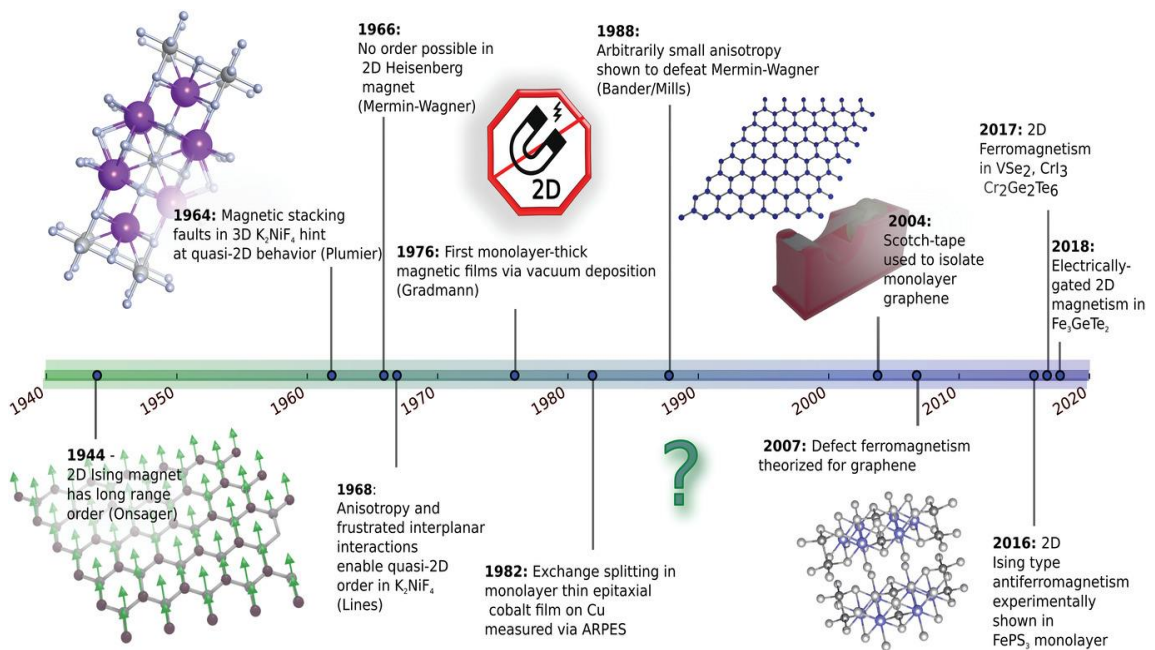


Figure 1.1: The progression of 2-D magnetism over the past few decades is shown in a timeline [30].

1.2 vdW magnets

1.2.1 Magnetism in 2-D

Until the discovery of intrinsic ferromagnetism in 2-D materials $\text{Cr}_2\text{Ge}_2\text{Te}_2$ [10] and CrI_3 [32], the realization of magnetic order in 2-D remained an elusive dream. This breakthrough led to a plethora of opportunities and new discoveries. Figure 1.1 depicts the timeline of developments in the area of 2-D magnetism made over the previous decades.

The spatial and spin dimensionality (n) has a significant role in determining the existence of a magnetic ground state. While in 3-D systems the magnetic ordering of moments is possible at finite temperatures, in 1-D the magnetic phase transition can occur only at absolute zero temperature [33]. This situation attains a complex character in 2-D, where the existence of a magnetic order depends critically on the spin dimensionality (n). In a 2-D system with $n=1$, explained well by the Ising model [34, 35], the spins are only allowed to orient either in-plane or out-of-plane as shown in Figure 1.2 (a). Onsager's [36] solution of the 2-D Ising model showed that for a system with $n=1$, the phase transition from a non-ordered paramagnetic state to an ordered ferromagnetic state can always occur at finite temperatures. The system, as a consequence of strong uniaxial anisotropy, exhibits a gapped spin wave spectrum that counters the effect of thermal fluctuations. The system with $n=2$, explained well by the XY model, exhibits easy plane anisotropy where the spins are restricted to orient only in 2D plane [37, 38]. However, within a given plane the orientation can be random as shown in Figure 1.2 (b). Such a 2-D system undergoes an unconventional magnetic transition known as the Berezinskii–Kosterlitz–Thouless (BKT) phase transition, where isolated vortices and anti-vortices form a quasi-long-range magnetic order with the formation of vortex-antivortex bound pairs below a certain transition temperature (T_{KT}). On the contrary, intrinsic ferromagnetism is absent at finite temperatures in the isotropic system ($n=3$) where the spins are allowed to orient in any direction as shown in Figure 1.2 (c). Such a 2-D system can be described under the paradigms of the Heisenberg model [39]. The existence of long-range magnetic ordering in isotropic 2-D systems is prevented by the Mermin–Wagner–Hohenberg theorem [40, 41]. The theorem is based on the idea that the excitation of the gapless long-wavelength spin waves prevents the existence of a long-range magnetic ordering in isotropic systems with dimensions $d \leq 2$, due to thermal fluctuations. A generalized Heisenberg spin Hamiltonian can be written for the aforementioned 2-D systems with different spin dimensionality as

$$H = -\frac{1}{2} \sum_{i,j} J \mathbf{S}_i \mathbf{S}_j - \sum_i K (S_i^z)^2 - g \mu_B B \sum_i S_i^z \quad (1.1)$$

In equation (1.1), the first term corresponds to the pure Heisenberg Hamiltonian, where J is

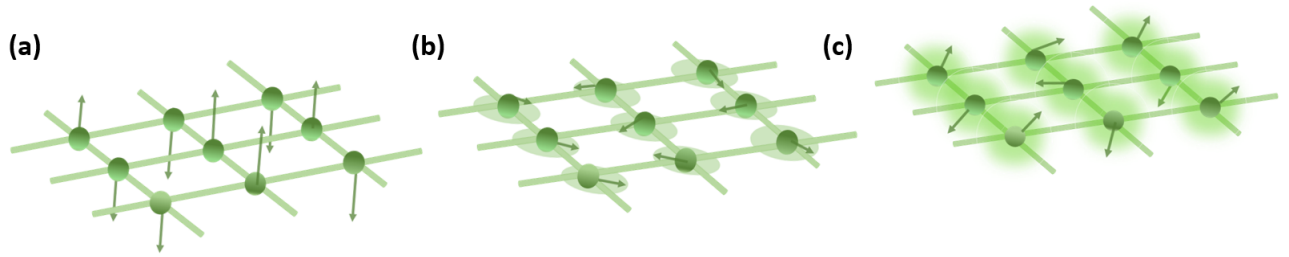


Figure 1.2: The diagram illustrates the variation in the preferred spin orientation with different spin dimensionality. In this context, (a) $n = 1$ correlates to the Ising Hamiltonian with strong uniaxial anisotropy, while (b) $n = 2$ and (c) $n = 3$ correspond to systems with easy-plane anisotropy (XY Hamiltonian) and isotropic Heisenberg Hamiltonian, respectively.

the exchange coupling between the neighboring spins on lattice sites i and j . The sign of J determines whether the ferromagnetic ($J > 0$) or anti-ferromagnetic ($J < 0$) order exists. In the second term, The coefficient K corresponds to the on-site anisotropy, such that $K=0$ for the isotropic Heisenberg model ($n=3$), and non-zero for the Ising model ($n=1$) and 2-D XY model ($n=2$) exhibiting easy-axis and easy-plane anisotropies respectively. The third term corresponds to the coupling of the local magnetic moments to the applied external magnetic field B .

Initially, attempts were made to induce magnetic order in 2-D vdW materials of non-magnetic origin through defect engineering [42], proximity effects [43, 44], or magnetic doping [45]. However, the magnetism achieved through these methods was weak making such materials unreliable for spintronic applications. The first evidence of a long-range order originating intrinsically from the 2-D parent lattice was given by Cheng Gong *et al.* in $\text{Cr}_2\text{Ge}_2\text{Te}_2$ in 2017 [10]. This discovery completely reshaped the existing understanding of 2-D magnetism in the community. Their results showed that intrinsic ferromagnetism can exist in 2-D, contrary to the restrictions set by the Mermin–Wagner–Hohenberg theorem, in the presence of magnetic anisotropy in the system where the system aligns its spin along a preferred direction. The presence of magnetic anisotropy in the system stabilizes the long-range magnetic order by opening a gap in the spin wave density of the states. Bevin Huang *et al.* [32] and J. L. Lado *et al.* [46] showed that the ferromagnetic state exists in CrI_3 down to monolayer, where the origin of magnetic anisotropy is due to superexchange interaction between the Cr-I-Cr bonds. The origin of magnetic anisotropy in ferromagnets can be linked to the presence of shape anisotropy, magnetocrystalline anisotropy, spin-orbit coupling, strain-induced anisotropy, etc. A brief list of theoretically predicted and experimentally realized 2-D vdW magnets is shown in Table 1.1.

2-D material	Magnetic order	T_C or T_N	Electrical Properties
$\text{Cr}_2\text{Ge}_2\text{Te}_6$	FM	30 K (bilayer) 68 K (bulk)	Insulator
$\text{Cr}_2\text{Si}_2\text{Te}_6$	FM	33 K (monolayer) 290 K (under stress)	Semiconductor
CrI_3	FM	45 K (monolayer) 61 K (bulk)	Insulator
CrBr_3	FM	37 K (monolayer)	Insulator
ReI_3	FM	65 K (theoretic)	Half-metal
ReBr_3	FM	390 K (theoretic)	Half-metal
VSe_2	FM (monolayer) PM (bulk)	300 K (monolayer)	Metal
MnSe_2	AFM	300 K (monolayer)	Metal

Table 1.1: A list of a few experimentally demonstrated and theoretically predicted vdW magnets.

1.2.2 Fe_nGeTe_2

High electrical conductivity, high ferromagnetic Curie temperature, large spin-polarization at the Fermi level of material and its ease of integrating with other materials are some of the most important prerequisites for application in spintronic devices. Most of the well-studied vdW ferromagnets, some of them listed in Table 1.1, lack at least one of the desired attributes discussed above making them unsuitable for realistic applications. In this context, the iron-based family of vdW ferromagnets with the general formula Fe_nGeTe_2 (with $n \geq 3$), stands out due to their near-room temperature ferromagnetism, high uniaxial magnetic anisotropy, high saturation magnetization, and good metallicity. The enhanced Curie temperature (T_{Curie}) in these family of ferromagnets can be achieved by increasing the exchange interaction by tuning the Fe-concentration [47]. These systems are known to exhibit itinerant ferromagnetism governed by the paradigms of the Stoner model [47–49]. The extensively studied ferromagnet from this family, Fe_3GeTe_2 , shows a T_{Curie} of 230 K in the bulk [50, 51] which can be increased to room temperature through ionic gating or patterning [52, 53]. Additionally, the successful fabrication of Fe_3GeTe_2 -based spin valves [54] and magnetic tunneling junctions have demonstrated its potential uses in the next generation of spintronic devices that can significantly speed up the storing, processing, and transfer of

information. Within this family, stoichiometric Fe_4GeTe_2 has near-room temperature ferromagnetism along with a spin re-orientation transition i.e. change in the orientation of magnetic anisotropy from in-plane to out-of-plane on cooling below 110 K [55, 56]. Fe_5GeTe_2 shows the highest T_{Curie} of 300 K [49], in the family. However, T_{Curie} of Fe_5GeTe_2 has been observed to be sensitive to Fe-vacancy and thermal cycling. Fe_3GeTe_2 also exhibits strong correlations, as evidenced by the significant value of the Sommerfeld coefficient observed in measurements of specific heat and scanning tunneling spectroscopy (STS) [57, 58]. Such behavior has not been reported or investigated in the other members of the family yet. It is important to investigate the interplay of various quantum phenomena in these vdW ferromagnets, for their application in realizing highly efficient spintronic devices, which have been one of the goals of the present work. We have studied the spin-polarized transport characteristics of two members of Fe_nGeTe_2 : Fe_3GeTe_2 and Fe_4GeTe_2 through different spectroscopic techniques. The local magnetization characteristics of these ferromagnets have also been probed by performing domain imaging.

1.3 Spin polarization of ferromagnets

As previously stated, a crucial prerequisite for the development of spintronic devices is the creation of highly spin-polarized current. One of the primary sources of spin-polarized current is ferromagnetic materials. Due to the splitting of spin-up and spin-down bands known as exchange splitting, ferromagnets can exhibit a significant degree of spin polarization at the Fermi level. Consequently, studying the spin polarization of ferromagnets is essential for the advancement of materials with desired magnetic properties and the design and optimization of devices like spin valves and magnetic tunnel junctions. Various techniques can be employed to evaluate the spin polarization of ferromagnets. One such technique, introduced by Meservey and Tedrow [59], involves analyzing tunneling through a junction between a ferromagnet and a superconductor to determine the spin polarization value. The conductance spectrum of this junction displays coherence peaks that, under the influence of a strong parallel magnetic field (B), split asymmetrically. Measuring this asymmetry provides a direct estimation of the magnitude and direction of spin polarization. Other techniques used for measuring the spin polarization of ferromagnets include spin-resolved photoemission spectroscopy [60] and scanning tunneling microscopy [61]. However, these methods are highly sensitive to surface properties. An alternative well-known method to calculate the spin polarization of ferromagnets, without the need for extremely high magnetic fields or an ultra-clean surface, is the spin-polarized point contact Andreev reflection spectroscopy (PCARS) [62]. Before delving into the applications of PCARS as a spin-resolved probe, we will first explore the fundamentals of point contact spectroscopy (PCS).

1.3.1 Point Contact Spectroscopy (PCS)

PCS [63] is a widely recognized spectroscopic tool employed to investigate the scattering mechanisms, involving conduction electrons and elementary excitations such as phonons, magnons, Bogoliubons in superconductors, etc. [64, 65]), by measuring the non-linearities in I - V . In this experimental method, a sharp tip and a freshly cleaved or polished sample are brought into physical contact, either through a step-positioner or a differential screw, until a micro-constriction is formed, enabling electrical transport. The electron transport through a point contact junction involving two metal electrodes is based on two key parameters: the mean free path of the electron (l) and the diameter (a) of the constrictions. In other words, depending on the value of ' l ' and ' a ' different regimes of electronic transport (discussed below) can be realized.

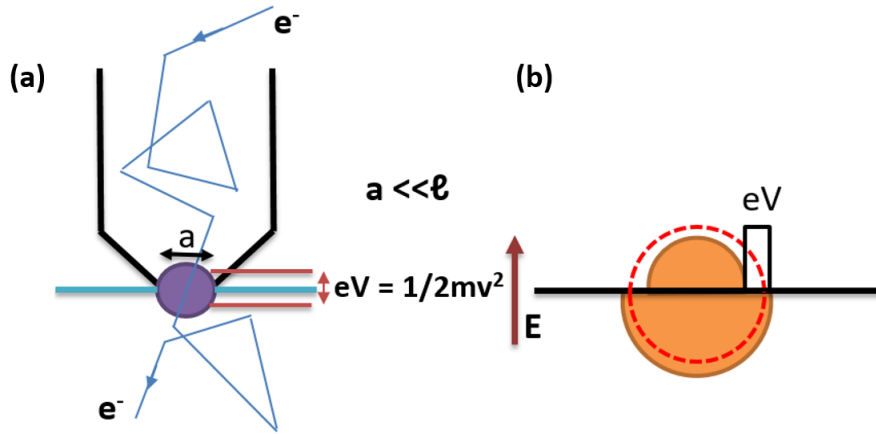


Figure 1.3: (a) Schematic depicting transport through a point contact formed in a ballistic regime ($a \ll l$). (b) The electron distribution in the ballistic regime at the center of the contact is shown.

Ballistic regime: A regime known as the ballistic regime of transport is achieved when the elastic mean free path of electron ' l ' is much greater than the point contact diameter ' a ' as shown in Figure 1.3 (a). When a bias voltage (V) is applied to a ballistic point contact, the electrons within the contact diameter can undergo acceleration, acquiring kinetic energy proportional to the applied bias. Since the electron travel through the contact ballistically, it is possible to attain high energies within the contact region. Sharvin [66] developed an expression for such a junction, by applying Knudsen's technique to the problem of diluted gas passing through a small hole, as $R_S = \frac{4\rho l}{3\pi a^2}$. For metals, the resistivity of the material is inversely proportional to the mean free path making R_S independent of l and dependent on a only. Hence, the resistance of a ballistic point contact can be written as $R_S = \frac{2h}{e^2 (ak_F)^2}$. where ak_F represents the number of conduction channels. The momentum space (k -space) of the

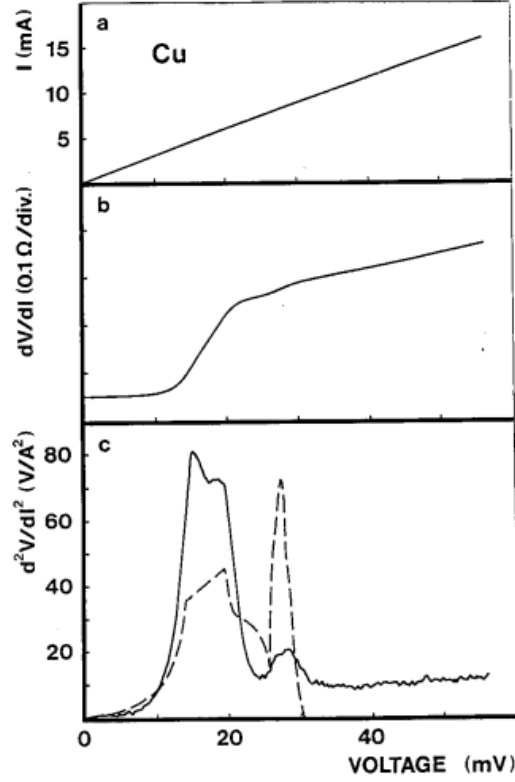


Figure 1.4: Point contact studies for a Cu-Cu point contact with a contact resistance of 3.3Ω at a temperature of 1.5K where a) I-V. (b) The differential resistance, $\frac{dV}{dI}$. (c) The second derivative, $\frac{d^2V}{dI^2}$. The dashed curve depicts the phonon density of states, $F(\epsilon)$, obtained through neutron scattering experiments [68].

point contact in the ballistic regime, as shown in Figure 1.3 (b), exhibits deformed Fermi surfaces (FS). These deformed FS consist of two half spheres, with a difference in a radius equal to the magnitude of the applied bias voltage (eV). When the electron energy is high enough, it may excite elementary excitations like phonons in metals, magnons in magnets, and Bogoliubons in superconductors by undergoing inelastic (back) scattering within the contact region. This results in a negative correction to the current value I at certain bias voltages about the characteristic energies of elementary excitations, given by:

$$I = \frac{-2\pi e}{\hbar} \Omega_{eff} N(0) \int_0^{eV} d\epsilon \int_0^{eV} d\epsilon' S(\epsilon - \epsilon') \quad (1.2)$$

where $N(0)$ is the density of states at the Fermi energy, Ω_{eff} is the effective volume over which the inelastic scattering takes place, and $S(\epsilon)$ is the energy-dependent spectral function for the scattering interaction. If the initial and the final electron states are given by $|\vec{k}\rangle$ and $|\vec{k}'\rangle$ respectively, then

$$S(\varepsilon) = \frac{N(0)}{32\pi^2} \int \frac{d^2\vec{k}}{k^2} \int \frac{d^2\vec{k}'}{k'^2} |g_{kk'}|^2 \eta(\vec{k}, \vec{k}') \delta(\varepsilon - \varepsilon_k + \varepsilon_{k'}) \quad (1.3)$$

where $|g_{kk'}|^2$ corresponds to the scattering matrix elements and $\eta(\vec{k}, \vec{k}')$ gives the efficiency function. For a ballistic regime, $\Omega_{eff} = \frac{8a^3}{3}$. Therefore, the corrected differential conductance is

$$\frac{dI}{dV} = \frac{1}{R_S} - \frac{2}{3} e^2 a^3 N(0) \frac{1}{\tau(eV)} \quad (1.4)$$

where $\frac{1}{\tau(eV)}$ is the inverse scattering time within the contact region and is related to the spectral function as $\frac{1}{\tau(eV)} = \frac{2\pi}{\hbar} \int_0^V S(\varepsilon) d\varepsilon$. Unlike, tunneling experiments, PCS conductance is independent of the energy-dependent density of states.

A direct analysis of the nonlinear I-V curves can provide energy-dependent information on the electron-phonon scattering mechanism. The electron-phonon interaction plays an important role in the thermal and electrical properties of the solids as well as in superconductivity. Yanson [67] calculated for the first time the electron-phonon spectral function for a point contact junction by measuring the second derivative of the voltage with respect to the current ($\frac{d^2V}{dI^2}$), which is similar to the Eliashberg function $\alpha^2S(\varepsilon)$; α is the electron-phonon coupling constant. The demonstration of the measurement of electron-phonon spectral function in a Cu-Cu point contact junction is given in Figure 1.4. An increase in the differential resistance, $\frac{dV}{dI}$, with the applied bias corresponding to the zone-boundary phonon frequencies can be seen in Figure 1.4(b). Peaks are observed in the second derivative, $\frac{d^2V}{dI^2}$, at energy levels of 16-20 meV and 30 meV corresponding to the transverse phonons and longitudinal phonons, respectively (Figure 1.4(c)). The results depict the power of PCS as a spectroscopic tool to probe energy-resolved information, of the scattering processes involving conduction electrons and elementary quasiparticles, by tuning the applied bias over the point contact junction.

Thermal regime: Contrary to the ballistic regime is the thermal regime where $a \gg l$ (Figure 1.5(a)). In this regime, in the contact region, electrons can scatter inelastically just like they would in bulk. The resistance of point contact, as calculated by Maxwell using the Poisson equation, is given by $R_M = \frac{\rho(T)}{2a}$ where ρ is the resistivity of the material under study [68]. Due to the inelastic scattering of electrons within the contact region, Joule heating occurs in the contact region resulting in a local increase in the temperature at the center of contact. Thus, any spectroscopic information within the contact region is lost. The FS, as shown in Figure 1.5(b), is only slightly shifted, similar to the transport of electrons in a normal conductor.

The resistance of the contact, between the two above-discussed extreme regimes, can be expressed using Wexler's formula [69]: $R = R_S + \Gamma(l/a) R_M$; where R_S is the Sharvin's resis-

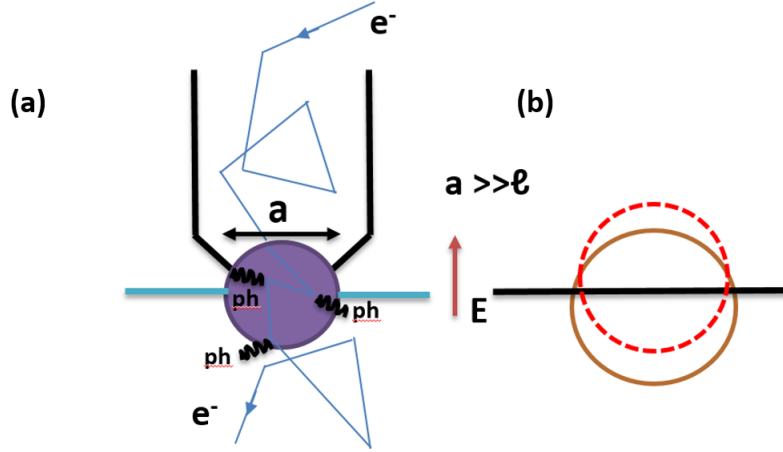


Figure 1.5: (a) Schematic showing transport in the thermal regime. The electrons can undergo inelastic scattering within the contact region leading to Joule heating. (b) The FS is shifted slightly by eEl , where E is the applied electric field and l is the mean free path of electrons.

tance for ballistic point contact and R_M is Maxwell's resistance for thermal point contact.

Diffusive regime: Apart from the ballistic and thermal regime there lies another regime of transport known as the diffusive regime where $l_{el} < a < \sqrt{l_{in}l_{el}}$. In other words, in a diffusive regime, the contact diameter is bigger than the elastic mean free path of electrons but smaller than the diffusive length ($\sqrt{l_{in}l_{el}}$) as shown in Figure 1.6(a). Therefore, the electrons can undergo elastic scattering within the contact region but inelastic scattering is not allowed. As a consequence of elastic scattering, the electrons are redistributed isotropically within an energy shell of width eV . The spectroscopic information is still present in the contact region, but compared to the ballistic regime, the effective volume for the backflow current produced by the inelastic scattering of electrons has been reduced by a factor of the order of a/l .

1.3.2 Point contact Andreev reflection spectroscopy

Till now, we have discussed the transport through point contact junctions formed between normal metals. A special case of PCS is the point contact Andreev reflection spectroscopy (PCARS) based on the point contact junctions between normal metal-superconductor. In a normal metal-superconducting ballistic junction, the transport is dominated by Andreev reflection [70], a quantum process through which a normal current in the metal converts to a supercurrent in the superconductor. Schematic of the process is shown in Figure 1.7. For an incident electron with energy greater than the superconducting gap (2Δ) of the superconductor, transmission from the normal metal to the superconductor can take place. But if the

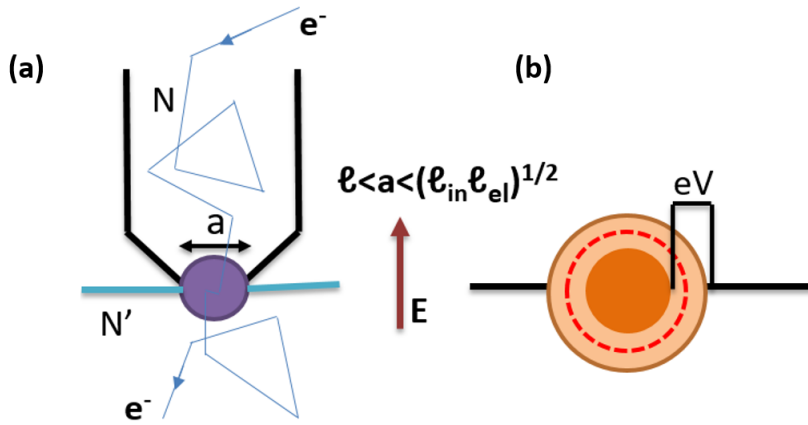


Figure 1.6: (a) Schematic showing transport in the diffusive regime. The electrons can undergo elastic scattering within the contact region. (b) The process of elastic scattering redistributes the electrons across a spherical region, but this redistribution is limited to an energy shell characterized by a width equal to eV .

incident electron has energy less than the superconducting gap, such transmission is forbidden. However, for such energy scale, a process where an up (down) spin electron is reflected as a down (up) spin hole in the normal metal resulting in the simultaneous formation of Cooper pair at the Fermi level of the superconductor can take place. This unique process, known as Andreev reflection, is a consequence of the particle-hole symmetry in superconductors. By measuring the conductance of the point contact ($G(V) = \frac{dI}{dV}$) as a function of bias voltage, one can obtain information about the superconducting energy gap. At zero temperature, for a transparent N-S interface, the enhancement in the value of conductance at a low bias ($V < \Delta$) is 200% than the conductance at a high bias ($V > \Delta$).

1.3.3 BTK formalism

The Andreev reflection spectra (dI/dV versus V) obtained through N-S point contact junctions are usually analyzed in the framework of the theory given by Blonder, Tinkham, and Klapwijk (BTK) [71]. This theory employs a δ -function potential barrier at the interface, which is of the form $V(x) = V_0 \delta(x)$. The strength of the barrier can be characterized by a dimensionless quantity $Z = V_0 / \hbar v_F$, where v_F is the Fermi velocity. The interfacial scattering can have its origin in the presence of an oxide barrier at the interface or a Fermi velocity mismatch between the materials forming a point contact junction. Along with Andreev reflection, the electron has a finite probability to undergo normal reflection as well. If $A(E)$ and $B(E)$ correspond to probabilities of Andreev reflection and normal reflection respectively, then the current for ballistic point contact geometry between a normal metal

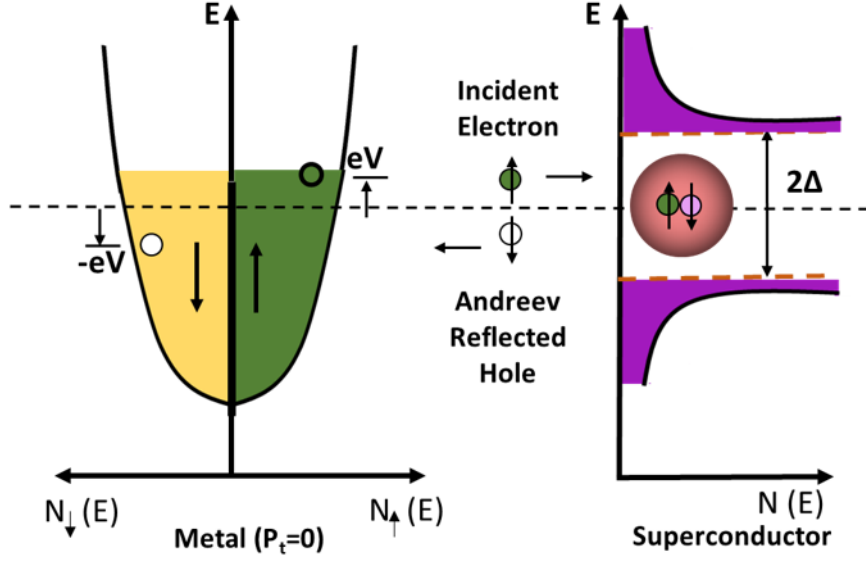


Figure 1.7: Schematic showing Andreev reflection in a junction formed between unpolarized ($P_t = 0$) metal and a conventional superconductor.

and superconductor as per the BTK theory is given by:

$$I_{N/S} \propto N(0) v_F \int_{-\infty}^{\infty} [f_0(E - eV) - f_0(E)][1 + A(E) - B(E)] dE \quad (1.5)$$

where $N(0)$ accounts for the density of states (DOS) at the Fermi level and $f_0(E)$ is the Fermi distribution function given by $f(E) = \frac{1}{\exp \frac{E}{k_B T} + 1}$ for Fermi energy being set to zero. BTK solved the Bogoliubov-de Gennes (BdG) equations [72], given by equation (1.6) and (1.7), to calculate the probabilities at the N/S interface.

$$i\hbar \frac{\partial f(x,t)}{\partial t} = \left(-\frac{\hbar^2 \nabla^2}{2m} - \mu(x) + V(x) \right) f(x,t) + \Delta(x) g(x,t) \quad (1.6)$$

$$i\hbar \frac{\partial g(x,t)}{\partial t} = - \left(-\frac{\hbar^2 \nabla^2}{2m} - \mu(x) + V(x) \right) g(x,t) + \Delta(x) f(x,t) \quad (1.7)$$

where $\Delta(x)$ is the superconducting pairing gap, $\mu(x)$ is the chemical potential, and $V(x)$ is the Hartree potential. $f(x,t)$ and $g(x,t)$ are part of the two-element column vector wavefunction, $\psi = \begin{pmatrix} f(x,t) \\ g(x,t) \end{pmatrix}$, and represents the wavefunction for electron-like and hole-like quasiparticles. Further, $f(x,t)$ and $g(x,t)$ can be expressed in terms of u and v as

$$f(x,t) = u e^{(ikx - \frac{iEt}{\hbar})} \quad (1.8)$$

$$g(x, t) = v e^{(ikx - \frac{iEt}{\hbar})} \quad (1.9)$$

where $E = \sqrt{\left(\frac{\hbar^2 k^2}{2m} - \mu\right)^2 + \Delta^2}$ for $V = 0$. Coefficients u and v can be related as

$$u^2 = \frac{1}{2} \left(1 \pm \frac{(E^2 - \Delta^2)^{\frac{1}{2}}}{E} \right) = 1 - v^2; E > 0 \quad (1.10)$$

Considering the plane wave representation for the electron and hole wavefunction, the wavefunction of the incident electron on the normal metal side (N) can be written as

$$\psi_{inc} = \begin{pmatrix} 1 \\ 0 \end{pmatrix} e^{ikx} \quad (1.11)$$

The reflected wavefunction comprises the wavefunction of normal reflected electron $\begin{pmatrix} 1 \\ 0 \end{pmatrix} e^{-ikx}$ and the Andreev reflected hole $\begin{pmatrix} 0 \\ 1 \end{pmatrix} e^{ikx}$ such that

$$\psi_{ref} = b \begin{pmatrix} 1 \\ 0 \end{pmatrix} e^{-ikx} + a \begin{pmatrix} 0 \\ 1 \end{pmatrix} e^{ikx} \quad (1.12)$$

where $A(E) = a^* a$ and $B(E) = b^* b$. On the superconducting (S) side of the electrode, the transmitted wavefunction can be expressed as

$$\psi_{trans} = c \begin{pmatrix} u \\ v \end{pmatrix} e^{iqx} + d \begin{pmatrix} v \\ u \end{pmatrix} e^{-iqx} \quad (1.13)$$

To calculate the total current through the N-S interface, given by equation (1.5), the value of probabilities $A(E)$ and $B(E)$ needs to be evaluated which can be done by making use of the following boundary conditions:

- (i) The wavefunction should be continuous across the interface *i.e.* $\psi_N(x=0) = \psi_S(x=0)$.
- (ii) The first derivative of the wavefunction should be discontinuous across the interface *i.e.* $\psi'_S(x=0) - \psi'_N(x=0) = \frac{2mV_0}{\hbar^2} \psi_N(x=0)$.

Applying the above boundary conditions and setting $k = q = k_F^*$ where k_F is the Fermi wave vector, the value of $A(E)$ and $B(E)$ for different cases have been listed in Table 1.2.

From equation (1.5), the zero temperature differential conductance can be calculated as $\frac{dI}{dV} \propto [1 + A(E) - B(E)]$. The plots of differential conductance as a function of applied bias V , for different values of Z , when $T=2 K$, and $\Delta = 1.5 meV$, are shown in Figure 1.8. In the limit of a completely transparent barrier ($Z \rightarrow 0$), the conductance within the superconducting gap nearly doubles as most of the incident electrons are Andreev-reflected to a hole resulting

Probability	$E < \Delta$	$E > \Delta$
A(E)	$\frac{(\frac{\Delta}{E})^2}{1 - \varepsilon(1 + 2Z^2)^2}$	$\frac{(uv)^2}{[u^2 - v^2]Z^2 + u^2]^2}$
B(E)	$1 - A(E)$	$\frac{[u^2 - v^2]^2 Z^2 [1 + Z^2]}{[u^2 - v^2]Z^2 + u^2]^2}$

Table 1.2: Probabilities of Andreev reflection and normal reflection, as per BTK theory, for different energy scales. Here, $\varepsilon = \frac{E^2 - \Delta^2}{E^2}$.

in the formation of a Cooper pair carrying double the amount of charge of the incident electrons. For the intermediate barrier limit, two Andreev peaks symmetric about $V=0$ can be seen in the conductance. The BTK analysis of these peaks can give the magnitude of the superconducting gap. In the high-barrier limit ($Z \rightarrow \infty$), the result given by the BTK formalism is essentially the same as that of the tunneling regime. For more complex systems, often a broadening parameter (Γ) is needed and that originates from multiple mechanisms including finite quasiparticle lifetime, distribution of Δ [73] and two-level fluctuations [74].

1.3.4 PCAR as a probe of spin polarization of ferromagnets

When the metal in the metal-superconductor junction is a ferromagnet, that may host a spin-polarised Fermi surface due to an imbalance of density of up and down spin electrons at the Fermi level. In such a situation, all the electrons at the Fermi level cannot undergo Andreev reflection simply because all the corresponding Andreev reflected holes cannot find accessible states in the opposite spin band. This leads to a suppression of Andreev reflection. The schematic, in Figure 1.9, illustrates the Andreev reflection in the case of a junction between a half metal, having spin polarization of 100%, and a conventional superconductor. For ferromagnets, the transport spin polarization usually lies between 0 to 100%. Therefore, by measuring the degree of suppression of Andreev reflection in a ferromagnet-superconductor junction, the magnitude of spin-polarization at the Fermi surface of the ferromagnet can be estimated [75–79]. The spin polarization of the ferromagnet can be defined as

$$P = \frac{N_{\uparrow}(E_F) - N_{\downarrow}(E_F)}{N_{\uparrow}(E_F) + N_{\downarrow}(E_F)} \quad (1.14)$$

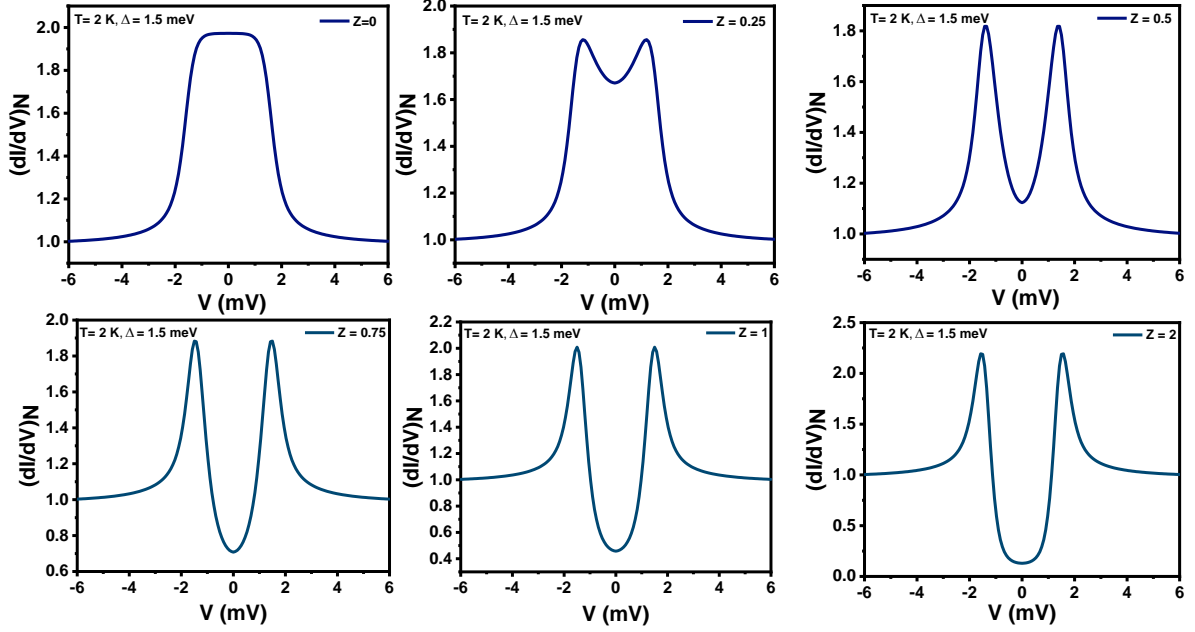


Figure 1.8: Evolution of the $\frac{dI}{dV}$ spectrum with change in the value of Z . The conductance at zero bias becomes suppressed with an increase in the value of Z . The other fitting parameters used are $T=2K$, $\Delta=1.5$ meV, and $\Gamma=0$.

$N_{\uparrow}(E_F)$ is the density of states of spin-up electrons and $N_{\downarrow}(E_F)$ is the density of states of spin-down electrons. However, in real systems, the transport spin polarization doesn't depend on the DOS at the Fermi level alone. Using the Classical Bloch-Boltzmann transport theory, the transport spin polarization can be defined in terms of current densities of up and down spin electrons as follows [62]:

$$P_t = \frac{J_{\uparrow} - J_{\downarrow}}{J_{\uparrow} + J_{\downarrow}}, \quad (1.15)$$

For a ballistic point contact the transport spin polarization can be defined as:

$$P_t = \frac{\langle N(E_F)v_F \rangle_{\uparrow} - \langle N(E_F)v_F \rangle_{\downarrow}}{\langle N(E_F)v_F \rangle_{\uparrow} + \langle N(E_F)v_F \rangle_{\downarrow}}, \quad (1.16)$$

For a diffusive point contact the transport spin polarization can be defined as:

$$P_t = \frac{\langle N(E_F)v_F^2 \rangle_{\uparrow} - \langle N(E_F)v_F^2 \rangle_{\downarrow}}{\langle N(E_F)v_F^2 \rangle_{\uparrow} + \langle N(E_F)v_F^2 \rangle_{\downarrow}}, \quad (1.17)$$

$\langle v_F \rangle$ is the average spin-polarized Fermi velocity. In the case of a ferromagnet-superconductor junction, the PCAR spectra can be calculated using the modified BTK theory [75] as discussed below.

By renaming the probabilities $A(E)$ and $B(E)$ in equation (1.5) as $A_u(E)$ and $B_u(E)$, where the subscript u represents unpolarized current, we can rewrite equation (1.2) as fol-

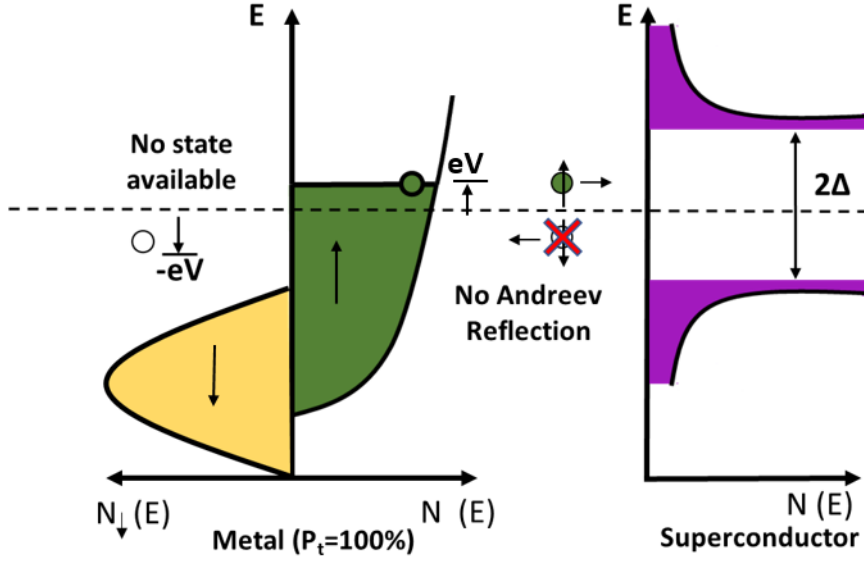


Figure 1.9: (a) Schematic showing Andreev reflection in a point contact junction formed between fully polarized ($P_t = 100\%$) metal and a conventional superconductor.

lows:

$$I_u \propto N(0)v_F \int_{-\infty}^{\infty} [f(E - eV) - f(E)][1 + A_u(E) - B_u(E)]dE \quad (1.18)$$

To calculate the fully polarized current I_p , equation (1.15) can be employed by replacing A_u and B_u with A_p and B_p , respectively, where the latter represents the corresponding probabilities for the fully polarized case. The coefficients A_p and B_p can be determined using the same boundary conditions as discussed in the previous section. Table 1.3 provides the values of probabilities A_p and B_p for various energies.

The total current in terms of I_u and I_p can then be written as

$$I_{total} = (1 - P_t)I_u + P_t I_p \quad (1.19)$$

where P_t is one of the fitting parameters of the modified BTK theory which gives an estimate of the value of transport spin polarisation [62, 75]. To summarize, the magnitude of transport spin polarization can be estimated by following the algorithm: (i) Calculate the BTK current for the unpolarized case (I_u), (ii) Calculate the BTK current for the fully polarized case spin polarization is 100 percent (I_p), (iii) Find an intermediate total polarization current by interpolation between I_u and I_p using equation (1.19). The derivative of I_{total} with respect

Probability	$E < \Delta$	$E > \Delta$
$A_p(E)$	0	0
$B_p(E)$	1	$\frac{(\sqrt{\frac{E^2-\Delta^2}{E^2}} - 1)^2 + 4Z^2(\frac{E^2-\Delta^2}{E^2})}{(\sqrt{\frac{E^2-\Delta^2}{E^2}} + 1)^2 + 4Z^2(\frac{E^2-\Delta^2}{E^2})}$

Table 1.3: Probabilities $A_p(E)$ and $B_p(E)$.

to V gives the modified Andreev reflection spectrum with finite spin polarization in the ferromagnet. Figure 1.10 depicts representative spectra for different values of transport spin polarization P_t while keeping T , Δ , and Z fixed at 2 K, 1.5 meV, and 0, respectively. It can be observed that as P_t approaches 100%, the differential conductance at zero bias tends to zero, indicating complete suppression of Andreev reflection in a half metal, as illustrated in Figure 1.10.

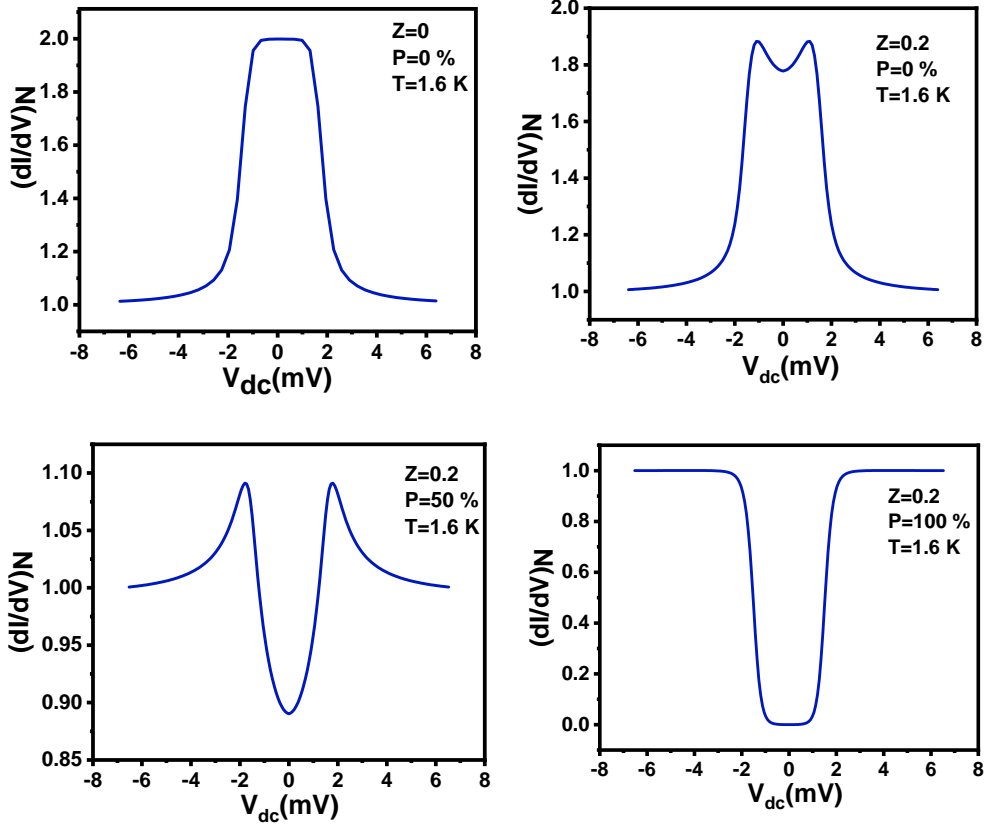


Figure 1.10: PCAR spectra for different values of transport spin polarization P_t and Z .

1.4 Heavy Fermion systems

Fe_3GeTe_2 shows an emergent Kondo lattice behavior, along with a large effective carrier mass, imparting a heavy fermionic character to the system [57, 58]. Here, we delve into a brief discussion of such systems. In heavy fermion systems, the itinerant conduction electrons strongly interact with localized magnetic moments associated with the f or d electrons. These strong electron-electron interactions give rise to a many-body state in which the effective mass of the charge carriers becomes significantly larger than their bare mass. As per Landau's Fermi liquid framework, the linear specific heat coefficient also known as the Sommerfeld coefficient ($\gamma_{\text{Sommerfeld}}$) which signifies the electronic contribution to specific heat, is directly proportional to the density of states (ρ^*) of quasiparticles and, consequently, to their effective mass (m^*). The Sommerfeld coefficient is given by:

$$\gamma_{\text{Sommerfeld}} = \frac{\pi^2 k_B^2}{3} \rho^* = \frac{k_F k_B^2}{3 \hbar^2} m^* \quad (1.20)$$

In conventional metals, $\gamma_{\text{Sommerfeld}}$ ranges between 1 and 10 mJ/molK². However, in heavy fermionic systems, this coefficient can exhibit much larger values ranging between 10-1000 mJ/molK², indicating the significant heaviness of the charge carriers in these materials [80].

The heavy fermion behavior is typically observed at low temperatures, typically below a characteristic energy scale known as the Kondo temperature (T_K). Below T_K , the localized magnetic moments are effectively screened by the conduction electrons, forming a coherent, heavy quasiparticle state.

1.4.1 The single impurity Anderson Model

It is important to first gain an insight into the physics underlying the formation of local moments which can be explained using Anderson's single impurity model [81]. As per the model,

$$H = \sum_{k\sigma} \epsilon_k c_{k\sigma}^\dagger c_{k\sigma} + \epsilon_d n_d + U n_{d\uparrow} n_{d\downarrow} + \sum_{k\sigma} V_{k\sigma} [d_\sigma^\dagger c_{k\sigma} + c_{k\sigma}^\dagger d_\sigma] \quad (1.21)$$

The first term gives the kinetic energy of the de-localized conduction electrons. The second term describes an energy of localized d or f electrons in impurity ion. The third term gives the on-site Coulomb repulsion at the impurity site. The last term describes the hybridization of the delocalized conduction electrons with localized moments of the impurity ion. c and d are the annihilation operators for conduction electrons and localized electrons for d orbitals respectively. In the atomic limit (neglecting hybridization, $V = 0$),

$$H_{atom} = \epsilon_d n_d + U n_{d\uparrow} n_{d\downarrow} \quad (1.22)$$

There can exist 4 quantum states with respective energies: $|d^0 \rangle: E(d^0) = 0$; $|d^2 \rangle: E(d^2) = 2\epsilon_d + U$; $|d^1 \uparrow \rangle, |d^1 \downarrow \rangle: E(d^1) = \epsilon_d$. Out of these $|d^0 \rangle$ and $|d^2 \rangle$ are non-magnetic. For the magnetic doublet ($|d^1 \uparrow \rangle, |d^1 \downarrow \rangle$) the cost of adding or removing an electron from the d orbital is given by:

$$\text{removing} : E(d^0) - E(d^1) = -\epsilon_d > 0 \quad (1.23)$$

$$\text{adding} : E(d^2) - E(d^1) = \epsilon_d + U > 0 \quad (1.24)$$

The difference between the energies in equation (1.23) and (1.24) being $\Delta E = \frac{U}{2} \pm (\epsilon_d + \frac{U}{2})$. This sets the condition for the existence of local moment given by:

$$\frac{U}{2} > |\epsilon_d + \frac{U}{2}| \quad (1.25)$$

Therefore, the energy is lowest when the d orbital is singly occupied resulting in a non-zero magnetic moment. For the condition in equation (1.25) to be met, U must be large and thermal excitations should be small i.e. $k_B T < \max(\epsilon_d + U, -\epsilon_d)$.

In the scenario where hybridization is present but on-site Coulomb repulsion is absent,

the d electrons engage in hybridization with the conduction electrons, leading to the formation of a resonant state [82]. The width of this resonant state, denoted as w , is given by $w = \pi V^2 \rho$, where V^2 represents the average strength of hybridization and ρ corresponds to the density of states (DOS) of the conduction electrons at the Fermi level. In the situation where both terms in the Hamiltonian given by equation (1.21) are non-zero, Anderson employed a mean-field treatment to demonstrate that when the on-site Coulomb repulsion exceeds a critical value of approximately $U_c \approx \pi w$, local moments are formed with a non-zero magnetization. The interaction between the conduction electrons and these localized moments gives rise to various intriguing quantum phenomena, among which the Kondo effect stands out as one notable effect.

1.4.2 Kondo effect

Matthiessen's rule of electrical resistivity states that the total resistivity of a metal can be regarded as the sum of individual resistivities due to different scattering mechanisms present in the material. The resistivity of a normal metal can be expressed as

$$\rho(T) = \rho_o + a\rho(T^2) + b\rho(T^5) \quad (1.26)$$

where ρ_o is the zero temperature resistivity, also termed as residual resistivity, that originates from carrier scattering from impurity or defects. The T^2 dependence of resistivity originates from the electrons-electron interactions while the T^5 dependence originates from electron-phonon interaction. However, resistivity in some metals when doped with magnetic impurities is not found to saturate at low temperatures. Instead, below a certain temperature (T_K) known as the Kondo temperature, the resistivity increases with the decrease in temperature. This effect was first discovered by W. J. de Haas, J. de Boer and G.J. van den Berg in 1934 in impure gold wires [83]. The origin of the resistivity minimum in such systems was explained by Jun Kondo [84], in 1964, using second-order perturbation theory. He reasoned that the resistance minimum occurs due to the electron spin-flip scattering processes where a temporary spin exchange happens between the conduction electrons and localized moments associated with the magnetic impurity (Figure 1.11 (a)). This process can be explained as follows: Suppose we have a magnetic ion that is situated within a metallic lattice, the energy of the highest energy electron associated with the impurity being lower than the energy of the electrons in the Fermi sea. As per the Heisenberg uncertainty principle, it is possible for the magnetic impurity's electron to spontaneously tunnel from the impurity to the Fermi sea of the lattice within a timescale constrained by the uncertainty principle. Simultaneously, an electron from the Fermi sea can tunnel to the available state in the impurity. Importantly, in this latter case, the spins of these two electrons are not necessarily required to be identical, allowing for a spin exchange to take place. The occurrence of spin exchanges brings

about a notable change in the overall energy spectrum of the system. When numerous spin exchanges take place, this many-body phenomenon leads to the system transitioning into a new state. This new state, known as a Kondo resonance, possesses the same energy as the Fermi level. It effectively scatters electrons whose energies are also near the Fermi level, specifically the conduction electrons. As these conduction electrons undergo scattering, we observe a corresponding increase in resistivity within the bulk state of the material [85]. It is important to note that this phenomenon primarily occurs at low temperatures since the Fermi distribution, which governs the distribution of filled and unfilled states, broadens as the temperature rises. For the spin exchange to occur and have a significant impact compared to other scattering processes, the energies of the conduction electrons must be in close proximity to the Fermi energy. Therefore, at low temperatures, the resistivity of such systems gets modified to

$$\rho(T) = \rho_o + c \ln\left(\frac{\mu}{T}\right) + b\rho(T^5) \quad (1.27)$$

where the logarithmic term in equation (1.27) produces a resistivity minima at $T_{minimum} = \left(\frac{c}{5b}\right)^{\frac{1}{5}}$.

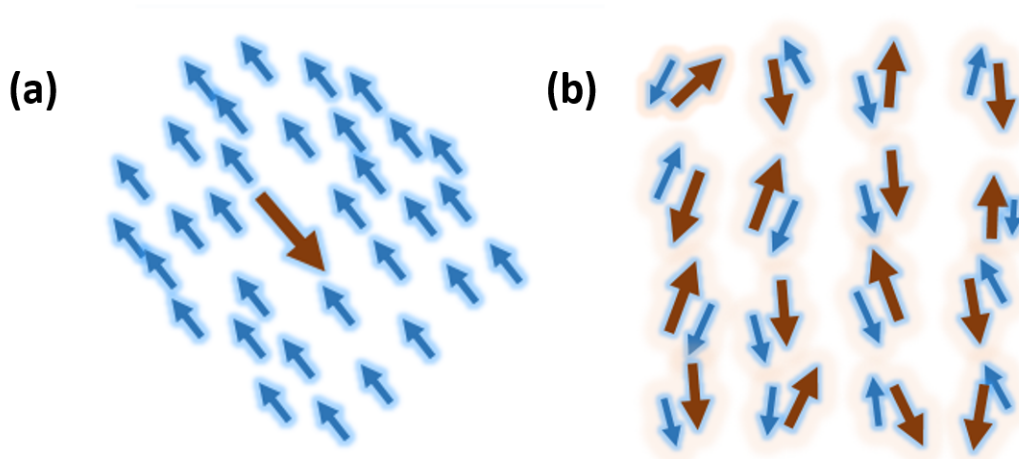


Figure 1.11: Schematic depicting the hybridization (screening) of the localized moments (red arrows) with the conduction electrons (blue arrows) in (a) a single-impurity Kondo effect (b) and a Kondo lattice.

1.4.3 Kondo lattice

We have aforementioned the interaction of localized moments of a single impurity with the conduction electrons. If a periodic array of such localized moments is embedded in a sea of conduction electrons, the interaction between the two leads to the formation of a Kondo lattice (Figure 1.11 (b)). The experimental signature of Kondo effect can be found in the

tunneling experiments. When an electron enters a Kondo lattice (Figure 1.12), it triggers a cotunneling mechanism that leads to a simultaneous spin flip of the localized moments [86]. The differential tunneling conductance of such a system, in the clean limit, exhibits a double peak antisymmetric spectra separated by the hybridization gap. The peak structure gets smeared out as one reaches the dirty limit. Within this picture, even with the moderate disorder, the conductance spectrum is expected to take the shape of a Fano line [87]. The Fano lineshape is given by [87]:

$$dI/dV \propto \frac{(\varepsilon + q)^2}{1 + \varepsilon^2}; \varepsilon = \frac{eV - \varepsilon_0}{\Gamma} \quad (1.28)$$

Here, V is the applied dc bias, q is the Fano asymmetry factor, ε_0 is the position of the resonance in the energy scale, Γ is the resonance at HWHM (half width at half maximum). Such Fano lineshape behavior was experimentally observed in Point contact spectroscopy (PCS) and Scanning tunneling spectroscopy (STS) with a number of heavy fermion systems like CeCoIn₅ [88], CeCu₂Si₂, URu₂Si₂ [92], UBe₁₃, UPt₃ [93], UTe₂ [94], etc. The presence of an anti-symmetric Kondo background can lead to an extra suppression in the Andreev reflection in PCAR measurements.

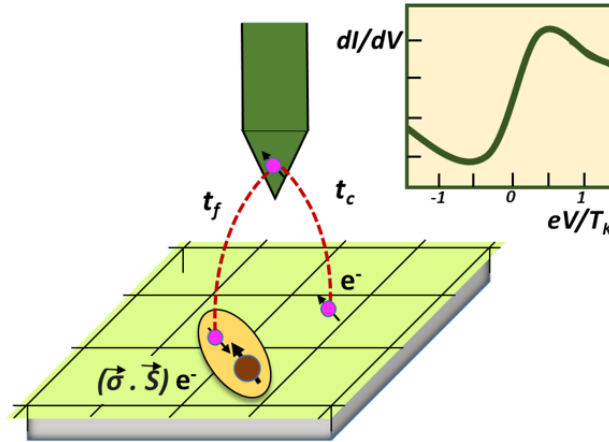


Figure 1.12: Schematic illustrating electron tunneling into a Kondo Lattice where t_c gives the direct tunneling amplitude into the sea of conduction electrons and t_f gives the tunneling amplitude into the composite state made from the hybridization of the localized moments and conduction electrons. Inset shows the typical Fano line behavior observed, in the tunneling conductance, for a Kondo lattice.

1.5 Topological Superconductivity

Another area where spin-polarized fermions are known to play a significant role is topological superconductivity. Within the Bogoliubov-de Gennes (BdG) description of superconductivity, the negative energy single-particle states are filled. The positive and the negative energy states are separated by a pairing energy called the superconducting energy gap (2Δ) [9, 95]. By construction, this is similar to an insulator where the valence band (states below the Fermi energy E_F) is filled which is separated from the conduction band by an insulating energy gap. This similarity prompted the question of the possibility of a superconducting analogue of a topological insulator where a non-zero topological invariant defined in the filled band gives rise to a band structure that is topologically distinct from a trivial band insulator [97–99]. Theoretically, it is understood that in the case of a superconductor, if a non-zero topological invariant can be found for the filled states in the BdG picture, it is possible to obtain a topologically distinct superconducting phase where the gap will be non-zero in the bulk, but the gap will close at the surface due to the emergence of self-Hermitian surface modes called the Majorana modes [100–104]. Such a special class of superconductors is termed ‘Topological Superconductors’ [100–104]. Majorana modes in such superconductors are a direct consequence of the boundary correspondence of the topologically non-trivial bulk.

Conventional s -wave superconductors, where Cooper pair formation involves the pairing of opposite spin electrons ($S=0$), are ubiquitous in the sense that most of the known superconducting materials exhibit conventional s -wave pairing. This makes the s -wave superconductors the natural starting point for exploring the potential topological character of superconductors. However, the Bogoliubov operators defined for conventional s -wave superconductors don’t follow the expected Majorana nature i.e $\gamma_{k\uparrow}^\dagger = u_k c_{k\uparrow}^\dagger + v_k c_{-k\downarrow} \neq \gamma_{-k\downarrow}$. This discrepancy arises from the different spin projections of electrons, leading to non-self-conjugate quasiparticle operators. The effect of spin can be eliminated in p -wave superconductors, also termed ‘spinless superconductors’. In these superconductors, the Cooper pairing results from the pairing of spin-polarised electrons ($S = 1$) and hence have only a single active spin degree of freedom. Due to particle-hole symmetry in these superconductors, the creation operator for a quasiparticle in state ψ_E is equivalent to the annihilation operator for a quasiparticle in state ψ_{-E} (Figure 1.13(a)), denoted as $\gamma_E^+ = \gamma_{-E}$. These states possess topological triviality since they can be affected by perturbations that drive them into or out of the energy gap. However, a state at zero energy exhibits topological non-triviality. These mid-gap excitations demonstrate the Majorana nature of spinless quasiparticles, represented by $\gamma_0^+ = \gamma_0$, implying that the quasiparticle is its own antiparticle (Figure 1.13(b)). This unpaired bound state at zero energy remains fixed at $E = 0$ unless the energy gap closes [100]. If these topologically-protected modes can be realized experimentally, they hold the poten-

tial to achieve fault-tolerant quantum computing. [105–111].

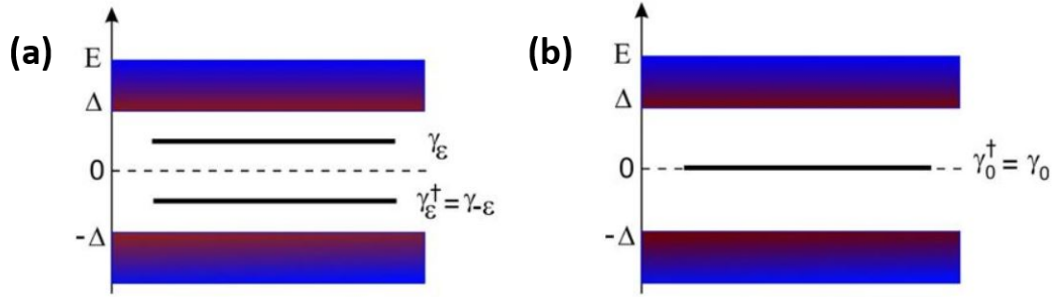


Figure 1.13: (a) For every state E in the superconducting gap there exists a state at $-E$ as a consequence of particle-hole symmetry. (b) The mid-gap excitations of the topological superconductor will lead to a topologically protected unpaired Majorana bound state at zero energy as it cannot be moved away from $E=0$ unless the gap closes.

1.5.1 Majorana Zero energy modes.

In second quantization language creation c_i^\dagger and annihilation operators c_i can be used to represent Fermions. These operators obey Fermion algebra i.e. they obey anticommutation relation:

$$\{c_i^\dagger, c_j^\dagger\} = 0; \{c_i, c_j\} = 0; \{c_i^\dagger, c_j\} = \delta_{ij} \quad (1.29)$$

Without any loss of generality, these operators can be expressed in terms of a set of new operators $\gamma_{i,1}$ and $\gamma_{i,2}$ such that

$$\begin{aligned} c_i &= \frac{\gamma_{i,1} + i\gamma_{i,2}}{2} \\ c_i^\dagger &= \frac{\gamma_{i,1} - i\gamma_{i,2}}{2} \end{aligned} \quad (1.30)$$

On inversion,

$$\begin{aligned} \gamma_{i,1} &= (c_i + c_i^\dagger) \\ \gamma_{i,2} &= i(c_i - c_i^\dagger) \end{aligned} \quad (1.31)$$

These operators follow the anti-commutation relations:

$$\{\gamma_{i\alpha}, \gamma_{j\beta}\} = 2\delta_{ij}\delta_{\alpha\beta} \quad (1.32)$$

with

$$\gamma^2 = 1 \quad (1.33)$$

i.e. the operator γ being necessarily self adjoint. This implies

$$\gamma_{i,\alpha}^\dagger = \gamma_{i,\alpha} \quad (1.34)$$

i.e. a particle created by γ operator is identical to its antiparticle. So we can term $\gamma_{i,1}$ and $\gamma_{i,2}$ as the Majorana operators.

An inference can be made that a Fermionic state can be recast into the real and imaginary parts with each part corresponding to Majorana Fermion through canonical transformations shown in equation (1.34). This recasting doesn't have any physical consequences because the Majorana pair remains spatially localized and overlap significantly to be considered as separate entities. However, in the context of topological superconductors, an intriguing phenomenon arises where Majorana fermions bound at the edges can become spatially separated, with the potential for significant localization even at considerable distances. This spatial separation provides protection against local perturbations or decoherence. Equation (1.33) further emphasizes the distinction between Majorana operators and fermionic operators by demonstrating that the action of the Majorana operator twice on state results in the same state.

1.5.2 Kitaev model of topological superconductivity

The toy model to realize unpaired or spatially separated MZMs in spinless p-wave superconductors was proposed by Alexei Kitaev in 2001 [112]. To understand this model, let's consider a system with $i = N$ sites where each site can host one fermion as per the Pauli exclusion principle such that by definition each site can host two different Majorana modes $\gamma_{i,A}$ and $\gamma_{i,B}$ (Figure 1.14).



Figure 1.14: Schematic illustrating N sites 1-D Kitaev chain, where each fermionic site can host two Majorana modes

The tight binding Hamiltonian for such a 1-D chain with p-wave superconducting pairing can be expressed as

$$H = -\mu \sum_i (n_i) - t \sum_i (c_i^\dagger c_{i+1} + c_{i+1}^\dagger c_i) + \sum_i (\Delta c_i c_{i+1} + \Delta^* c_{i+1}^\dagger c_i^\dagger) \quad (1.35)$$

where μ is the chemical potential, t is nearest neighbor hopping amplitude, $n = c_i^\dagger c_i$ is the

number operator and Δ is the superconducting pairing potential $\Delta = |\Delta| \exp(i\phi)$. For sake of simplicity, we consider Δ to be real i.e. $\phi = 0$. Unlike BCS Hamiltonian, Kitaev Hamiltonian doesn't have spin dependence because electrons are assumed to have one spin direction i.e. effectively spinless system. This leads to odd superconducting pairing i.e. coupling of same spin electrons.

In Majorana representation equation (1.35) can be rewritten as

$$H = -\frac{\mu}{2} \sum_i^N (1 + i\gamma_{i,B}\gamma_{i,A}) - \frac{it}{2} \sum_i^{N-1} (\gamma_{i+1,A}\gamma_{i,B} + \gamma_{i,A}\gamma_{i+1,B}) + \frac{i|\Delta|}{2} \sum_i^{N-1} (\gamma_{i,B}\gamma_{i+1,A} + \gamma_{i,A}\gamma_{i+1,B}) \quad (1.36)$$

Using the anti-commutation relation equation (1.36) can be expressed as

$$H = -\frac{i\mu}{2} \sum_i^N (\gamma_{i,A}\gamma_{i,B}) + \frac{i(t + |\Delta|)}{2} \sum_i^{N-1} (\gamma_{i,B}\gamma_{i+1,A}) + \frac{i(|\Delta| - t)}{2} \sum_i^{N-1} (\gamma_{i,A}\gamma_{i+1,B}) \quad (1.37)$$

Depending on the values of t , Δ and μ , two special cases can be considered:

Case 1: When $t = |\Delta| = 0$ and $\mu \neq 0$, the Hamiltonian given by equation (1.37) takes the form

$$H = -\frac{i\mu}{2} \sum_i^N (\gamma_{i,A}\gamma_{i,B}) = -\mu \sum_i^N c_i^+ c_i \quad (1.38)$$

This is a topologically trivial phase where only pairing between Majoranas at the same sites

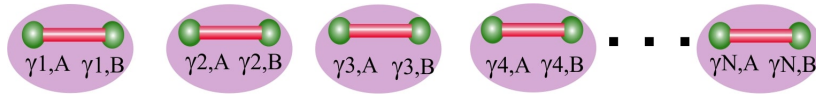


Figure 1.15: Schematic illustrating pairing between Majoranas present at the same fermionic site for the case when $\mu \neq 0, t = |\Delta| = 0$.

is effective and no unpaired Majorana modes appear as shown in Figure 1.15. The energy cost of filling a fermion at a particular site is finite and is equal to μ .

Case 2: When $\mu = 0, t = \Delta \neq 0$, the Hamiltonian takes the form

$$H = it \sum_i^{N-1} \gamma_{i,B}\gamma_{i+1,A} \quad (1.39)$$

This leads to the coupling of Majorana at a given site to those at the adjacent neighboring

site as shown in Figure 1.16. It is evident from equation (1.39) that two Majorana modes at the edges of the chain $\gamma_{1,A}$ and $\gamma_{N,B}$, which are basically Zero energy MZMs, are missing from the Hamiltonian and are unpaired. To add a fermion at any site on the chain except the edge modes, energy cost is equivalent to t . The bulk is gapped and $2t$ is the energy gap between the filled and the empty states. The two unpaired MZMS can be combined to form

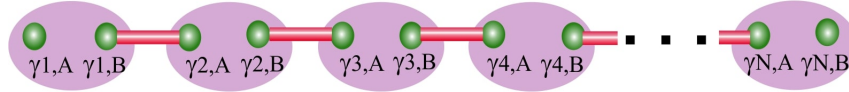


Figure 1.16: Schematic illustrating pairing of Majoranas at adjacent neighboring sites for the case when $\mu = 0, t = |\Delta| \neq 0$ leading to unpaired Majorana modes $\gamma_{1,A}$ and $\gamma_{N,B}$ localized at opposite ends of 1-D Kitaev chain

a highly non-local operator by

$$d_M = \frac{1}{2}(\gamma_{1,A} + \gamma_{N,B}) \quad (1.40)$$

The term 'non-local' is associated with d_M in the sense that the $\gamma_{1,A}$ and $\gamma_{N,B}$ comprising this fermionic operator are localized at the opposite ends of the Kitaev chain. Occupying the corresponding state will not cost any energy.

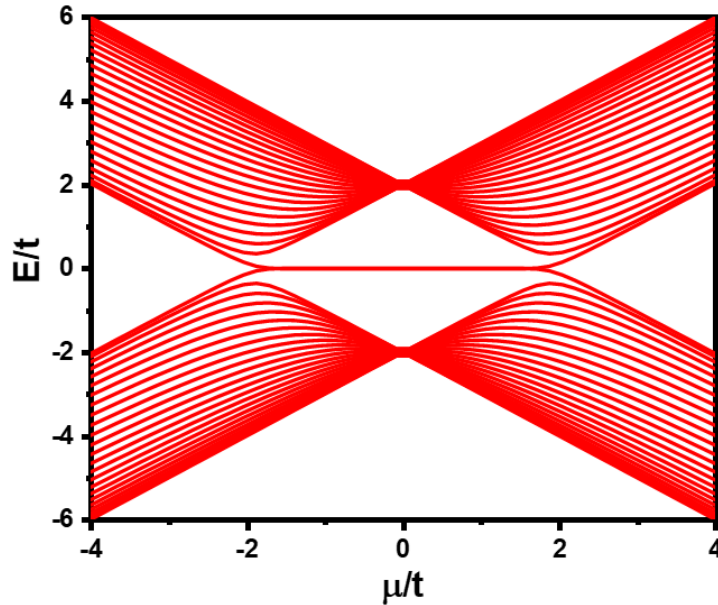


Figure 1.17: Energy spectrum of Kitaev chain w.r.t to μ plotted for $|\Delta| = 1, t=1$. Phase transition between the topological phases taking place at $|\mu| = 2t$.

Although occupation numbers cannot be defined for Majorana modes, we can assign a number operator to d_M , which is constructed from these unpaired Majorana zero modes (MZMs). Depending on the eigenvalue of the number operator, parity can be defined as

even corresponding to the number operator being 0, and odd corresponding to the number operator being 1. While the non-degenerate ground state of a conventional superconductor being condensate of Cooper pair has even parity, the doubly degenerate ground state in this case can have odd parity i.e. odd number of quasiparticles at zero energy cost. This corresponds to the topologically non-trivial phase.

Based on the specific set of parameters, we have categorized the cases mentioned above into two groups: topological trivial and non-trivial phases. However, the presence of the topologically non-trivial phase is maintained as long as the condition $|\mu| < 2t$ is satisfied. This implies that zero-energy Majorana modes will persist as long as the bulk of the system remains completely gapped. Conversely, if $|\mu| > 2t$, the system transitions into a topologically trivial phase. In the presence of periodic boundary conditions, the Hamiltonian in momentum space can be written as:

$$H = \sum_k (-2t \cos(k) - \mu) c_k^\dagger c_k + \Delta (i \sin(k)) c_k c_{-k} + h.c. \quad (1.41)$$

with the excitation spectrum of the form

$$E(k) = \pm \sqrt{(2t \cos(k) + \mu)^2 + (2\Delta \sin(k))^2} \quad -\pi < k < \pi \quad (1.42)$$

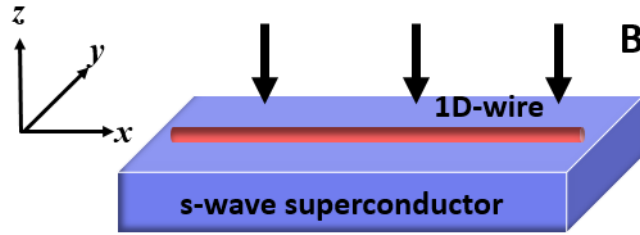


Figure 1.18: Schematic showing a semiconducting Rashba spin-orbit coupled nanowire lying along x -axis in proximity to an s -wave superconductor. The external magnetic field is applied along the z -axis.

As depicted in Figure (1.17) at $\mu = 2t$, the band closes leading to the direct coupling between MZMs and bulk states resulting in the recombination of MZMs to electrons and filling of the first empty energy band. In conclusion, choosing the different values of nearest neighbor hopping amplitude and on-site energy (chemical potential) leads to two distinct topological phases i.e trivial topological phase with no Majorana modes and the non-trivial

topological phase with Majorana edge modes where the two phases can be distinguished on the basis of presence or absence of unpaired MZMs at the ends of the Kitaev chain.

1.5.3 Physical Realization of Kitaev Model

In the absence of clear evidence of a p -wave superconductor in practice, a 1D model involving an s -wave superconductor in the proximity of a Rashba-coupled semiconductor under a perpendicular Zeeman field can host similar topologically protected Majorana edge modes [113, 114]. The schematic of the system is shown in Figure 1.18. The Hamiltonian of the system can be written as

$$H_{\text{sys}} = \left(-\frac{1}{2m}\partial_x^2 + i\alpha\sigma_y\partial_x\right)\tau_z - V_z\sigma_z + \Delta\tau_x \quad (1.43)$$

where m, α, μ and Δ is the effective mass, Rashba spin orbit coupling, chemical potential and superconducting energy gap proximity induced in the nanowire due to underlying s -wave superconductor respectively. Discretizing the continuous Hamiltonian in equation(1.43) results in:

$$H_{\text{sys}} = \sum_{n=1}^N \left[-t(|n+1\rangle\langle n| + H.c.)\tau_z + i\alpha(|n+1\rangle\langle n| - H.c.)\sigma_y\tau_z + \Delta|n\rangle\langle n|\tau_x + (-\mu)|n\rangle\langle n|\tau_z - V_z|n\rangle\langle n|\sigma_z \right] \quad (1.44)$$

where $t = \frac{\hbar^2}{2ma^2}$ gives the hopping amplitude and a is the lattice constant. It is well known from the theoretical as well as experimental results that for a 1-D wire, a phase transition from the topologically trivial regime (no Majorana bound state) to topologically non-trivial regime (with Majorana bound state) can be achieved by setting Zeeman field $V_z > \sqrt{\mu^2 + \Delta^2}$ [113, 114]. Since such edge modes are protected precisely at zero energy, one of the potential experimental signatures of that could be a robust zero-bias conductance peak (ZBCP) in a tunneling experiment [115–122]. The differential conductance of a 1D nanowire can be measured by attaching a normal lead/ metal electrode at one end of the proximitized superconducting nanowire as shown in Figure 1.19. The normal lead has the same Hamiltonian (equation (1.44)) as the nanowire except that the superconducting pairing term (Δ) is taken to be zero for the normal lead. Choosing the chemical potential of the lead greater than the superconducting gap provides the provision of fixing the lead always in the topologically trivial regime. At the interface of normal lead-superconducting nanowire junction, tunnel barrier is modelled by adding an additional onsite energy of strength $10t$ on one end (left) of the wire. The tunnel barrier potential added in the model to account for the

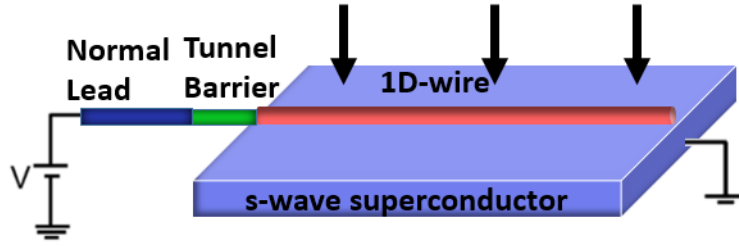


Figure 1.19: The tunneling conductance setup consisting of Majorana nanowire (in red) connected to the normal leads (in blue) with a barrier potential (in green) existing at the interface of the junction. A bias V is applied to the normal leads.

interfacial scattering can have its origin in the presence of an oxide barrier on the nanowire or Fermi velocity mismatch between the leads of different materials forming the junction. If there are N conducting channels in the lead then the zero temperature differential conductance can be calculated using the Blonder-Tinkham-Klapwijk (BTK) formula (in the units of e^2/h) [71]. The differential conductance plot as a function of applied bias V to the leads is shown in Figure 1.20. The tunneling conductance of the nanowire in the topologically non-trivial regime leads to quantized conductance of $\frac{2e^2}{h}$ due to perfect Andreev reflection which is a consequence of the formation of Majorana modes at the edges of the nanowire.

As discussed above, one of the possible signatures of such modes is the appearance of a zero-bias conductance peak (ZBCP) in tunneling experiments [115, 118]. However, it is also known that a peak at zero bias can have origins due to non-Majorana sources as well such as Andreev bound states, weak antilocalization, or Kondo resonance [123–127] making the confirmation of Majorana modes challenging. As a consequence, as far as the experimental detection of these modes is concerned, they have remained elusive. We have theoretically proposed a tunneling setup consisting of an array of weakly coupled Majorana nanowires, a quasi-two-dimensional topological superconductor, which can be used in the detection of these topologically non-trivial modes in a more controlled and effective manner [128]. In our setup, the ZBCP can be turned *OFF* and *ON* depending on the parity of the transport active wires leading to an odd-even-like effect in the tunneling conductance, providing a more comprehensive signature of these modes. In addition, we have studied the effect of the magnetic field angle on the odd-even effect where the field tilt angle can be used as another tuning parameter to confirm the Majorana-origins of ZBCP.

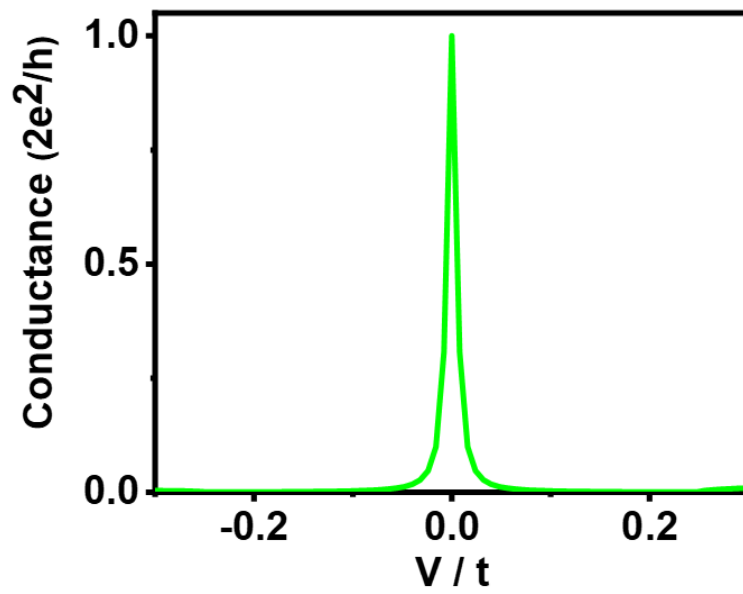


Figure 1.20: The differential conductance (in units of $2\frac{e^2}{h}$) for a single nanowire in the topological regime. For calculations, the values used are $\alpha = 1t$, $\mu = -2t$, and $\Delta = 0.6t$, $V_z = 0.85t$.

Bibliography

- [1] M. M. Waldrop, *Nature* **530**, 144–147 (2016) .
- [2] A. Hirohata, K. Yamada, Y. Nakatani, I.-L. Prejbeanu, B. Diény, P. Pirro and B. Hillebrands *J. Magn. Magn. Mater.* **509**, 166711 (2020).
- [3] S. A. Wolf, D. D. Awschalom, R. A. Buhrman, J. M. Daughton, S. von Molnár, M. L. Roukes, A. Y. Chtchelkanova, D. M. Treger *Science* **294**, 5546 (2001).
- [4] I. Žutić, J. Fabian, and S. D. Sarma *Rev. Mod. Phys.* **76**, 323 (2004).
- [5] S.D. Bader and S.S.P. Parkin *Ann. Rev. of Cond. Matt. Physics* **1**, 71 (2010).
- [6] M. N. Baibich, J. M. Broto, A. Fert, F. Nguyen Van Dau, F. Petroff, P. Etienne, G. Creuzet, A. Friederich, and J. Chazelas *Phys. Rev. Lett.* **61**, 2472 (1988).
- [7] S. Tehrani, B. Engel, J.M. Slaughter, E. Chen, M. DeHerrera, M. Durlam; P. Naji, R. Whig, J. Janesky, and J. Calder *IEEE Transactions on Magnetics* **36**, 2752 - 2757 (2000).
- [8] S. Bhatti, R. Sbiaa, A. Hirohata, H. Ohno, S. Fukami, and S.N. Piramanayag *Materials Today* **20**, 530-548 (2017).
- [9] A. Fert *Rev. Mod. Phys.* **80**, 1517 (2008).
- [10] E. C. Ahn *npj 2D Mater Appl* **4**, 17 (2020).
- [11] G. Hu and B. Xiang *Nanoscale Res. Lett.* **15**, 226 (2020).
- [12] Y. Liu, C. Zeng, J. Zhong, J. Ding, Z. M. Wang and Z. Liu *Nano-Micro Lett.* **12**, 93 (2020).
- [13] W. Han *App. Phys. Lett.* **4**,032401 ((2016).

- [14] H. Yang, S. O. Valenzuela, M. Chshiev, S. Couet, B. Dieny, B. Dlubak, A. Fert, K. Garello, M. Jamet, D.-E. Jeong, K. Lee, T. Lee, M.-B. Martin, G. S. Kar, P. S  n  or, H.-J. Shin and S. Roche *Nature* **606**, 663–673 (2022).
- [15] J.F. Sierra, J. Fabian, R. K. Kawakami, S. Roche and S. O. Valenzuela *Nature Nanotechnol* **16**, 856–868 (2021)
- [16] X. Lin, W. Yang, K. L. Wang, and W. Zhao *Nat Electron* **2**, 274-283 (2019)
- [17] J.-F. Dayen, S.J. Ray, O. Karis, I. J. V.-Marun and M. V. Kamalakar *Appl. Phys. Rev*, **7**, 011303 (2020)
- [18] C. Gong and X. Zhang *Appl. Phys. Rev*, **7**, 011303 (2020)
- [19] G. Fiori, F. Bonaccorso, G. Iannaccone, T. Palacios, D. Neumaier, A. Seabaugh, S. K. Banerjee, and L. Colombo *Nat. Nanotech.* **9**, 768–779 (2014) (2014)
- [20] K. S. Novoselov, A. K. Geim, S. V. Morozov, D. Jiang, Y. Zhang, S. V. Dubonos, I. V. Grigorieva, A. A. Firsov *Science* **306**, 666-669 (2004)
- [21] G. Chen, L. Jiang, S. Wu, B. Lyu, H. Li, B. L. Chittari, K. Watanabe, T. Taniguchi, Z. Shi, J. Jung, Y. Zhang, and F. Wang. *Nat. Phys.* **15**, 666-237–241,(2019).
- [22] A. L. Sharpe, E. J. Fox, A. W. Barnard, J. Finney, K. Watanabe, T. Taniguchi, M. A. Kastner, and D. Goldhaber-Gordon. *Science* **365**, 605–608,(2019).
- [23] G. Chen, A. L. Sharpe, E. J. Fox, Y.-H. Zhang, S. Wang, L. Jiang, B. Lyu, H. Li, K. Watanabe, T. Taniguchi, Z. Shi, T. Senthil, D. Goldhaber-Gordon, Y. Zhang, and F. Wang. *Nature* **579**, 56–61,(2020).
- [24] M. Serlin, C. L. Tschirhart, H. Polshyn, Y. Zhang, J. Zhu, K. Watanabe, T. Taniguchi, L. Balents, and A. F. Young. *Science* **367**, 900-903,(2020).
- [25] H. Polshyn, J. Zhu, M. A. Kumar, Y. Zhang, F. Yang, C. L. Tschirhart, M. Serlin, K. Watanabe, T. Taniguchi, A. H. MacDonald, and A. F. Young. *Nature* **588**, 66–70,(2020).
- [26] Y. Cao, V. Fatemi, A. Demir, S. Fang, S. L. Tomarken, J. Y. Luo, J. D. Sanchez-Yamagishi, K. Watanabe, T. Taniguchi, E. Kaxiras, R. C. Ashoori, and P. Jarillo-Herrero. *Nature* **556**, 80-84 (2018).
- [27] C. R. Dean, L. Wang, P. Maher, C. Forsythe, F. Ghahari, Y. Gao, J. Katoch, M. Ishigami, P. Moon, M. Koshino, T. Taniguchi, K. Watanabe, K. L. Shepard, J. Hone, and P. Kim *Nature* **497**, 598–602 (2013).

- [28] B. Hunt, J. D. Sanchez-Yamagishi, A. F. Young, M. Yankowitz, B. J. LeRoy, K. Watanabe, T. Taniguchi, P. Moon, M. Koshino, P. Jarillo-Herrero, and R. C. Ashoori. *Science* **6139**, 1427–1430 (2013).
- [29] Y. Cao, V. Fatemi, S. Fang, K. Watanabe, T. Taniguchi, E. Kaxiras, and P. Jarillo-Herrero. *Nature* **556**, 43–50 (2018).
- [30] D. L. Cortie, G. L. Causer, K. C. Rule, H. Fritzsche, W. Kreuzpaintner, F. Klose *Adv. Funct. Mater.*, **30**, 1901414 (2020).
- [31] C. Gong, L. Li, Z. Li, H. Ji, A. Stern, Y. Xia, T. Cao, W. Bao, C. Wang, Y. Wang, Z. Q. Qiu, R. J. Cava, S. G. Louie, J. Xia, and X. Zhang *Nature* **546**, 265–269 (2017).
- [32] B. Huang, G. Clark, E. N. Moratalla, D. R. Klein, R. Cheng, K. L. Seyler, D. Zhong, E. Schmidgall, Michael A. McGuire, D. H. Cobden, W. Yao, Di Xiao, P. J.-Herrero , and X. Xu *Nature* **546**, 270–273 (2017).
- [33] R. Peierls *Proc. Camb. Philos. Soc.* **32**, 477-481 (1936).
- [34] W. Lenz *Phys. Z.* **21**, 613-15 (1920).
- [35] E. Ising *Z. Phys.* **31**, 353-58 (1925).
- [36] L. Onsager *Phys. Rev.* **65**, 117-149 (1944).
- [37] V.L. Berezinskii *Sov. Phys. JETP-USSR* **32**, 493-500 (1971).
- [38] J. M. Kosterlitz, and D. J. Thouless *J. Phys. C.* **6**, 1181–1203 (1973).
- [39] W. Heisenberg *Z. Phys.* **49**, 619–636 (1928).
- [40] N.D. Mermin, and H. Wagner *Phys. Rev. Lett.* **17**, 1133–1136 (1966).
- [41] P.C. Hohenberg *Phys. Rev.* **158**, 383–3863 (1967).
- [42] T.P. Kaloni *J. Phys. Chem. C* **118**, 25200–25208 (2014).
- [43] F. Ersan, H. Arkin, and E. Aktürk, *RSC Adv.* **7**, 937815–37822 (2017).
- [44] Y. Mao, G. Guo, J. Yuan, and J. Zhong *Appl. Surf. Sci.* **464**, 236–242 (2019).
- [45] Y. Miao, Y. Huang, Q. Fang, Z. Yang, K. Xu, F. Ma ,and P. K. Chu *J. Mat. Sci.* **51**, 9514–9525 (2016).
- [46] J. L. Lado and J. Fernández-Rossier *2D Materials* **4**, 035002 (2017).

- [47] J. Seo, D. Y. Kim, E. S. An, K. Kim, G. Y. Kim, S. Y. Hwang, D. W. Kim, B. G. Jang, H. Kim, G. Eom, S. Y. Seo, R. Stania, M. Muntwiler, J. Lee, K. Watanabe, T. Taniguchi, Y. J. Jo, J. Lee, B. I. Min, M. H. Jo, H. W. Yeom, S. Y. Choi, J. H. Shim, and J. S. Kim, *Science Adv.* **6**, eaay8912 (2020).
- [48] H. L. Zhuang, P. R. C. Kent, R. G. Hennig, *Phys. Rev. B* **93**, 134407 (2016)
- [49] A. F. May, D. Ovchinnikov, Q. Zheng, R. Hermann, S. Calder, B. Huang, Z. Fei, Y. Liu, X. Xu, and M. A. McGuire *ACS Nano* **13**, 4436-42 (2019).
- [50] H.-J. Deiseroth, K. Aleksandrov, C. Reiner, L. Kienle, and R. K. Kremer, *Eur. J. Inorg. Chem.* **2006**, 1561(2006).
- [51] B. Chen, J. Yang, H. Wang, M. Imai, H. Ohta, C. Michioka, K. Yoshimura, and M. Fang, *J. Phys. Soc. Japan* **82**, 124711 (2013).
- [52] Y. Deng, Y. Yu, Y. Song, J. Zhang, N. Z. Wang, Z. Sun, Y. Yi, Y. Z. Wu, S. Wu, J. Zhu, J. Wang, X. H. Chen, Y. Zhang, *Nature* **563**, 94-99 (2018)
- [53] Q. Li, M. Yang, C. Gong, R. V. Chopdekar, A. T. N'Diaye, J. Turner, G. Chen, A. Scholl, P. Shafer, E. Arenholz, A. K. Schmid, S. Wang, K. Liu, N. Gao, A. S. Admasu, S. W. Cheong, C. Hwang, J. Li, F. Wang, X. Zhang, Z. Qiu, *Nano Lett.* **18**, 5974 (2018)
- [54] Z. Wang, D. Sapkota, T. Taniguchi, K. Watanabe, D. Mandrus, and A. F. Morpurgo, *Nano Lett.* **18**, 4303-4308 (2018)
- [55] S. Mondal, N. Khan, S. M. Mishra, B. Satpati, and P. Mandal *Phys. Rev. B* **93**, 156802 (2004)
- [56] S. Bera, S. K. Pradhan, Md S. Khan, R. Pal, B. Pal, Sk Kalimuddin, A. Bera, B. Das, A. N. Pal, M. Mondal *J. of Magnetism and Magnetic Mat.* **565**, 170257 (2023).
- [57] Y. Zhang, H. Lu, X. Zhu, S. Tan, W. Feng, Q. Liu, W. Zhang, Q. Chen, Y. Liu, X. Luo, D. Xie, L. Luo, Z. Zhang, X. Lai, *Sci. Adv.* **4**, eaao6791 (2018).
- [58] M. Zhao, B.-B. Chen, Y. Xi, Y. Zhao, H. Xu, H. Zhang, N. Cheng, H. Feng, J. Zhuang, F. Pan, X. Xu, W. Hao, W. Li, S. Zhou, S. X. Dou, Y. Du, *Nano Lett.* **21**, 6117-6123 (2021).
- [59] R. Meservey and P. M. Tedrow, *Phys. Rev. Lett.* **26**, 192 (1971)
- [60] P.D. Johnson, *Rep. Prog. Phys.* **60**, 1217 (1997)
- [61] S. Phark D. Sander *Nano Convergence* **4**, 8 (2017).

- [62] I. I. Mazin, A. A. Golubov and B. Nadgorny *J. Appl. Phys.* **89**, 7576 (2001).
- [63] Yu. G. Naidyuk and I. K. Yanson, Point contact spectroscopy *Springer* (2005).
- [64] Yu. G. Naidyuk, I. K. Yanson, A. A. Lysykh, and O. I. Shklyarevskii, *Sov. Phys. Solid State* **22** 2145(1980).
- [65] A.G.M Jansen, A.P. van Gelder and P. Wyder *J. Phys. C: Solid St. Phys* **13**, 6073 (1980).
- [66] Y. V. Sharvin *Zh. Eksp. Teor. Fiz.* **21**, 655 (1965).
- [67] I.K. Yanson *Sov. Phys. JETP* **39**, 506–513 (1974).
- [68] A.M. Duif, A.G.M. Jansen, and P. Wyder *J. Phys.: Condens. Matter* **1**, 3157–3189 (1989).
- [69] G. Wexler *Proc. Phys. Soc. London* **89**, 927 (1966).
- [70] A.F. Andreev, *Sov. Phys. JETP* **19**, 1228 (1964).
- [71] G. E. Blonder, M. Tinkham, and T. M. Klapwijk, *Phys. Rev. B* **25**, 4515 (1982).
- [72] M. Tinkham,, Introduction to Superconductivity *McGrawhill* (1996).
- [73] P. Raychaudhuri, D. J. Nagar, G. Sheet, S. Ramakrishnan, H. Takeya *Phys. Rev. Lett.* **282**, 85 (1998).
- [74] Jian Wei , Goutam Sheet, and Venkat Chandrasekhar *Appl. Phys. Lett.* **97**, 062507 (2010).
- [75] R. J. Soulen Jr., M. S. Osofsky, B. Nadgorny, T. Ambrose, P. Broussard and S. F. Cheng, *J. Appl. Phys.* **85**, 4589 (1999).
- [76] S. Howlader, S. Saha, R. Kumar, V. Nagpal, S. Patnaik, T. Das, G. Sheet, *Phys. Rev. B* **102**, 104434 (2020).
- [77] S. Kamboj, S. Das, A. Sirohi, R. R. Chowdhury, S. Gayen, V. K. Maurya, S. Patnaik, and G. Sheet, *J. Phys.: Condens. Matter* **30**, 355001 (2018).
- [78] L. Aggarwal, S. Gayen, S. Das, R. Kumar, V. Su, C. Felser, C. Shekhar, and G. Sheet, *Nat. Commun.* **8**, 13974 (2016).
- [79] A. Sirohi, C. K. Singh, G. S. Thakur, P. Saha, S. Gayen, A. Gaurav, S. Jyotsna, Z. Haque, L. C. Gupta, M. Kabir, A. K. Ganguli, and G. Sheet, *App. Phys. Lett.* **108**, 242411 (2016).

- [80] P. Coleman *arxiv:cond-mat* 0612006v3 (2007).
- [81] P. W. Anderson *Phys. Rev.* **124**, 41 (1961).
- [82] J. Friedel *J. Phys. Radium* **19**, 573 (1958).
- [83] W.J. de Haas, J. de Boer, G.J. van den Berg *Physica* **1**, 1115-1124 (1934).
- [84] J. Kondo *Progress of Theoretical Physics* **32**, 37– 49 (1964).
- [85] L. Kouwenhoven and L. Glazman. *Physics World* **14**, 33–38 (2001).
- [86] M. Maltseva, M. Dzero, and P. Coleman, *Phys. Rev. Lett.* **103**, 206402 (2009).
- [87] U. Fano, *Phys. Rev.* **124**, 1866 (1961).
- [88] W. K. Park, J. L. Sarrao, J. D. Thompson, L. H. Greene, *Phys. Rev. Lett.* **100**, 177001 (2008).
- [89] M. Fogelström, W. K. Park, L. H. Greene, G. Goll, M. J. Graf, *Phys. Rev. B* **82**, 014527 (2010).
- [90] W. K. Park, P. H. Tobash, F. Ronning, E. D. Bauer, J. L. Sarrao, J. D. Thompson, L. H. Greene, *Phys. Rev. Lett.* **108**, 246403 (2012).
- [91] Y.-F. Yang, *Phys. Rev. B* **79**, 241107(R) (2009).
- [92] Y. De Wilde, J. Heil, A. G. M. Jansen, P. Wyder, R. Deltour, W. Assmus, A. Menovsky, W. Sun, and L. Taillefer *Phys. Rev. Lett.* **72**, 2278 (1994).
- [93] A. Nowack, A. Heinz, F. Oster, D. Wohlleben, G. Güntherodt, Z. Fisk, and A. Menovsky, *Phys. Rev. B* **36**, 2436(R) (1987).
- [94] L. Jiao, S. Howard, S. Ran, Z. Wang, J. O. Rodriguez, M. Sigrist, Z. Wang, N. P. Butch, V. Madhavan, *Nature* **579**, 523–527 (2020).
- [95] N. N. Bogoliubov *J. Exptl. Theoret. Phys(U.S.S.R)* **34**, 58 (1958).
- [96] J. Bardeen, L. N. Cooper, and J. R. Schrieffer, *Phys. Rev.* **108**, 1175 (1957).
- [97] X.-L. Qi and S.-C. Zhang *Rev. Mod. Phys.* **83**, 1057 (2011).
- [98] Y. Tanaka, M. Sato, and N. Nagaosa *J. Phys. Soc. Jpn.* **81**,011013 (2012)
- [99] B. A. Bernevig and T. L. Hughes *Princeton University Press, Princeton* (2013),
- [100] M. Z. Hasan, and C. L. Kane, *Rev. Mod. Phys.* **82**, 3045 (2010).

- [101] Y. Ando, and M. Sato, *Rep. Prog. Phys.* **80**, 076501 (2017).
- [102] J. Alicea, *Rep. Prog. Phys.* **75**, 076501 (2012).
- [103] C. W. J. Beenakker, *Annu. Rev. Con. Mat. Phys.* **4**, 113 (2013).
- [104] R. Aguado *La Rivista del Nuovo Cimento* **40**, 523 (2017).
- [105] A. Kitaev, *Annals of Physics* **303**, 2 (2003).
- [106] S. Das Sarma, M. Freedman, and C. Nayak, *Physics Today* **59**, 32 (2006).
- [107] C. Nayak, S. H. Simon, A. Stern, M. Freedman, and S. Das Sarma, *Rev. Mod. Phys.* **80**, 1083 (2008).
- [108] M. Leijnse, and K. Flensberg, *Semicond. Sci. Technol.* **27**, 124003 (2012).
- [109] T.D. Stanescu, and S. Tewari, *J. Phys. Condens. Matter* **25**, 233201 (2013).
- [110] S. R. Elliott, and M. Franz, *Rev. Mod. Phys.* **87**, 137 (2015).
- [111] S. Das Sarma, M. Freedman, and C. Nayak, *Npj Quantum Information* **1**, 15001 (2015).
- [112] A. Kitaev, *Phys. Usp.* **44**, 131 (2001).
- [113] R. M. Lutchyn, J. D. Sau, and S. Das Sarma, *Phys. Rev. Lett.* **105**, 077001 (2010).
- [114] Y. Oreg, G. Refael and F. von Oppen, *Phys. Rev. Lett.* **105**, 177002 (2010).
- [115] V. Mourik, K. Zuo, S. M. Frolov, S. R. Plissard, E. P. A. M. Bakkers and L. P. Kouwenhoven, *Science* **336**, 1003 (2012).
- [116] M. T. Deng, C. L. Yu, G. Y. Huang, M. Larsson, P. Caroff, and H. Q. Xu, *Nano Lett.* **12**, 6414 (2012).
- [117] L. P. Rokhinson, X. Liu, and J. K. Furdyna, *Nat. Phys.* **8**, 795 (2012).
- [118] A. Das, Y. Ronen, Y. Most, Y. Oreg, M. Heiblum and H. Shtrikman *Nat. Phys.* **8**, 887 (2012).
- [119] A. D. K. Finck, D. J. Van Harlingen, P. K. Mohseni, K. Jung, and X. Li, *Phys. Rev. Lett.* **110**, 126406 (2013).
- [120] H. O. H. Churchill, V. Fatemi, K. Grove-Rasmussen, M. T. Deng, P. Caroff, H. Q. Xu, and C. M. Marcus, *Phys. Rev. B* **87**, 241401 (2013).

- [121] W. Chang, S. M. Albrecht, T. S. Jespersen, F. Kuemmeth, P. Krogstrup, J. Nygrd and C. M. Marcus, *Nat. Nanotechnol.* **10**, 232 (2015).
- [122] J. J. He , J. Wu, T.-P. Choy, X.-J. Liu, Y. Tanaka & K. T. Law *Nat. Comm.* **5**, 3232 (2014).
- [123] O. A. Awoga, J. Cayao, and A. M. Black-Schaffer *Phys. Rev. Lett.* **123**, 117001 (2019).
- [124] J. Cayao, E. Prada, P. San-Jose, and R. Aguado *Phys. Rev. B.* **91**, 024514 (2015).
- [125] C.-X. Liu, J. D. Sau, T. D. Stanescu, and S. Das Sarma, *Phys. Rev. B* **96**, 075161 (2017).
- [126] S. Cho, R. Zhong, J. A. Schneeloch, G. Gu, and N. Mason *Sci. Rep.* **6**, 21767 (2016).
- [127] D. I. Pikulin, J. P. Dahlhaus, M. Wimmer, H. Schomerus and C.W.J Beenakker, *New J. Phys.* **14**, 125011 (2012).
- [128] D. Rana and G. Sheet, *J. Appl. Phys.* **131**, 084301 (2022).

Experimental Techniques

To extensively study the electronic and magnetic properties of the vdW ferromagnets, we have used three low-temperature techniques namely point contact spectroscopy (PCS), scanning tunneling microscopy/ spectroscopy (STM/S), and magnetic force microscopy (MFM). These techniques are briefly discussed below:

2.1 PCS experimental setup

The fundamentals of PCS have been discussed in Section (1.3) of this thesis. Here, we discuss different methods that can be adopted to form a point contact junction, details of the home-built PCS probe along with the data acquisition technique used for obtaining the results presented in this thesis.

2.1.1 Fabrication of point contacts

There are a number of techniques that can be employed to form a point contact junction between two metal electrodes. These are the needle-anvil method [1], soft point contact [2], shear method [3], lithographic method [4], and break junctions [5]. For our PCS measurements, we employed the needle-anvil method. In this method, a metallic tip sharpened electrochemically or mechanically and a freshly cleaved/polished sample are brought physically in contact either using a step-positioner or a differential screw arrangement, till ohmic contact forms. Given the crucial role of the interface in point contact spectroscopy (PCS) experiments, special care must be taken during the preparation of both the tip and sample surfaces. We first scratched and then sharpened the Niobium wire, used as a tip for our measurements, by mechanically cutting it at an angle. The single crystals of both the ferromagnets were cleaved using scotch tape just before cryogenic measurements. However, it is important to note that the presence of an oxide layer at the interface is still possible. To ensure the ballistic nature of the contact, certain steps are taken. Firstly, the oxide layer at

the interface is punctured by controlling the pressure on the tip, creating small constrictions that allow current flow. Subsequently, a ballistic contact is achieved by slightly retracting the tip to increase the contact resistance and, consequently, decreasing the contact size. In some cases, applying high-voltage electrical pulses at the interface can also assist in altering the contact resistance by eliminating existing micro-constrictions and forming new ones. For each formed contact, we record the differential conductance (dI/dV) as a function of the applied bias (V). Based on the characteristics of the conductance, we can identify the type of contact that has been established. The needle-anvil technique presents several advantages. Firstly, it is non-destructive, allowing for multiple measurements on the same samples. Secondly, the resistance of the contact can be controlled by adjusting the pressure applied by the tip. However, when dealing with very small samples, such as single crystals, the procedure becomes significantly challenging. In such cases, the "soft" point contact technique emerges as a more viable option.

The formation of soft point contact junctions involves delicately placing a droplet of silver paste or a small In flake ($\approx 50 \mu\text{m}$ in diameter) onto the pristine surface of the sample. The counter electrode, connected to current and voltage leads through a thin Au wire, is positioned above the sample. Despite the relatively larger "footprint" of the counter-electrode, particularly noticeable with Ag paste, compared to the electronic mean free path, these contacts frequently provide spectroscopic information. This suggests that, on a microscopic scale, the actual electrical contact occurs through parallel nanometric channels that connect the sample surface with the In flake or individual grains in the Ag paste. The contacts formed usually lie in the ballistic regime of transport. The schematic of both methods is shown in Figure 2.1.

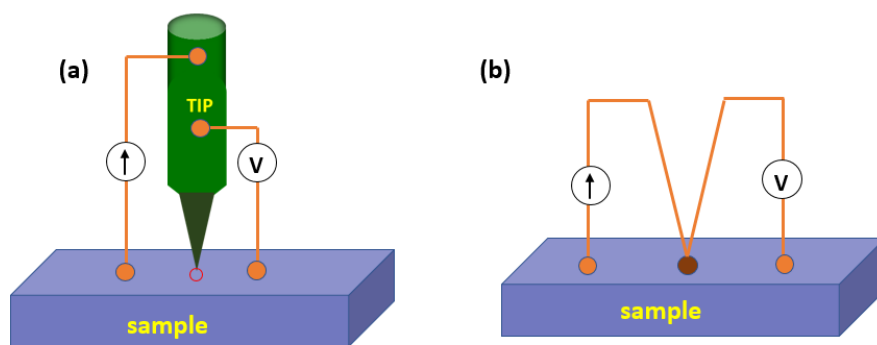


Figure 2.1: Schematic illustrating (a) needle-anvil and (b) soft point contact method.

2.1.2 PCS probe and data acquisition

A home-built PCS probe consisting of a long stainless steel tube with a probe head positioned at the end was used for measurements. The probe head is equipped with a differential screw (100 threads per inch) arrangement, which can be operated using a shaft extending to the top of the cryostat. The tip is mounted in the copper tip holder positioned at the end of the differential screw such that rotation of the screw enables vertical movement of a tip-holder in relation to the sample being studied. The sample was mounted on the small removable disc-shaped copper disk mounted on the bigger copper disk. A Cernox thermometer and a 33Ω (1 Watt) resistor, mounted on the bigger Copper disk, has been used to measure and regulate the temperature of the sample respectively. The PCS probe head has been shown in Figure 2.2. The electrical connections of the probe were done using twisted pairs of 0.25 mm dia Copper wires. For conductance measurements, two contact leads on the tip and sample respectively were made with silver epoxy (Epotek-2component) using copper wires. The measurements were performed inside a variable temperature American Magnetics cryostat working down to 1.4 K which is also equipped with a 3-axis superconducting vector magnet (6T-1T-1T).

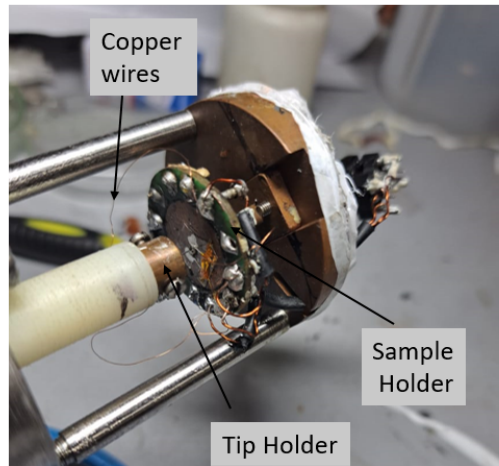


Figure 2.2: PCS probe head.

After the point contact between the tip and the sample had been established, a lock-in-based modulation technique was used to acquire the point contact spectrum (dI/dV vs V). A schematic of the setup is shown in Figure 2.3. In this technique, a sweeping dc current (I_{dc}) is coupled to fixed low-frequency (in the range of a few Hertz to a few kilo Hertz) ac current ($I_{ac}\cos(\omega t)$) such that $I_{dc} \gg I_{ac}$. The output voltage under this approximation can

be Taylor expanded as

$$V(I_{dc} + I_{ac}\cos(\omega t)) = V(I_{dc}) + \left(\frac{dV}{dI}\right)_{I=I_{dc}} I_{ac}\cos(\omega t) + \frac{1}{2} \left(\frac{d^2V}{dI^2}\right)_{I=I_{dc}} (I_{ac}\cos(\omega t))^2 + \dots \quad (2.1)$$

For our measurements, a dc current source (Kethley 6220) was used to supply dc current, and a lock-in amplifier (Stanford Research System 830) was used to provide ac current by using a voltage-to-current converter. The dc voltage drop across the point contact was then recorded using a digital multimeter (Kethley 2000). The ac voltage output of the lock-in amplifier, for signal locked at the first harmonic, is proportional to differential resistance dV/dI from which differential conductance was calculated. The code for data acquisition was designed in Labview.

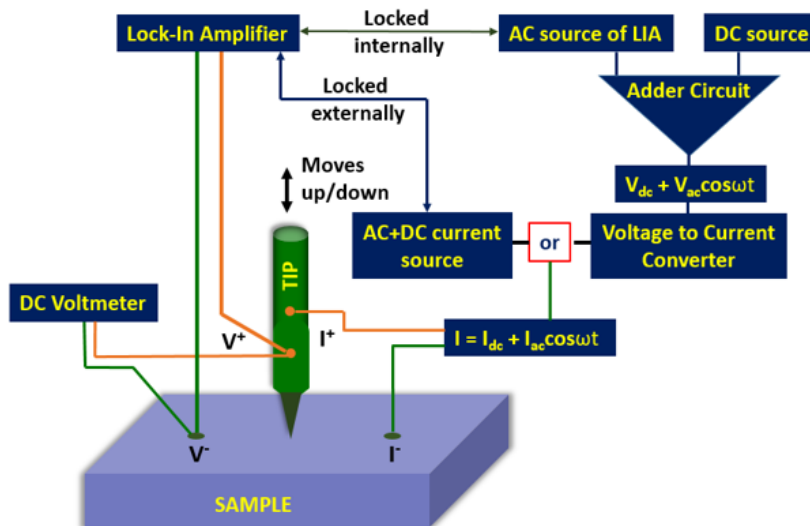


Figure 2.3: Schematic illustrating the point contact spectroscopy data acquisition setup.

2.2 Scanning Tunneling Microscopy

2.2.1 Basic Principles

Tunneling is a phenomenon in quantum mechanics where a particle can penetrate through a potential barrier even if its energy is less than the height of the barrier. The first demonstration of electron tunneling was given by Leo Esaki in semiconductors [6] and by Ivar Giaever in superconductors [7] respectively. Classically this phenomenon is forbidden. However, quantum mechanically, a particle can exhibit wave-like nature and the wave function can

exponentially decay into the barrier region leading to a non-zero probability of the particle passing through the barrier. Therefore, when the two metallic surfaces are brought close to within a few nanometers, the tunneling current flows when a potential difference between the two is established (Figure 2.4). The tunneling current depends exponentially on the width of the barrier between two electrodes (d) and can be expressed as:

$$I \propto e^{-2\kappa d} \quad (2.2)$$

where the decay constant $\kappa = \frac{\sqrt{2m\phi}}{\hbar} \approx 0.513\sqrt{\phi(eV)}\text{\AA}^{-1}$; m is the mass of the electron and ϕ gives the height of the potential barrier which is basically equal to the averaged work function ($\phi = \frac{\phi_1 + \phi_2}{2}$) of the two metals. Since most of the metals have their work function lying in the range 4 eV-6 eV, the work function of both metals can be approximated to be equal. Approximating $\phi = 5\text{eV}$ and $\kappa = 1\text{\AA}^{-1}$ leads to the decay of tunneling current by a factor of e^{-2} for every 1 \AA increase in d .

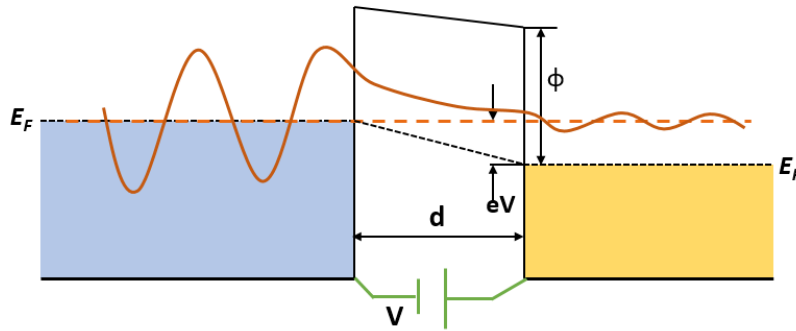


Figure 2.4: Schematic depicting two metal electrodes separated by a barrier of width d and height ϕ . Quantum tunneling of electrons between the two metals happens when a potential difference is established.

Based on this phenomenon, Binnig and Rohrer in 1982 [8], designed the first scanning tunneling microscope (STM) and was later awarded Nobel Prize for their invention. STM is a powerful probe to investigate the electronic properties of conducting materials on an atomic scale. A sharp metallic tip (W or Pt-Ir tip) and the conducting sample are positioned a few angstroms apart using an assembly of piezo-walkers. The vacuum or oxide plays the role of a potential barrier between the tip and the sample. The tunneling current flows when a potential difference of eV between the two is established and can be measured a function of (x,y) location and applied bias. Following Bardeen's approach [9], the resultant elastic tunneling current between the tip and the sample can be derived using Fermi's Golden rule [10], based on the time-dependent perturbation theory. Applying a negative bias V to the sample causes the Fermi electrons within the sample to be energetically elevated compared to the electrons in the tip. Consequently, electrons from the occupied states of the sample

can tunnel into the unoccupied states of the tip (Figure 2.5). The tunneling current from sample to tip in the presence of a bias voltage can be expressed as

$$I_{s \rightarrow t} = -2e \frac{2\pi}{\hbar} |M|^2 (N_s(\epsilon) f(\epsilon)) (N_t(\epsilon + eV) [1 - f(\epsilon + eV)]) d\epsilon \quad (2.3)$$

The factor of 2 comes from the spin of the electron, $|M|^2$ is the tunneling matrix element, N_t and N_s represent the density of states of tip and sample respectively. $f(\epsilon) = \frac{1}{\exp(\frac{\epsilon}{k_B T}) + 1}$ is the Fermi distribution function, Fermi energy being set to zero. $N_s(\epsilon) f(\epsilon)$ corresponds to the number of filled sample states for tunneling from and $N_t(\epsilon + eV) [1 - f(\epsilon + eV)]$ are the number of empty tip states available for tunneling into. The tunneling current from tip to sample can be expressed as:

$$I_{t \rightarrow s} = -2e \frac{2\pi}{\hbar} |M|^2 (N_t(\epsilon + eV) f(\epsilon + eV)) \cdot (N_s(\epsilon) [1 - f(\epsilon)]) d\epsilon \quad (2.4)$$

The net tunneling current, I , is given by the difference between equations (2.3) and (2.4),

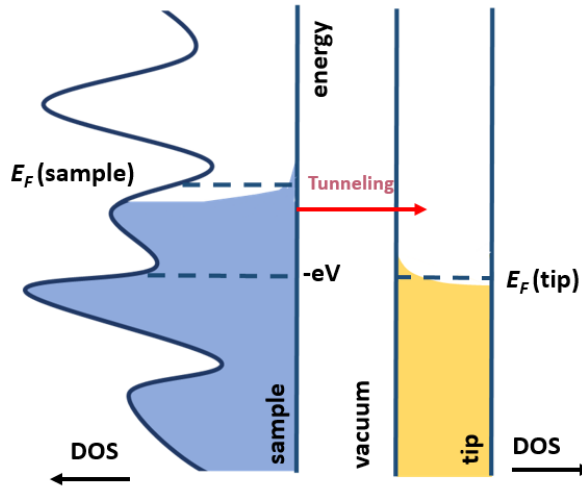


Figure 2.5: Schematic of tunneling from filled sample states to empty tip states when the sample is negatively biased.

$$I = \frac{4\pi e}{\hbar} \int_{-\infty}^{\infty} |M|^2 N_s(\epsilon) N_t(\epsilon + eV) \cdot (f(\epsilon) [1 - f(\epsilon + eV)] - [1 - f(\epsilon)] f(\epsilon + eV)) d\epsilon \quad (2.5)$$

Since the energy levels of the tip are shifted with respect to the sample by eV , it is sufficient to focus the range of interest to $-eV < \epsilon < 0$. At significantly low temperatures the Fermi distribution function shows a sharp cutoff at the Fermi energy. Therefore, at low

temperatures, the net tunneling current I is

$$I \approx \frac{4\pi e}{\hbar} \int_{-eV}^0 |M|^2 N_s(\varepsilon) N_t(\varepsilon + eV) d\varepsilon \quad (2.6)$$

The STM tips are commonly made of tungsten (W) and platinum-iridium ($Pt - Ir$) alloy, having a flat density of states at the Fermi level. In addition, the tunneling matrix element can be considered constant in energy. Under these approximations, the tunneling current can be expressed as

$$I \approx \frac{4\pi e}{\hbar} |M|^2 N_t(0) \int_{-eV}^0 N_s(\varepsilon) d\varepsilon \quad (2.7)$$

The tunneling matrix element $|M|^2$ was calculated by Tersoff and Hamann (TH) using the WKB approximation [11]. Under this approximation, the vacuum barrier between the tip and the sample is assumed to be a square barrier. The tunneling matrix element can be written as:

$$|M|^2 = e^{-2\frac{d}{\hbar}\sqrt{2m\phi}} \quad (2.8)$$

where d is the width of the barrier between tip and sample, ϕ is the height of the barrier which depends on the (averaged) work function of the tip and sample. By combining equation (2.7) with (2.8), the tunneling current becomes:

$$I \approx \frac{4\pi e}{\hbar} e^{-2\frac{d}{\hbar}\sqrt{2m\phi}} N_t(0) \int_{-eV}^0 N_s(\varepsilon) d\varepsilon \quad (2.9)$$

Therefore, the tunneling current is proportional to the integral of the density of states of the sample.

2.2.2 Modes of operation

Topography

STM has the exceptional ability to generate real-space images at the atomic level of resolution. To map the topography, the tunneling current between the tip and the sample is kept constant at the set value, as the tip is rastered at fixed bias across the surface in the $x - y$ plane. The height of the tip in the z direction is adjusted using a feedback loop to maintain the constant current, and this height information is used to generate a contour of the surface topography. This mode is generally called a constant current mode. This method is suitable for imaging any corrugated/irregular surface without altering or damaging the tip. However, the finite response time of the feedback loop imposes an upper limit on the maximum scanning speed. A typical schematic of the STM is shown in Figure 2.6 (a) and an example of a topograph, obtained using constant current mode is shown in Figure 2.6 (b). The constant current mode has been employed for all our topographic measurements using STM.

Another mode for obtaining topography using STM is the constant height mode. In this imaging method, the tip is positioned at a fixed distance above the sample, and the tunneling current between the tip and the sample is measured as the tip is scanned across the surface. Variations in the tunneling current indicate changes in the height of the sample surface, proportional to the topography of the surface. However, if there are any surface irregularities or unexpected changes, the tip can come into contact with the surface, potentially causing damage to both the tip and the sample.

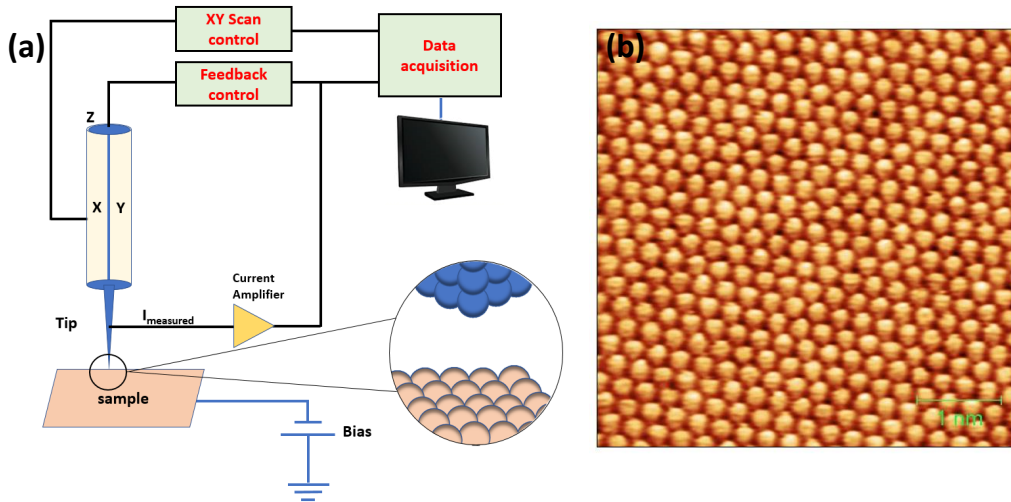


Figure 2.6: (a) A typical schematic of STM illustrating a sharp metallic tip (W or Pt-Ir tip) and the conducting sample positioned a few Angstroms apart using an assembly of piezo-walkers (b) Atomically resolved topograph of 5 nm × 5 nm area of turbostratic graphene for $V_b= 400$ mV and $I_t=450$ pA.

Scanning Tunneling Spectroscopy(STS)

STS is another mode of STM utilizing which the density of states of the sample can be obtained. Using this mode, it is possible to get information about the superconducting energy gap, Dirac point in topological insulators and semi-metals, Majorana fermions in topological superconductors, Fano resonance in Heavy fermionic systems, etc. It is evident from equation (2.9) that the tunneling current is proportional to the integral of the density of states (DOS) of the sample. Therefore, it is possible to measure the DOS of the sample by performing the first-order derivative of the current with respect to the applied bias i.e. by measuring the tunneling conductance such that

$$G(V) = \frac{dI}{dV} \propto N_s(eV) \quad (2.10)$$

For measuring the tunneling conductance, the feedback loop is turned off and the tip

position is fixed at the desired point on the sample. The bias voltage is swept and the current response as the function of applied bias is measured. To note, the process of obtaining the conductance (dI/dV) by numerically differentiating the I vs. V curve can be highly susceptible to noise. To overcome this challenge, a commonly employed method involves utilizing a lock-in amplifier-based modulation technique to measure dI/dV . This technique incorporates a small modulation (dV) of the bias voltage (typically a few millivolts) added to V , allowing the measurement of the resulting change in tunneling current (dI), which in turn provides the value of dI/dV . This technique has been employed for all our STS measurements. An example of the dI/dV spectrum obtained in the case of the type-II superconductor and Kondo lattice system is shown in Figure 2.7.

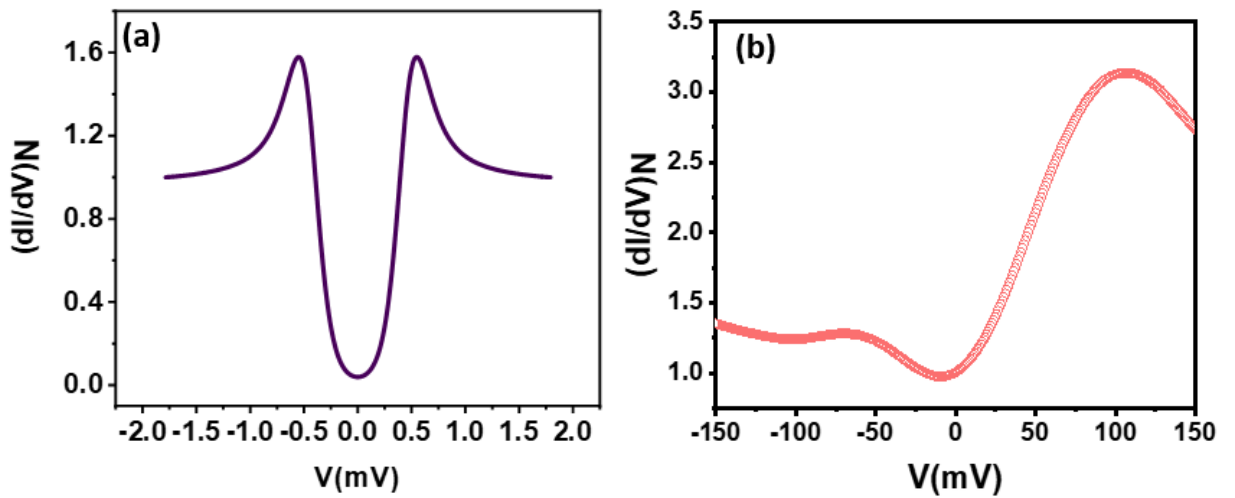


Figure 2.7: The density of states of (a) Pt-doped IrTe_2 , type-II superconductor, recorded at 330 mK. (b) a Kondo lattice ferromagnet Fe_4GeTe_2 recorded at 2K.

2.2.3 UHV-STM

The STM/S measurements presented in this thesis were performed using an ultra-high vacuum (UHV) UNISOKU USM-1300 STM. The STM is equipped with a He-3 cryostat and hence ultra-low temperature (ULT) down to 300mK can be achieved in the scanning stage. The liquid Helium dewar has a bottom-loaded 11 Tesla solenoidal superconducting magnet. Hence, it is possible to perform measurements under UHV and ULT conditions in the presence of high magnetic fields.

UHV subsystem

Since the presence of air molecules or other contaminants can interfere with the tunneling current and can effect the resolution of images, ultra-high vacuum conditions ($\sim 10^{-10}$ –

10^{-12} mbar) for STM measurements is required. The system has three stainless steel chambers: load lock, preparation, and exchange chamber. The chambers are separated from each other using VAT gate valves. The samples and tips are loaded from outside to the load lock chamber which is then pumped using an Edward nEXT-300 Turbomolecular pump connected to the chamber via a pneumatic valve. After the pressure of $\sim 10^{-9}$ mbar is reached in the load lock chamber, the samples are transferred from the load lock chamber to the preparation chamber using a horizontal magnetic manipulator. The UHV conditions in preparation, and exchange chambers are maintained using two Gamma vacuum ion pump reaching $10^{-10} - 10^{-11}$ mbar. The preparation chamber is equipped with a tip heating setup and additionally has the provision to clean the sample in-situ through Ar-based reverse sputtering or by heating the sample by passing current through it. In addition, it is equipped with two thermal evaporators (K-shell and W-shell), low energy electron diffraction (LEED), and reflection high energy electron diffraction (RHEED) setup. By using long horizontal magnetic manipulators, the processed tips and samples can be transferred from preparation to the exchange chamber. In the exchange chamber, the samples can be cleaved using an in-situ cleaver at low temperatures down to 77K. The sample and tip for measurements are transferred to the STM head using a long vertical magnetic manipulator.

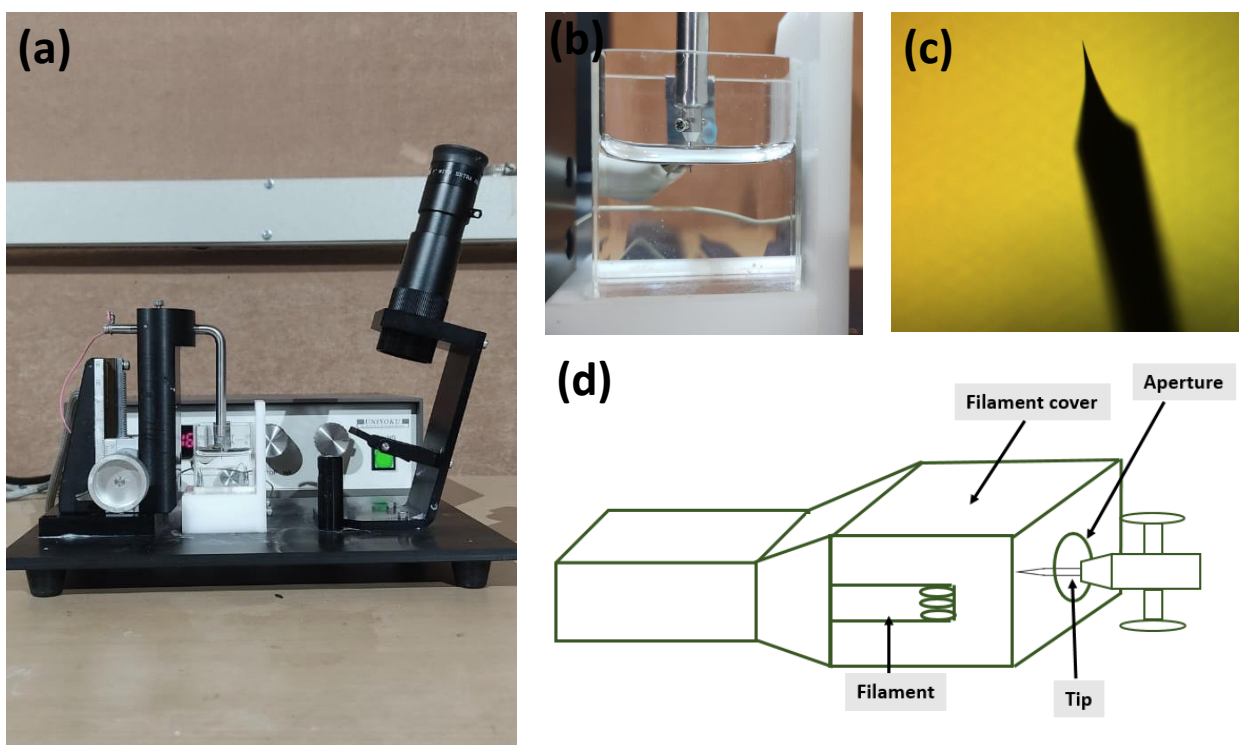


Figure 2.8: (a) Tip etching setup. (b) Tungsten tip immersed in the KOH solution (c) Image of W tip, prepared by electrochemical etching, under an optical microscope. (d) Schematic showing tip heating setup.

Tip preparation

The resolution of the STM image is significantly affected by the sharpness of the tip apex. The STM tips are generally made of conducting materials like tungsten (W) or platinum-iridium (Pt-Ir). Techniques like mechanical polishing and electrochemical etching are typically used for preparing STM tips. For our experiments, sharp W tips were prepared by the electrochemical etching method. A tungsten wire (0.25mm diameter, 1.5 cm in length) was scraped with sandpaper of grade P8000 before being cleaned with ethanol and distilled water. The tip etching setup is shown in Figure 2.8(a). A 1.2N potassium hydroxide (KOH) solution, acting as an electrolyte, was used to immerse a platinum ring (cathode) with tungsten wire (anode) in its center. A stopping current of 2 mA and a bias voltage of 10 V was supplied between the two electrodes. As soon as the output current attained a value below the stopping current, the etching process was automatically stopped. The electric voltage increases as it goes closer to the meniscus, which caused the submerged portion of the tungsten wire to begin to thin out. Finally, the submerged portion of the wire broke off after 20–25 minutes. After washing the tip with distilled water and ethanol, we halted the etching operation. Before transferring the tip to the load-lock chamber, the sharpness of the tip was checked under the optical microscope Figure 2.8 (c). The STM tips should be clean and free of any oxide layer as it can interfere with the tunneling current and affect the resolution of the images. Therefore, after the preparation, the STM tip was cleaned in the preparation chamber by electron bombardment using an electron beam heater EBT-100, before transferring it to the scanning unit. The schematic of the in-situ tip heat treatment setup is shown in Figure 2.8(d)

Cleaving mechanism

Since STM is a surface-sensitive technique, it is important to have a pristine sample surface free of any oxidation or surface contamination in order to achieve maximum resolution. The surface of the sample can be cleaned before measurements by Ar-sputtering, mechanical cleaving, or heating. The single crystals of Fe_3GeTe_2 and Fe_4GeTe_2 were cleaved, just before STM/S measurements, using an in-situ cleaver in ultra-high vacuum conditions and a cryogenic temperature of around 77K. A wire was fixed on the sample surface using silver epoxy before transferring the sample to the load-lock chamber. The sample along with the wire was then transferred to the exchange chamber, through the preparation chamber, where the sample temperature was first stabilized to 77 K using liquid nitrogen. After that using a manipulator the wire was hit, leaving us with a pristine sample surface. The sample was then transferred to the STM head for low-temperature measurements. Figure 2.9(a)-(b) shows the cleaving setup and the sample after cleaving.

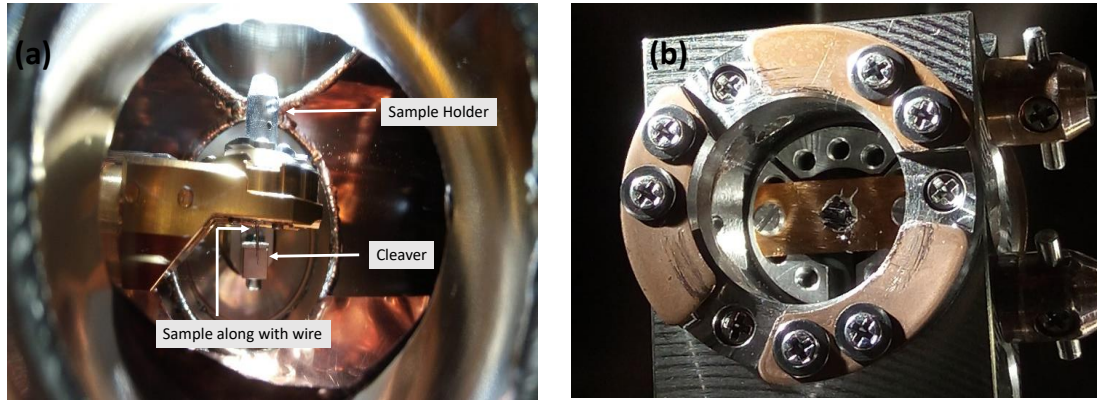


Figure 2.9: (a) In-situ cleaving setup. (b) Sample just after cleaving.

STM head and electronic unit

The tip is mounted at the end of the single tube-type piezo driver which controls its motion in the lateral (x,y) and vertical (z) directions during scanning. The tube is partitioned into quadrants using X (X+, X-), Y (Y+, Y-), and Z electrodes. Initially, the tip is driven towards the sample using the coarse and fine positioning unit in a slip-stick manner until a tunneling current is detected. Once the tunneling regime is reached, the tip can be directed in various directions by applying appropriate voltages to the electrodes of the scan piezo. The scanning tube piezo provides a maximum scanning area dimensions of $0.6\mu\text{m} \times 0.7\mu\text{m} \times 70\text{ nm}$ at Helium temperatures.

Before measurements, it is important to have effective noise isolation to counter the effect of common sources of noise: vibrational, acoustic, and electronic. Such noises can affect the stability of the tip-sample junction leading to distorted images or fluctuations in the tunneling current. To minimize the effect of vibrations, all three chambers of our STM hang on a vibration isolation table with pneumatic legs. A large concrete pit further surrounds the entire unit, isolated from the rest of the building using quartz sand and neoprene. To block electromagnetic radiation and acoustic noise from entering the measurement area, the system has been housed in a Faraday cage. To achieve internal vibration isolation, the STM head is equipped with coil springs. To mitigate ground loop noise, separate grounding pits for the data-acquisition electronics have been implemented.

Our scanning tunneling microscope (STM) is equipped with an RHK- R9 controller. For attaining high resolution, the R9 controller consists of multiple voltage sources ranging from -10 V to 10 V , lock-in amplifiers covering a frequency range of $0\text{-}100\text{ Hz}$, digital oscillators, digital-to-analog converters (DACs), high/low pass filters, and dual phase locked loops (PLLs). It is compatible with the IHDL icon-based program language for interface programming and provides diagnostic tools like a transient recorder, channel oscilloscope,

spectrum analyzer, and data logger. For current amplification and noise reduction in the feedback signal, we employ the Femto DLPCA-200 current amplifier. This amplifier can adjust its gain from 10^3 to 10^{11} V/A and features input noise as low as $4.3 \text{ fA}/\sqrt{\text{Hz}}$. It converts the measured tunneling current to voltage and amplifies it. Additionally, a high-voltage filter with a cut-off frequency of 530 kHz has been integrated to eliminate high-frequency noise in the input signal. To further enhance the amplification process, we utilize a second-stage voltage pre-amplifier called the R9 IVP preamp. The approach mechanism of the STM is controlled by the PMC100 from RHK technology, which is interconnected with the R9 controller. This allows for automated control of the approach mechanism through the interface program.

2.3 Magnetic force microscopy (MFM)

Magnetic force microscopy (MFM) is a powerful scanning probe technique with the ability to analyze and visualize localized magnetic characteristics of a given sample by measuring the magnetic force gradients [12, 13]. This technique has been widely used in the analysis of magnetic storage media and magnetic nanomaterials to map magnetic domains, walls, and vortices in superconductors. It is based on the principles of atomic force microscopy (AFM) [14] and utilizes a cantilever with a magnetic coating to map the z -component of the stray magnetic field emanating from the surface of the sample under study. The schematic illustrating the technique is shown in Figure 2.10. The interaction between the tip and sample can be either attractive or repulsive, depending on the orientation of the tip's magnetization and the stray field. The tip deflection as a consequence of this interaction can be measured using a photodetector.

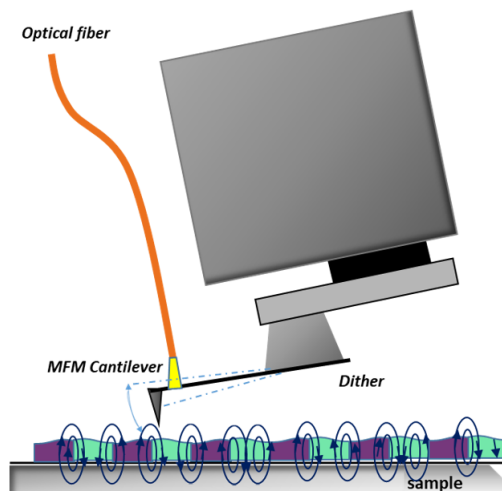


Figure 2.10: Schematic illustrating the interaction of MFM cantilever with the stray field of the sample.

Depending on the tip-sample distance the effect of a number of interaction forces comes into play, as depicted in Figure 2.11. Therefore, MFM images can contain both topographic as well as magnetic signals. To extract the magnetic signal, imaging is performed in the dual pass mode also known as the lift mode. In the single pass, the cantilever using a feedback loop maps the topography of the sample surface where the effect of van der Waal interactions dominates. In the dual pass mode, the tip is lifted to a certain height above the sample and performs imaging following the topographic contour at the set lift height. Since the magnetic forces are long-ranged as compared to the van der Waals forces, the effect of the topographic variations can be eliminated to obtain a pure magnetic signal in the dual pass mode.

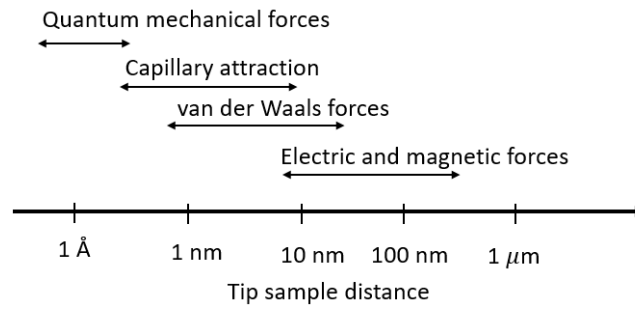


Figure 2.11: Range, as a function of tip-sample distance, over which the interaction forces dominate the MFM signal.

2.3.1 Modes of operation

There are two modes of operation in which magnetic force microscopy can be performed: Static mode and Dynamic mode. Dynamic mode can be further classified into the non-contact mode and the contact mode.

Static mode

In this mode, the force of interaction (either attractive or repulsive) between the tip and the sample surface is measured by detecting the vertical deflection in the cantilever's equilibrium position. The cantilever displacement can be calculated using Hooke's law

$$\Delta z = -\frac{F_{TS}}{k} \quad (2.10)$$

F_{TS} gives the force of interaction between the tip and the sample and k is the spring constant.

Dynamic mode

In this mode, the cantilever is made to oscillate at its resonant frequency by an actuator. The motion of the cantilever can be defined using the equation of motion of a harmonic oscillator:

$$m \frac{d^2z}{dt^2} + b \frac{dz}{dt} + k(z - z_0) = F_{ex}(t) + F_{TS}(z) \quad (2.11)$$

where m and k are the effective mass and spring constant of the cantilever, b is the damping coefficient, z is the displacement of the cantilever, and z_0 is the equilibrium position of the cantilever in the absence of any force. The cantilever is driven using an external oscillating force $F_{ext}(t) = F_0 \cos(\omega_0 t)$ and $F_{TS}(z)$ gives the z -component of the force between the cantilever and the sample. Approximating F_{TS} to be small, the Taylor expansion of equation (2.11) for $z = z_0$ gives:

$$m \frac{d^2z}{dt^2} + b \frac{dz}{dt} + k(z - z_0) = F_{ex}(t) + F_{TS}(z = z_0) + \left. \frac{dF_{TS}}{dz} \right|_{z=z_0} (z - z_0) \quad (2.12)$$

$$m \frac{d^2z}{dt^2} + b \frac{dz}{dt} + \left(k - \left. \frac{dF_{TS}}{dz} \right|_{z=z_0} \right) (z - z_0) = F_{ex}(t) + F_{TS}(z = z_0) \quad (2.13)$$

On defining, $k_{eff} = k - \left. \frac{dF_{TS}}{dz} \right|_{z=z_0}$, equation (2.13) can be rewritten as :

$$m \frac{d^2z}{dt^2} + b \frac{dz}{dt} + k_{eff}(z - z_0) = F_{ex}(t) + F_{TS}(z = z_0) + \left. \frac{dF_{TS}}{dz} \right|_{z=z_0} (z - z_0) \quad (2.14)$$

In the presence of a force gradient, the cantilever resonant frequency can be expressed as f'_o where

$$f'_o = \sqrt{\frac{k_{eff}}{m}} \quad (2.15)$$

where the right hand side can be Taylor expanded (in the limit $\left. \frac{dF_{TS}}{dz} \right|_{z=z_0} \ll k$). The shift in the cantilever frequency due to tip sample interaction, $\Delta f = f'_o - f_o$, can be expressed in terms of force gradient as

$$\frac{\Delta f}{f_o} = \frac{-1}{2k} \frac{\partial F_{TS}}{\partial z} \quad (2.16)$$

For attractive tip-sample interaction $\left. \frac{\partial F_{TS}}{\partial z} \right|_{z=z_0} > 0$, resulting in a negative shift in the resonance frequency. Repulsive tip-sample interaction $\left. \frac{\partial F_{TS}}{\partial z} \right|_{z=z_0} < 0$ results in the positive shift in the resonance frequency. To measure the force gradient, frequency/phase modulation [15] can be used.

2.3.2 LT-MFM

A low-temperature compatible magnetic force microscope (Attocube LT-MFM), working down to Helium temperatures, equipped with a single mode optical fiber-based interferometer was used for performing the ferromagnetic domain imaging in both the ferromagnets. The low temperatures were achieved using a liquid Helium-based cryostat working down to 1.4 K and equipped with a 3-axis superconducting vector magnet (6T-1T-1T). The schematic depicting the design of the setup is shown in Figure 2.12 (a). It consists of the measurement head, enclosed within a housing, attached to the lower end of the microspore stick. The image of the microscope head is shown in Figure 2.12 (b). The sample under study is placed on a stack of positioners and scanners. ANPxyz101 positioner allows for a coarse motion within a range of $5 \times 5 \times 5 \text{ mm}^3$ and ANSxyz100 scanner provides scanning dimensions of $30 \times 30 \times 15 \text{ }\mu\text{m}^3$ at a temperature of 4 K. The temperature sensor and heater are installed just below the sample holder to record and control the temperature of the sample. The cantilever assembly is residing, at the end of the optical fiber, just above the sample housing unit. The top end of the cantilever head is coated with a reflective material. The magnetic cantilever from Nanosensors (PPP-LM-MFMR), i.e. a Silicon cantilever with Aluminium coating, was used for our measurements. A high spatial resolution of $\approx 20\text{nm}$ can be achieved. The microscope is equipped with a laser diode of wavelength 1310 nm.

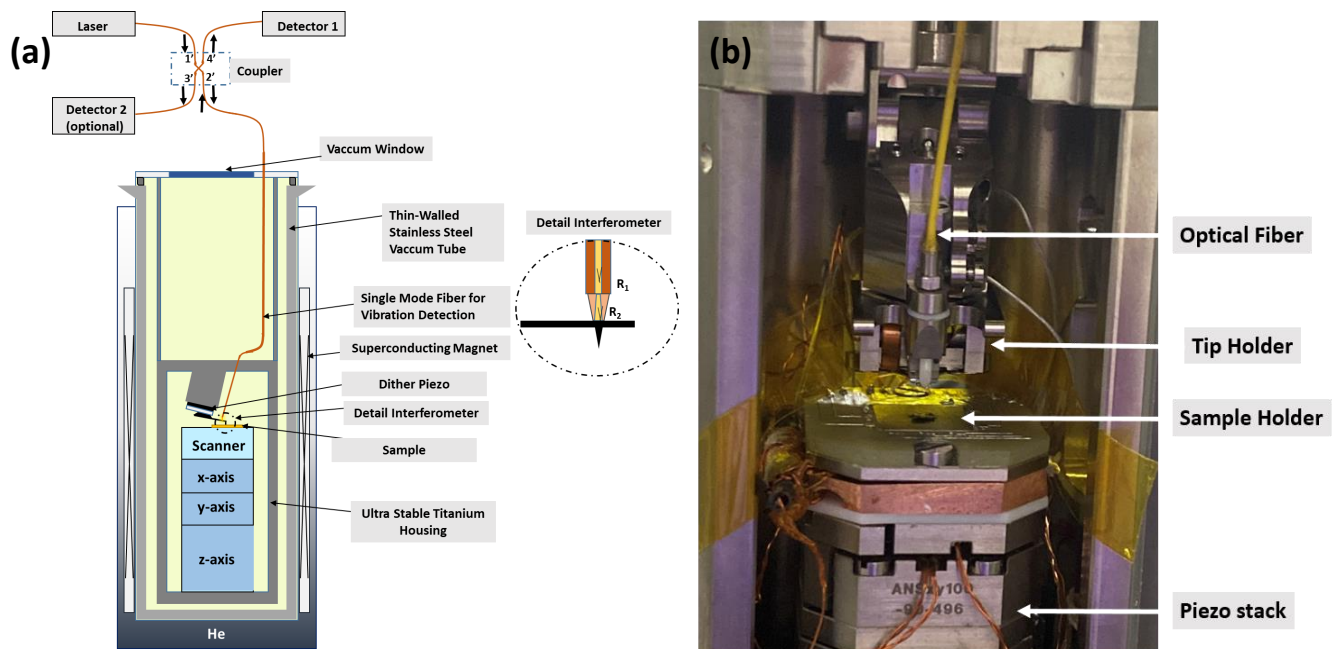


Figure 2.12: (a) Schematic illustrating the design of LT-MFM. The inset shows the optical cavity. (b) MFM microscope head.

The detection mechanism is explained as follows: The laser beam, incident from the

optical fiber, is reflected back from the detector once from the end face of the fiber ($R1$) and once from the back face of the cantilever ($R2$). The space between $R1$ and $R2$ acts as an optical cavity, similar to the concept observed in the Fabry-Perot or Michelson interferometer. The combination of these two reflected beams creates an interference pattern, which is then detected. The oscillations of the cantilever influence the length of the cavity, thereby affecting the intensity of the signal captured by the photo-detector. The interferometer achieves maximum sensitivity when the cantilever vibrates around the point of maximum slope in the interference signal, known as the working point. The working point is determined by applying a DC voltage offset to the dither piezo. Further, by applying an AC voltage to the dither piezo, the cantilever can be excited at its resonance frequency. Consequently, the AC signal detected at the resonance frequency, obtained from the photodetector, reflects the amplitude of oscillation exhibited by the cantilever. As the cantilever approaches the sample, the amplitude of this vibration rapidly decreases as the tip-sample distance diminishes. Therefore, physical contact between the tip and the sample is not necessarily established. At this stage, an oscillation amplitude known as the "set level" is defined, which corresponds to a specific force acting between the sample and the cantilever. The vibration amplitude of the cantilever is utilized as the input for a feedback loop, which adjusts the voltage on the z-scanner to maintain the cantilever oscillation at the set level (referred to as amplitude feedback). Alternatively, the amplitude and phase of the oscillation resonance can be kept constant (referred to as phase feedback). During the single pass, the output signal from the feedback loop (z-piezo voltage) is recorded to obtain topographic information. During the dual pass, the cantilever is lifted to the set lift height and follows the contours of the topography at the set lift height. The magnetic signal can be measured by either measuring the phase shift at a constant frequency or the frequency shift at a constant phase in a phase-locked mode. The dual pass phase image, taken at a lift height of 35nm, obtained on Fe_3GeTe_2 using the Attocube MFM is shown in Figure 2.13.

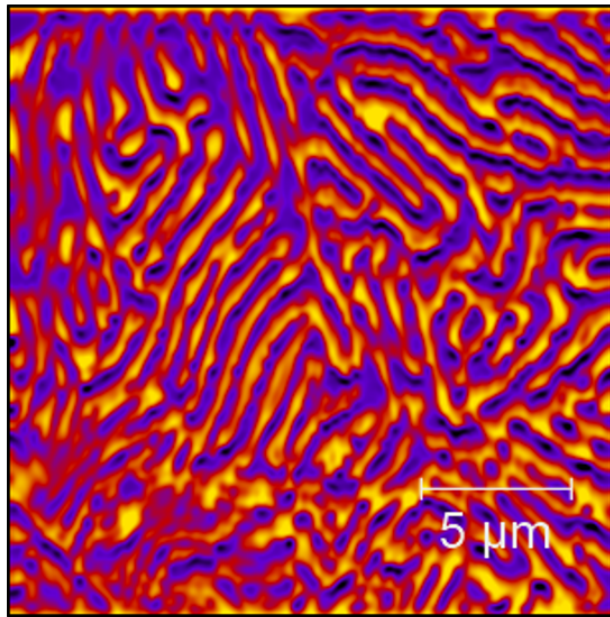


Figure 2.13: MFM dual pass phase image taken on the cleaved single crystal of Fe_3GeTe_2 using Attocube LT-MFM at 1.6 K. The magnetic filamentary domains are clearly visible. The contrast in the image corresponds to the regions of opposite magnetization.

Bibliography

- [1] A. G. M. Jansen, F. M. Mueller and P. Wyder, *Phys. Rev.* **16**, 1325 (1977).
- [2] D. Daghero, and R. S. Gonnelli, *Supercond. Sci. Technol.* **23**, 043001 (2010).
- [3] P. N. Chubov, I. K. Yanson, and A. I. Akimenko, *Sov. J. Low Temp. Phys* **8**, 32 (1982).
- [4] S. K. Ralls, A. R. Buhrman and C. R. Tiberio, *Appl. Phys. Lett.* **55**, 2459 (1989).
- [5] J. C. Muller, M. J. van Ruitenbeek and J. L. Jongh, *Physica C* **191**, 485 (1992).
- [6] L. Esaki, *Phys. Rev.* **109**, 603 (1958).
- [7] I. Giaever, *Phys. Rev. Lett.* **5**, 147 (1960).
- [8] G. Binnig and H. Rohrer, *Helv. Phys. Acta* **55**, 726 (1982).
- [9] J. Bardeen, *Phys. Rev. Lett.* **6**, 57 (1961).
- [10] C.J. Chen, *Oxford University Press, USA* (1993).
- [11] J. Tersoff, and D. Hamann, *Phys. Rev. B* **31**, 805 (1985).
- [12] Y. Martin and H. K. Wickramasinghe, *Appl. Phys. Lett.* **50**, 1455 (1987).
- [13] J. J. Saenz, N. Garc´ıa, P. Grutter, E. Meyer, H. Heinzelmann, R. Wiesendanger, L. Rosenthaler, H. R. Hidber, and H.J. Gunttherodt, *J. Appl. Phys.* **62**, 4293–4295 (1987).
- [14] G. Binnig, C. F. Quate, *Phys. Rev. Lett.* **56**, 930–933 (1986).
- [15] T. Albrecht, P. Grutter, D. Horne, and D. Rugar, *J. Appl. Phys.* **69**, 668 (1991).

The vdW ferromagnet Fe_3GeTe_2

The vdW ferromagnet Fe_3GeTe_2 crystallizes into a hexagonal lattice structure and adopts the spacegroup $P6_3/mmc$ (No. 194) [1,2]. The side view of the crystal structure of Fe_3GeTe_2 is shown in Figure 3.1 (a) with lattice parameters, $a = b = 4.015 \text{ \AA}$ and $c = 16.362 \text{ \AA}$. The Fe atoms are labeled Fe-I and Fe-II, owing to the two inequivalent Wyckoff sites they occupy. In the middle layer, the Fe-II atoms are covalently bonded with Ge, which are sandwiched between two hexagonal layers of Fe-I. This triple-layer Fe_3Ge are further sandwiched between two hexagonal Te layers, and a van der Waals gap of the order 2.96 \AA separates the resultant pentuple layers Fe_3GeTe_2 . Unlike other bulk vdW ferromagnets CrI_3 [3] and CrSiTe_3 [4], it is an itinerant ferromagnet with high Curie temperature of 220 K-230 K [1,2] which can be further increased by doping [5] or patterning [6], making it a promising candidate for next-generation spintronic devices [7,9,10]. The system shows planar topological Hall effect [11], along with significantly high uniaxial magnetic anisotropy [12–15]. Recently, it was shown that the van der Waals ferromagnet Fe_3GeTe_2 hosts Fermi surface spin-polarization, an emergent Kondo lattice behaviour, along with a large carrier mass leading to a heavy fermion character to the system [16,17]. Existence of strong correlations in Fe_3GeTe_2 are concluded from evidences of enhanced specific heat described by a high Sommerfeld coefficient pointing to a (~ 10 folds) mass enhancement [18]. In this work, we have performed Andreev reflection spectroscopy at point-contact junctions between tips of superconducting Nb and single crystals of the Kondo lattice ferromagnet Fe_3GeTe_2 . In addition, we have also studied the magnetic ground state of Fe_3GeTe_2 using MFM.

3.0 Sample details

High quality single crystals of Fe_3GeTe_2 were synthesized by chemical vapor transport using I_2 as a transport agent [19]. The stoichiometric mixture of the ingredient elements in powder form was sealed in a vacuum sealed quartz tube and was placed in a two-zone fur-

nance maintained at 750 / 700 °C for one week. Large shiny single crystals of typical sizes 5–6×3–5 mm² were obtained and the single phase was confirmed by room-temperature X-ray diffraction measurements. Owing to the van der Waals bonding between the different layers, the single crystals were cleavable by mechanical exfoliation. We have performed STM measurements on the in-situ cleaved (at 77 K) single crystal of Fe₃GeTe₂. An atomically resolved topography of area 9 nm× 9 nm, recorded at 77 K, of the Te-terminated surface of the sample is shown in Figure 3.1(b). Such atomic resolution was obtained everywhere on the surface confirming the good surface quality.

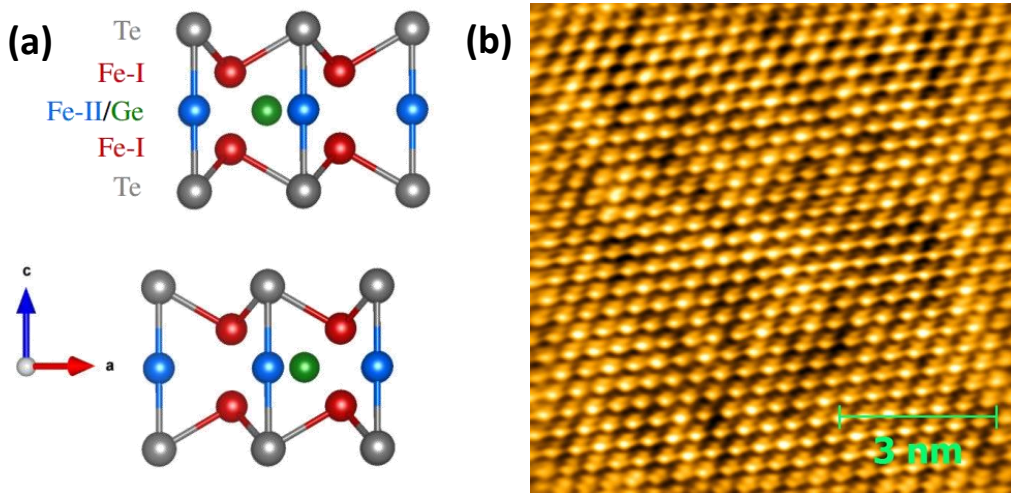


Figure 3.1: (a) Crystal structure of Fe₃GeTe₂. (b) STM topograph of 9 nm × 9 nm area taken on the cleaved surface of Fe₃GeTe₂ taken at sample bias $V_b = 0.6$ V and tunneling current $I_t = 200$ pA.

3.1 Measurement of transport spin polarization

As discussed in subsection (1.3.4), measurement of the suppression of Andreev reflection gives an estimate of the spin polarization at the Fermi surface. The problem gains additional complexity when the spin-polarized electrode forming the junction with a superconductor hosts significant electron correlations. In such cases, additional suppression of Andreev reflection is expected due to a larger effective potential barrier that would arise from the intrinsic mismatch in the Fermi velocities in the two sides of the junction [20]. The situation approaches an extreme limit when the carriers in the spin-polarized part of the junction are also characterized by a large effective mass as in the heavy Fermions. In such cases, the suppression of conductance may not be only due to spin polarization and larger potential barrier, both of which can be modelled within an appropriately modified version of the conventional Blonder-Tinkham-Klapwijk (BTK) theory [21].

The transport spectroscopic features in the aforementioned situations may also involve the signature of other electronic effects in various forms, including a Kondo anomaly [22–25]. Within the theory of electron tunneling into a Kondo lattice [26] (as in case of a point contact geometry), it was earlier shown that a co-tunneling mechanism causes spin-flip processes. In presence of that, the calculation of the conductance within a mean field picture predicts the appearance of two peaks separated by a hybridization gap in the clean limit which gets smeared out as one approaches the dirty (disordered) limit. Within this picture, even with moderate disorder, the conductance spectrum is expected to take the shape of a Fano line [27]. Such Fano lineshape behaviour were experimentally observed in point contacts with a number of heavy fermion systems in the past [22–25].

In addition to the above, other complex possibilities may also arise. For example, the superconducting phase induced (proximity) in the heavy fermionic part of the junction may achieve unconventional character in the order parameter symmetry. While such possibilities were explored experimentally in non-magnetic or weakly magnetic heavy fermion superconductors like CeCoIn₅ [22], CeCu₂Si₂, URu₂Si₂ [28], UBe₁₃, UPt₃ [29], UTe₂ [30], etc., investigation of such phenomena in a ferromagnetic Kondo lattice with heavy fermionic character was not investigated, mainly due to lack of a model system where all such physical properties would coexist.

3.1.1 PCARS on Nb / Fe₃GeTe₂ junctions

For the Andreev reflection spectroscopy experiments, a Nb tip was engaged by standard needle-anvil method on a freshly cleaved single crystal of Fe₃GeTe₂ inside a variable temperature cryostat working down to 1.4 K which is also equipped with a 3-axis superconducting vector magnet (6T-1T-1T). The point contacts were formed on the [001] facet such that the current was injected along the c-axis of the crystal. For this direction of current injection, the layered structure does not play a role in deciding the point contact resistance and its microscopic anatomy. Owing to the high quality of the single crystals, ballistic superconducting point contacts, characterized by two differential conductance (dI/dV) peaks symmetric about $V = 0$, could be established fairly easily. One such representative spectrum and its temperature dependence is shown in Figure 3.2(a). The colored points are experimentally obtained data points at different temperatures and the solid black lines are the corresponding fits within a modified BTK theory [21]– modified to incorporate the effect of the spin-polarized band structure of the ferromagnetic fraction of the point contacts. The spectra shown in the Figure 3.2(a) have been normalized relative to the differential conductance in the normal state and subsequently fitted using the modified BTK fit. An ac modulation of 0.25 mA was used in the measurements

In a normal metal-superconductor Andreev reflection process, the zero-bias conductance

should be 2 times the normal state conductance, for a fully transparent barrier and at absolute zero [31]. While finite temperature broadens the spectral features with marginal reduction of dI/dV at $T < 0.5T_c$, a non-zero interfacial barrier ($Z \neq 0$) causes suppression of the zero-bias conductance in a characteristic way that also causes enhancements (sharpening) of the dI/dV peaks near $V = \pm\Delta/e$. However, a visual inspection of the spectra presented in Figure 1(g) it is clear that the barrier is transparent (low Z), but despite that Andreev reflection has been suppressed significantly. The zero-bias enhancement is only about 6%. The spectrum could be described well within the modified BTK theory with an effective spin polarization (P_t) of 46.57%, but only with an enhanced effective temperature of 4.6 K, or a rather large (Dynes like [32]) broadening parameter (Γ) approaching 0.52 meV which is almost 0.5Δ . The need of a significantly enhanced effective temperature, or, instead, a larger Γ , is due to additional broadening effects that could be playing a role here, but the origin of which is unclear. We note that this effect is not due to contact heating because the normal state resistance did not change with increasing temperature, no additional spectral features other than the double-peak structure was seen, and Wexler's formula [33] gave an estimate of the contact diameter ~ 20 nm which is smaller than the mean free path in Fe_3GeTe_2 thereby confirming that the contacts are ballistic and no significant contact heating is expected. Since the contact diameter is smaller than the domain size, statistically, majority of the times, the point contacts are formed on single domains. Furthermore, taking the measured temperature as the contact temperature, the Δ vs. T graph is well described by the Bardeen-Cooper-Schrieffer (BCS) theory [34] (solid red line in Figure 3.2(b)). It should be noted that a significant Δ is found even at measured $T = 8\text{K}$ – any significant contact heating would make the contact non-superconducting at a much lower temperature. Furthermore, a larger effective temperature should also lead to an underestimation of P_t . There is also a possibility that certain local disorders under the point contacts, giving rise to the additional broadening. The point contacts were made on the freshly cleaved surfaces of single crystalline Fe_3GeTe_2 . Hence, the possibility of such a effect should be low – though that cannot be completely ruled out.

As per the standard practice, the intrinsic spin-polarization can be estimated by performing experiments with a number of spectra for junctions with different barrier strength (Z), and then extrapolating the Z -dependence of P_t to $Z = 0$. We investigated several other point contacts which display features of a higher Z . We show three such representative spectra, along with their modified BTK fits in Figure 3.3 (a-c). P_t was seen to monotonically decrease with increasing Z and the extrapolated dependence to $Z = 0$ revealed a spin polarization greater than 60% as shown in Figure 3.3 (d). In all these cases, however, the effective temperature (or, the artificially introduced Dyne's-like broadening parameter Γ) used for the analysis was significantly high, indicating that the intrinsic Fermi surface spin polarization could be even higher.

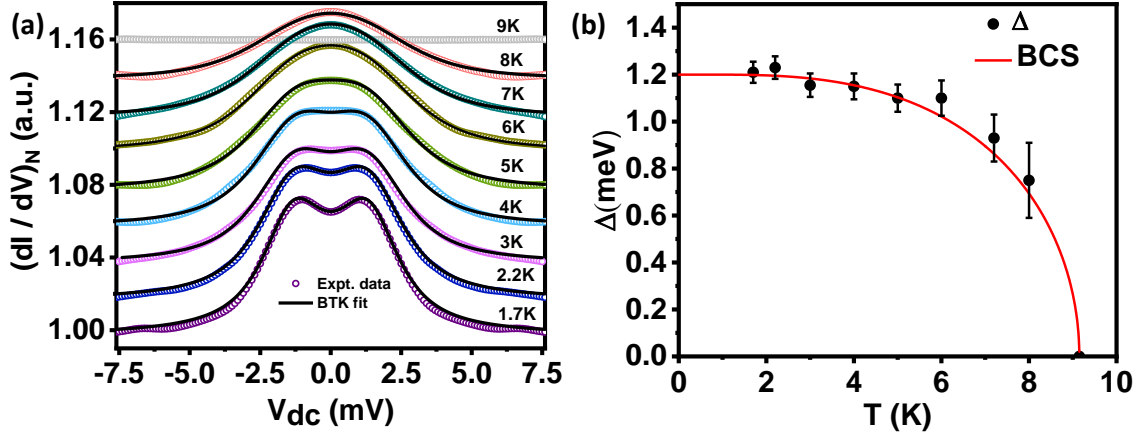


Figure 3.2: (a) Temperature dependence of ballistic spectra (shown by colored dots) and their corresponding BTK fits (shown by black line). All the spectra are normalised and equal vertical shift to spectra with respect to conductance spectrum at 1.7K is given for clarity. (b) Temperature dependence of the superconducting gap (shown by black dots). The error bars depict the range of Δ for which a reasonable fit could be obtained using a modified BTK theory. The expected variation of the gap from BCS theory is shown by solid red line.

Here we would also like to highlight that the point contact showed strong anisotropy in magnetoresistance. To investigate that, we performed field-angle dependence of the normal state resistance of one such ballistic point contact at zero bias. The orientation of the magnetic field with respect to the applied current was varied using the 3-axis vector magnet. The results for in-plane rotation (ϕ) of field and out-of-plane rotation (θ) of the magnetic field are shown in Figure 3.4 (a) and (b) respectively. The anisotropy in magnetoresistance became more pronounced with increase in the strength of the field. The anisotropic behavior followed typical $\cos^2(\phi)$ and $\cos^2(\theta)$ dependence (shown by the black lines in the Figure 3.4 (a) and (b) signifying spin-polarized nature [35] of the transport supercurrent flowing through the Nb/Fe₃GeTe₂ point contacts. It should be noted that the angular magnetoresistance has been measured for a point contact in the ballistic regime where the point contact resistance is predominantly given by Sharvin's resistance which remains independent of the bulk resistance of the materials forming a point contact. Similar results have been found in the past in on a number of ferromagnets [35, 36].

3.1.2 Bandstructure calculations

In order to gain insight on the spin-polarized Fermi surface of Fe₃GeTe₂, we performed first-principles density functional calculations. We have presented the detailed calculated band structures in Figure 3.5 (a). We focus on the key features of the calculated band structure here. The spin-polarized electronic structure analysis indicates the metallic nature of

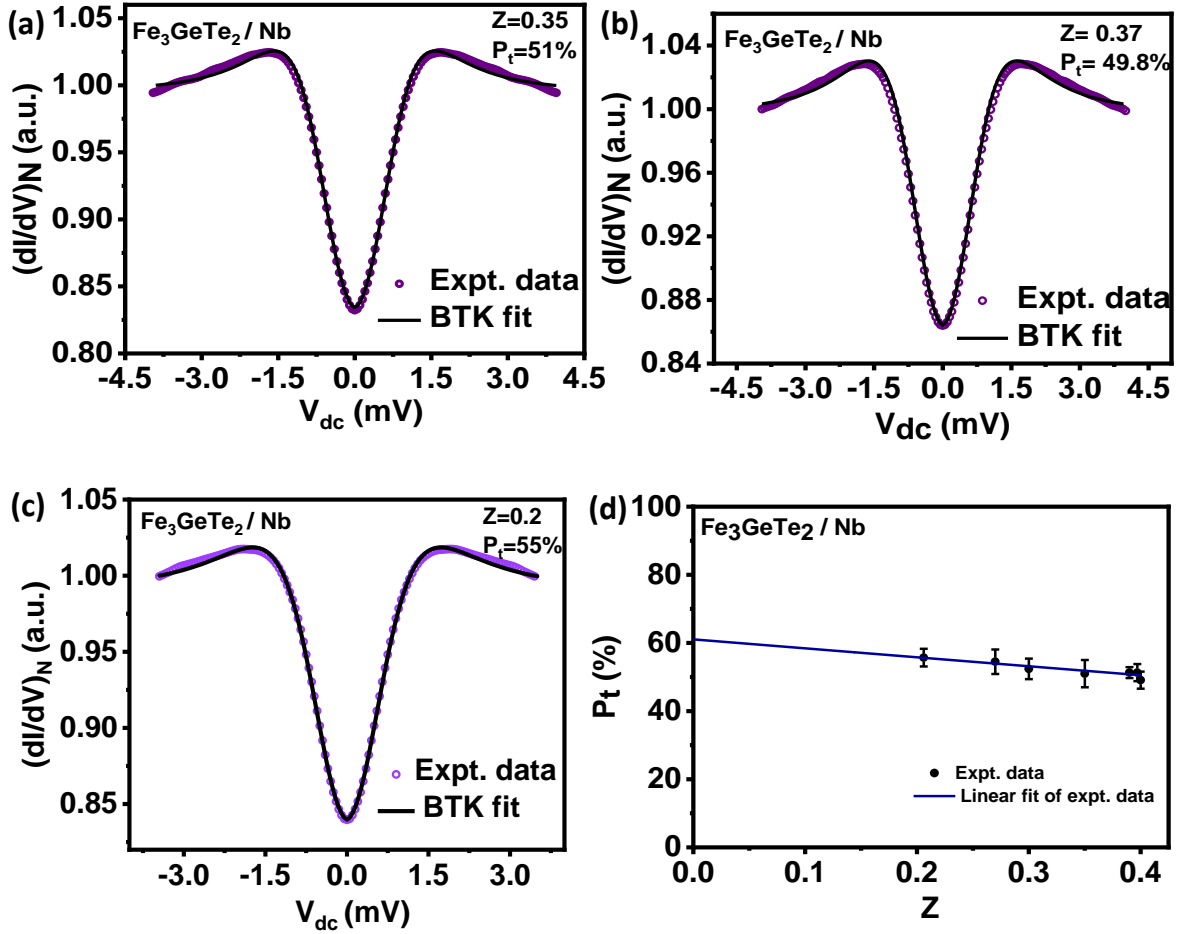


Figure 3.3: (a)-(c) Three fitted ballistic spectra with different values of barrier strength (Z) and spin polarisation (P_t). (d) P_t vs Z . The extrapolated value of P_t (at $Z=0$) is around 61%. The error bars depict the range of P_t for which a reasonable fit could be obtained using a modified BTK theory.

Fe_3GeTe_2 , which along with the non-integer magnetic moment, supports the itinerant nature of ferromagnetism. The appearance of several flat bands near the Fermi level indicates enhanced quasiparticle mass suggesting a strong electron correlation in the material. This is in agreement with the high Sommerfeld coefficient of specific heat data published in the past [18]. The states at the Fermi level are constructed with d_{yz} and d_{xz} orbitals from Fe-I hybridized with the Te- p orbitals for the majority spin channel. In addition, a contribution from the d_{xy} from Fe-II is also observed but is significantly lower. Similar trends are encountered for the minority spin channel. To note, the band structure of the system was also calculated earlier [16], though not in the context of the Fermi level spin-polarization. The key aspects of our calculations are consistent with the past calculations. We have used the calculated bands to extract additional parameters for the analysis of our experimental data. In general, as far as the transport measurements are concerned, the general expression for

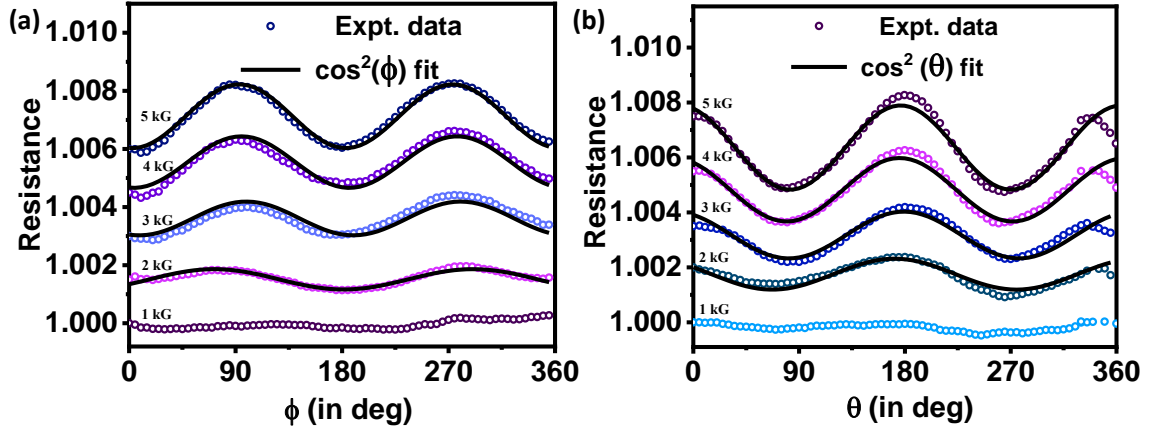


Figure 3.4: (a)-(b) In-plane and out-of plane magnetic field angle dependence of resistance taken at zero bias and 11 K. The $\cos^2(\phi)$ and $\cos^2(\theta)$ fits are shown by solid black lines. All the resistance curves are normalised and equal vertical shift to resistance curves with respect to curve at lowest magnetic field is given for clarity.

(transport) spin polarization can be written as [37]

$$P_t^n = \frac{\langle N(E_F)v_F^n \rangle_{\uparrow} - \langle N(E_F)v_F^n \rangle_{\downarrow}}{\langle N(E_F)v_F^n \rangle_{\uparrow} + \langle N(E_F)v_F^n \rangle_{\downarrow}}, \quad (3.1)$$

where v_F is the spin-polarised Fermi velocity. The Fermi velocity of the individual bands can be calculated from the slope of the individual bands at the Fermi energy. Taking the arithmetic average of the velocities of all the bands results in the the average Fermi velocity for the respective spin channels. $n = 0$ gives the net Fermi surface spin polarization which is not the relevant quantity here, as the Fermi velocity of the up and the down spin channels can be different too. In point-contact spectroscopy $n = 1$ and $n = 2$ give P_t in ballistic and diffusive regimes respectively. From our calculations, we found the average Fermi velocity of the majority spin channel to be $v_{F\uparrow} = 4.10 \times 10^5 \text{ ms}^{-1}$, which is larger than the minority spin channel, $v_{F\downarrow} = 2.86 \times 10^5 \text{ ms}^{-1}$. The observation of Fermi velocities an order of magnitude slower than that in the typical metals is consistent with the reported higher Fermion mass in the system. The calculated spin-polarized density of states at the Fermi level is $N_{\uparrow} = 4.72 \text{ states/eV/unitcell}$, that is 79% greater than N_{\downarrow} [Figure 3.5 (b)]. Therefore, the imbalance of both v_F and $N(E_F)$ result into the transport spin polarization of 44% in the ballistic regime and 58% in the diffusive regime. To note, these estimates were done at absolute zero temperature and did not involve the effects of thermal broadening at the measurement temperatures. In principle, the measured spin-polarization should be significantly smaller than the theoretically obtained numbers. However, the experimentally measured spin polarization was found to be higher even with larger effective temperatures (or higher effective broadening parameters (Γ)).

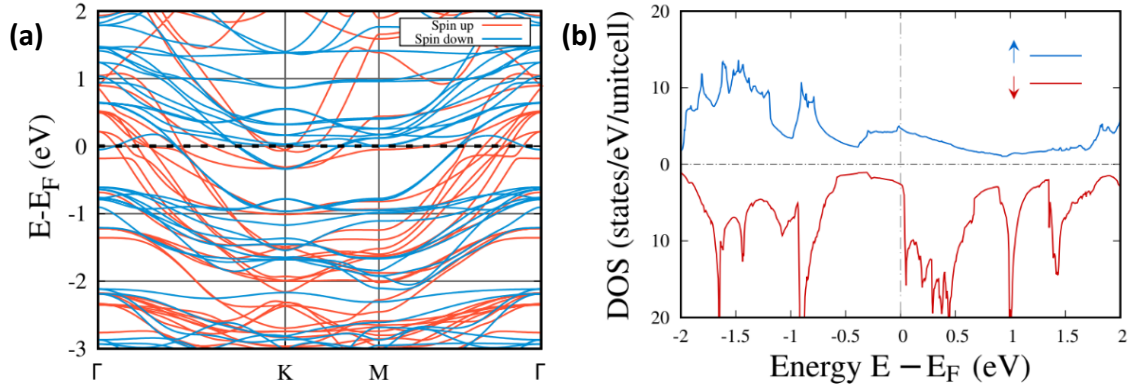


Figure 3.5: (a)-(b) Band structure and the electronic density of states (DOS) is calculated for the ferromagnetic state respectively.

3.1.3 Emergence of Kondo-lattice behavior in dI/dV spectra

The above observation motivated us to investigate the possibility of any other physics competing and/or cooperating with spin-polarized Andreev reflection at the Nb/Fe₃GeTe₂ interfaces. For that, we gradually increased the temperature of the point contact for a high Z contact, as shown in Figure 3.6 (a), and noted the spectral features over a larger bias range ($\pm 40mV$). As it was mentioned before, the central dip in an Andreev reflection spectrum is primarily due to non-zero Z and P_t , and that should disappear at the T_c of the superconductor forming the junction. However, we found that the central dip structure remained even above 10 K, definitely above the T_c of Nb. Moreover, the normal state spectra also displayed broad conductance peaks around $\pm 18mV$. These peaks compete with the Andreev reflection features in the superconducting state thereby causing anomalous features near 15 mV, where the background gives a downward trend to dI/dV with decreasing V , while the peaks due to Andreev reflection give an upward trend. It is this competition that brings the zero-bias conductance of the 10K spectrum below the 7 K spectrum. In this context, we note that the relative strength of the background anomaly and the enhancement due to Andreev reflection are seen to be different at different points. A visual inspection of the spectra presented in Figure 3.6 (a) and Figure 3.3 (a)-(c) clearly reveals this difference.

Now it is important to understand the special features in dI/dV that appeared above the T_c of Nb. A careful inspection of the normal state data reveals an asymmetry between the $\pm V$ regions. As shown in the inset of Figure 3.6 (a), the asymmetry observed in our data at 10 K could be fit well with a Fano line-shape [27]. The line-shape was generated using the formula:

$$dI/dV \propto \frac{(\varepsilon + q)^2}{1 + \varepsilon^2}; \varepsilon = \frac{eV - \varepsilon_0}{\gamma} \quad (3.2)$$

Here, V is the dc bias, q is the asymmetry factor, ε_0 is the position of the resonance in

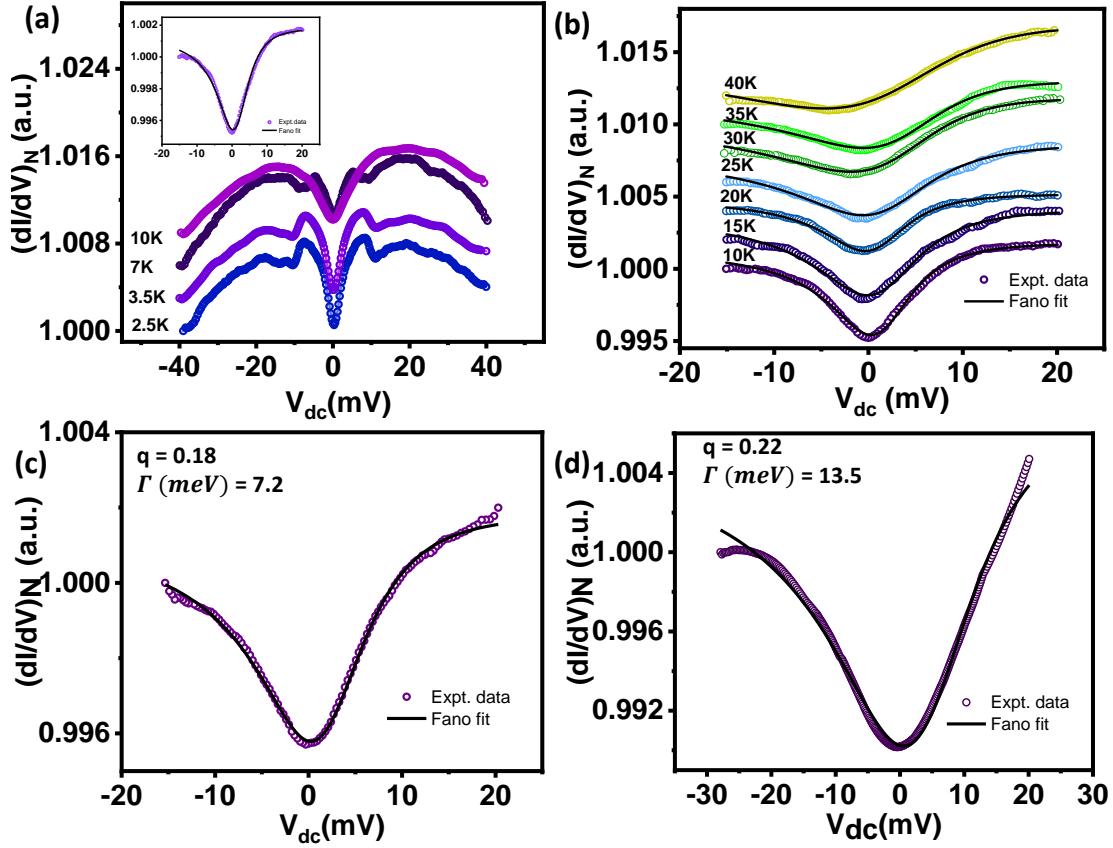


Figure 3.6: (a) The temperature dependence of high Z point contact. The inset shows the Fano lineshape fitting (shown by black line) of the conductance spectrum (shown by colored dots) taken at 10 K. (b) Temperature dependence of the normal state along with the Fano lineshape fits. Spectra are vertically shifted for clarity. (c)-(d) Two normalised conductance spectra (shown by colored dots) and their Fano lineshape fitting (shown by black line) taken at 12 K.

the energy scale, γ is the resonance at HWHM (half width at half maximum). Since a Kondo lattice behavior has already been reported in Fe_3GeTe_2 [16, 17], it is rational to attribute the Fano-like normal state feature with Kondo effect in a Kondo lattice. The normal state of various ballistic contacts was investigated and two such normal state spectra along with Fano fitting parameters are shown in the Figure 3.6 (c)-(d). For a Kondo lattice like Fe_3GeTe_2 , under a point contact geometry, within a two-channel model, the special line shape might be due to the interference between the two current paths, one through the channel of the itinerant electrons and the other one through the quasiparticles that have attained a significantly higher mass due to the interaction between the d -electron spins and the spins of the itinerant electrons. In Figure 3.6 (b), we investigated the normal state spectra and their Fano line shape as a function of increasing temperature. The resonance width given by γ increases with increasing temperature. This behavior is commonly seen in Kondo-induced Fano line shapes of dI/dV spectra. Such Fano lineshape fitting of experimental

point contact spectra was also done for a number of heavy Fermionic superconductors in the past, including CeCoIn₅ [22, 23] and URu₂Si₂ [24].

3.2 Stripes and bubbles

Realization and manipulation of novel magnetic textures in metallic systems is important for their application in next generation spintronics. Motivated by the observation of itinerant ferromagnetism in the 2D ferromagnets Fe_nGeTe₂ ($n \geq 3$), we have theoretically modelled a 2D triangular lattice with spin-orbit coupling and itinerant magnetism and found a ground state with filamentary magnetic domain walls. Our magnetic force microscopy experiments on Fe₃GeTe₂ revealed strikingly similar domain walls. While the initial model predicted the formation of skyrmions, the filaments on Fe₃GeTe₂ were seen to break into large size magnetic bubbles with magnetic field. This effect was understood by adding the role of magnetic anisotropy in the model. From our analysis of the theoretical model and the experimental data we demonstrate how different types of topological magnetic structures can be stabilized in real systems.

3.2.1 The model

In metallic magnets that consist of large magnetic moments and SOC, a generic starting model is the ferromagnetic Kondo lattice model (FKLM) in the presence of a Rashba term. We consider the Hamiltonian on a triangular lattice as,

$$\begin{aligned}
H = & -t \sum_{i,\gamma,\sigma} (c_{i,\sigma}^\dagger c_{i+\gamma,\sigma} + \text{H.c.}) - J_H \sum_i \mathbf{S}_i \cdot \mathbf{s}_i \\
& -i\lambda \sum_{i,\gamma,\sigma\sigma'} c_{i\sigma}^\dagger [\boldsymbol{\tau} \cdot (\hat{\boldsymbol{\gamma}} \times \hat{\mathbf{z}})]_{\sigma\sigma'} c_{j\sigma'} - h_z \sum_i S_i^z.
\end{aligned} \tag{3.3}$$

The annihilation (creation) operators, $c_{i\sigma}$ ($c_{i\sigma}^\dagger$), satisfy the usual Fermion algebra. J_H (λ) denotes the strength of Kondo (Rashba) coupling, t is the nearest neighbor hopping parameter on a triangular lattice. $\boldsymbol{\tau}$ is a vector operator with the three Pauli matrices as components. \mathbf{s}_i (\mathbf{S}_i) denotes the electronic spin operator (localized classical spin) at site i . Assuming the lattice constant to be unity, $\hat{\boldsymbol{\gamma}} \in \{\mathbf{a}_1, \mathbf{a}_2, \mathbf{a}_3\}$ are the primitive vectors of the triangular Bravais lattice with $\mathbf{a}_1=(1,0)$, $\mathbf{a}_2=(1/2, \sqrt{3}/2)$ and $\mathbf{a}_3=(-1/2, \sqrt{3}/2)$. The last term in equation (3.3) represents the Zeeman coupling of local moments to an external magnetic field of strength h_z . $t = 1$ sets the basic energy unit in the model. Taking the limit of large Kondo coupling, we obtain [40],

$$H_{\text{RDE}} = \sum_{\langle ij \rangle, \gamma} [g_{ij}^\gamma d_i^\dagger d_j + \text{H.c.}] - h_z \sum_i S_i^z, \quad (3.4)$$

where, $d_i(d_i^\dagger)$ annihilates (creates) an electron at site i with spin parallel to the localized spin. Site $j = i + \gamma$ is the nn of site i along one of the three symmetry directions on the triangular lattice. The projected hopping g_{ij}^γ depend on the orientations of the local moments \mathbf{S}_i and \mathbf{S}_j . The tight-binding, t_{ij}^γ and Rashba, λ_{ij}^γ , contributions to $g_{ij}^\gamma = t_{ij}^\gamma + \lambda_{ij}^\gamma$ are given by [40],

$$\begin{aligned} t_{ij}^\gamma &= -t \left[\cos\left(\frac{\theta_i}{2}\right) \cos\left(\frac{\theta_j}{2}\right) + \sin\left(\frac{\theta_i}{2}\right) \sin\left(\frac{\theta_j}{2}\right) e^{-i(\phi_i - \phi_j)} \right], \\ \lambda_{ij}^{\mathbf{a}_1} &= \lambda_{ij}^x, \quad \lambda_{ij}^{\mathbf{a}_{2/3}} = \pm \frac{1}{2} \lambda_{ij}^x + \frac{\sqrt{3}}{2} \lambda_{ij}^y, \\ \lambda_{ij}^x &= \lambda \left[\sin\left(\frac{\theta_i}{2}\right) \cos\left(\frac{\theta_j}{2}\right) e^{-i\phi_i} - \cos\left(\frac{\theta_i}{2}\right) \sin\left(\frac{\theta_j}{2}\right) e^{i\phi_j} \right], \\ \lambda_{ij}^y &= i\lambda \left[\sin\left(\frac{\theta_i}{2}\right) \cos\left(\frac{\theta_j}{2}\right) e^{-i\phi_i} + \cos\left(\frac{\theta_i}{2}\right) \sin\left(\frac{\theta_j}{2}\right) e^{i\phi_j} \right], \end{aligned} \quad (3.5)$$

where θ_i (ϕ_i) is the polar (azimuthal) angle for localized moment \mathbf{S}_i . The Hamiltonian equation (3.4) describes a modified tight-binding model where the hopping integrals are dependent on the configuration of classical spins. Therefore, the energy of the system depends on the classical spin configurations. This dependence can be formally written as an effective spin Hamiltonian by following a procedure well known for double-exchange models [40, 41]. For the present case of Rashba coupling on a triangular lattice, we obtain,

$$\begin{aligned} H_{\text{eff}} &= - \sum_{\langle ij \rangle, \gamma} D_{ij}^\gamma f_{ij}^\gamma - h_z \sum_i S_i^z, \\ \sqrt{2} f_{ij}^\gamma &= [t^2(1 + \mathbf{S}_i \cdot \mathbf{S}_j) + 2t\lambda\hat{\gamma} \cdot (\mathbf{S}_i \times \mathbf{S}_j) \\ &\quad + \lambda^2(1 - \mathbf{S}_i \cdot \mathbf{S}_j + 2(\hat{\gamma} \cdot \mathbf{S}_i)(\hat{\gamma} \cdot \mathbf{S}_j))]^{1/2}, \\ D_{ij}^\gamma &= \langle [e^{ih_{ij}^\gamma} d_i^\dagger d_j + \text{H.c.}] \rangle_{gs}. \end{aligned} \quad (3.6)$$

In the above, f_{ij}^γ (h_{ij}^γ) is the modulus (argument) of complex number g_{ij}^γ , and $\langle \hat{O} \rangle_{gs}$ denotes expectation values of operator \hat{O} in the ground state. The low-temperature magnetic states, with varying strengths of SOC, are shown in Figure 3.7. For small to intermediate values of λ/t , we found the filamentary domain structure of spins (see Figure 3.7 (a)-(b)). The thickness of these domains decreases with the increasing strength of SOC. For a sufficiently large lattice size, we found that the filaments are oriented in all possible directions. This freedom of the domains to orient freely in any direction is a consequence of the anisotropic

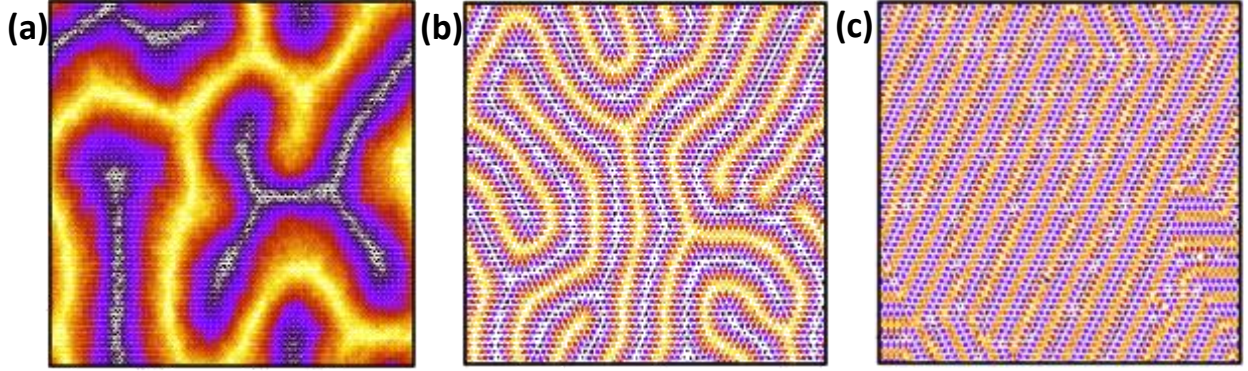


Figure 3.7: (Color online) Real-space view of spin configurations at low temperature ($T/t = 0.01$) for (a) $\lambda/t = 0.1$, (b) $\lambda/t = 0.5$ and (c) $\lambda/t = 1$.

DM interaction encoded in the linear in λ term in the f_{ij} in the Hamiltonian equation (3.6). For larger values of λ/t , we obtained a spin-spiral state as shown in Figure 3.7(c). The origin of this state is related to the importance of the λ^2 term in the effective Hamiltonian. Note that the λ^2 term prefers Ising-like interactions of different components along different directions, leading to a classical Kitaev model with degenerate ground states. Therefore, there are three states, related by the rotational symmetry of the triangular lattice, that can be realized as ground states. Assuming constant coupling parameters have been shown to be a good approximation for studying ground state phases of H_{eff} [40], therefore we set $D_{ij}^{\gamma} \equiv D_0 = 1/\sqrt{2}$ to study H_{eff} . We performed Monte Carlo (MC) simulations on the Hamiltonian equation (3.6) via the standard Markov chain MC using the Metropolis algorithm.

3.2.2 MFM results on Fe_3GeTe_2

Now we focus on the experimentally observed magnetic domain structures on Fe_3GeTe_2 where the characteristic features of the model, namely the existence of ferromagnetism, metallicity, and high spin-orbit coupling exist naturally. We imaged the magnetic domains in Fe_3GeTe_2 by magnetic force microscopy (MFM) performed at different temperatures and under magnetic fields. At the lowest temperature, in the absence of any external magnetic field treatment, we found clear stripe domains with a typical stripe width of ~ 700 nm (Figure 3.8 (a)). The filamentary domains in a large-size crystal are a consequence of strong uniaxial anisotropy, as is usually reported for Fe_3GeTe_2 from bulk magnetization measurements [12, 38, 39]. The alternative contrast of the filamentary domains corresponds to the region of opposite magnetization. The temperature evolution of the ferromagnetic domains is presented in Figure 3.8 (b)-(d). The width of the stripe domains increases with an increase in temperature and disappears at 205 K, near the Curie temperature. The domain structure at the lowest temperature involves stripes and interconnects with striking similarities with the simulated filamentary domains as shown in Figure 3.7(b). Therefore, it appears that

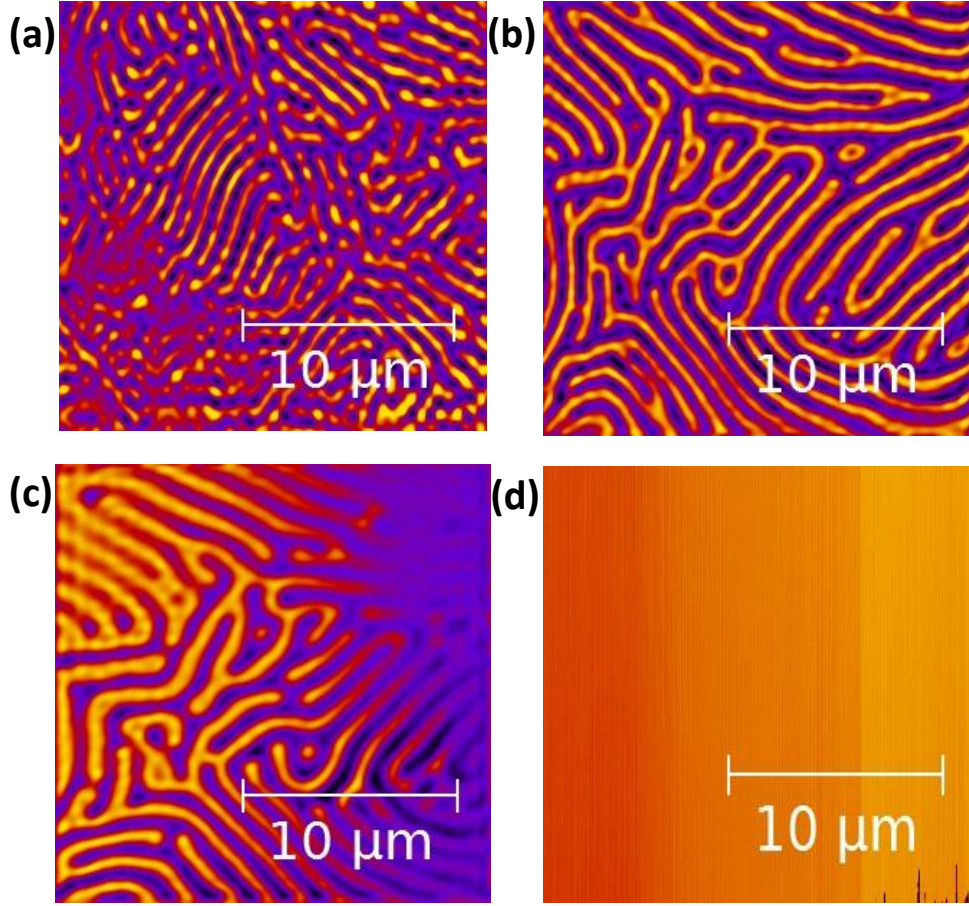


Figure 3.8: MFM dual pass phase images taken on the single crystals of Fe_3GeTe_2 , at different temperatures, showing contrast of ferromagnetic domains in the zero field cooled state. The sample temperature for the images is (a) 1.6 K (b) 93 K (c) 165 K and (d) 205 K. As the sample temperature is increased to 205 K the stripy domains vanishes.

Fe_3GeTe_2 hosts moderate spin-orbit coupling with $\lambda/t \sim 0.5$.

In order to gain further understanding on the magnetic state of Fe_3GeTe_2 , we performed MFM imaging in the field cooled (FC) states of the crystal. We first field-cooled the crystal under the magnetic field of the MFM cantilever and then performed MFM imaging at 1.6 K. Under this condition, as shown in Figure 3.9 (a), we found that circular domains (the dark circles) have formed within the stripes with the magnetization pointing opposite to the direction of the tip-magnetization, along with rows of circular domains with the magnetization aligned in the opposite direction (the bright circles). This feature was reported earlier in Fe_3GeTe_2 and is typical for ferromagnets with high perpendicular magnetic anisotropy. Interestingly, at several points, the stripes have also started breaking up into fragments. In order to investigate the microscopic structure in further detail, we imaged a smaller area (Figure 3.9 (b)) under the same condition where we find an assembly of bright circular domains with a background hosting the fragmented stripes. In the model, the zero-field cooled protocol was followed with the temperature reduced to $T/t = 0.01$ in the absence of a mag-

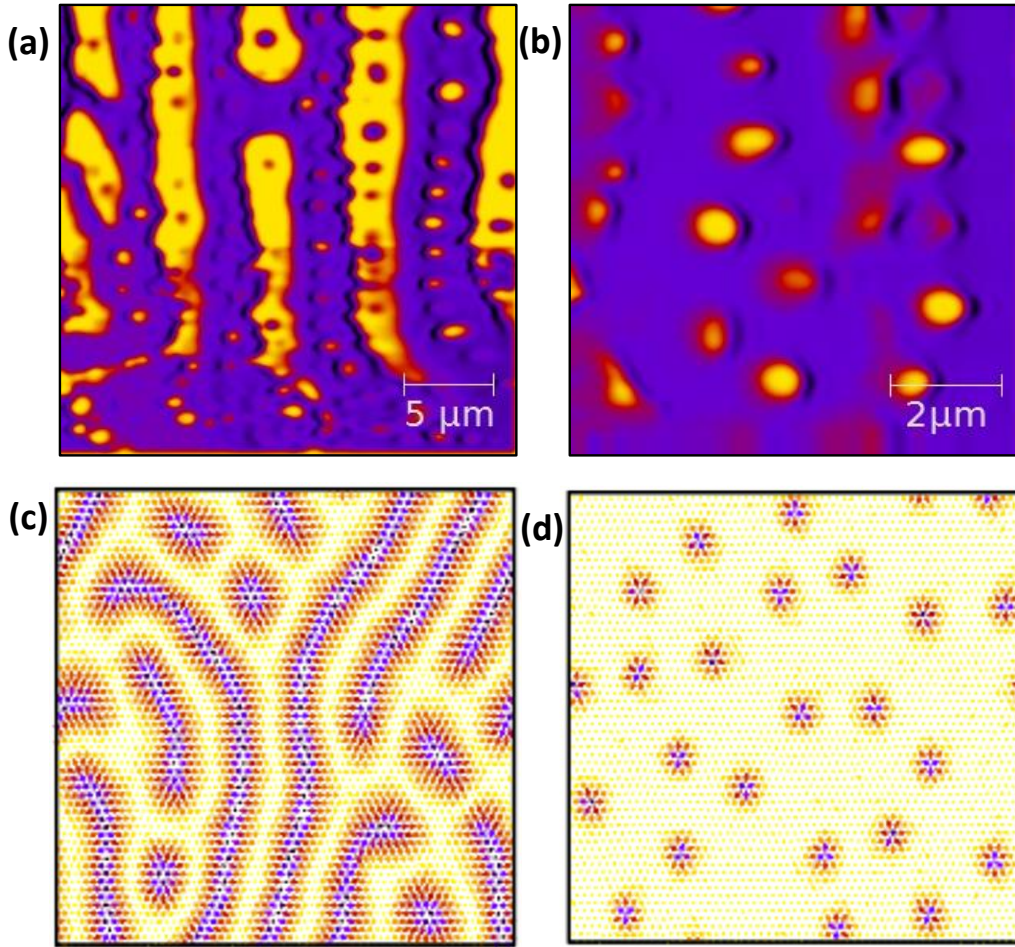


Figure 3.9: (a)-(b) MFM dual pass phase images taken in the field-cooled state in the presence of the stray field of the MFM cantilever. (Color online) Representative spin configurations at $T/t = 0.01$ and $\lambda/t = 0.5$ for (c) $h_z = 0.44$ and (d) $h_z = 0.84$.

netic field followed by the increase of field in a step-wise manner until a fully saturated ferromagnetic state is obtained. Within the model, for intermediate values of the SOC strength, the filamentary domains break into Skyrmions on increasing field strength (Figure 3.9 (c-d)).

In search of a deeper understanding of the difference between the experiment and the model, we studied the effect of a higher external field. For that, the crystal was first warmed up to 300 K and was then field cooled under an applied magnetic field of 1.2 kOe. The magnetic domains were then imaged at zero applied field. As shown in Figure 3.10 (a), in a given area, we found that most of the domains are circular in shape exhibiting bright rings along the perimeters with a darker central region. Along with that, there are fragmented flat domains. For the circular domains, there is a smooth gradient of color contrast indicating a gradient of the magnetization direction as one moves out from the center, along the radius of the circular domains. In another region, where the surface is slightly tilted with respect to the MFM tip, the domains were imaged from an oblique direction which revealed a vortex-

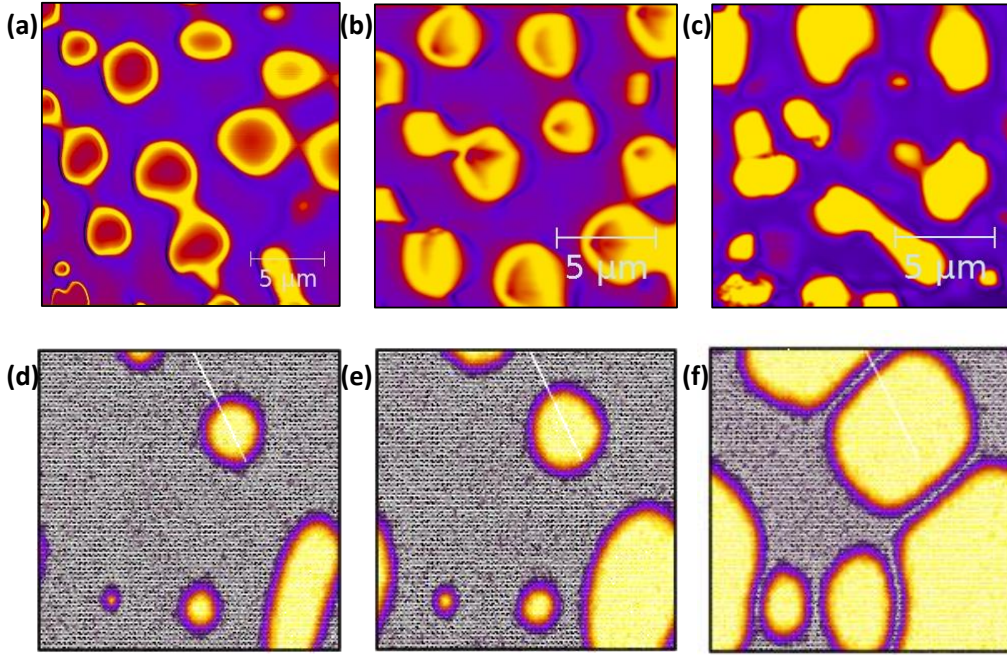


Figure 3.10: (a)-(c) MFM dual pass images in the field-cooled state (FC) where an external field of 1.2 kOe was applied. The lift height was kept constant at 30 nm for all the images. (Color online) Representative spin configurations at $T/t = 0.01$, $\lambda/t = 0.1$ and $A_u = 0.08$ for (d) $h_z = 0.004$, (e) $h_z = 0.016$ and (f) $h_z = 0.028$.

like shape of the domains (Figure 3.10 (b)). This means, in Figure 3.10 (a), the ring-like domains are merely the top view of the vortices. We then moved to an area where the flat domains are more in number in order to investigate the distribution of their size and shape. As shown in Figure 3.10 (c), the flat domains appear to be fragments of the stripes in Figure 3.9 (a). The domains have condensed into different shapes including nearly circular and elongated ones. However, the modeled results in the presence of an external magnetic field, shown in Figure 2(d-f), are different from the field-cooled MFM images.

To account for the discrepancy, we note that the model discussed so far did not include an important feature of the material, *i.e.*, the presence of easy-axis anisotropy. It is important to ask if the presence of easy axis anisotropy can explain the presence of large ferromagnetic bubbles in Fe_3GeTe_2 and Fe_4GeTe_2 . In order to check this, we included an additional term, $-A_u \sum_i (S_i^z)^2$, in the Hamiltonian equation (3.6). Positive values of A_u represent an easy-axis scenario relevant to the materials under discussion. We found that the anisotropy scale competes with the DM terms and therefore, the tendency of spins to continuously tilt away from the single skyrmion-core spin is suppressed. This leads to an expansion of the skyrmion core and finite regions with ferromagnetic bubble character are stabilized (Fig. 3.10 (d-f)). These are similar to the ring-like domain structures seen at 1.2 kOe. At even higher magnetic

fields the model generated larger size flat regions that show striking similarities with the flat regions seen experimentally. The variation of the experimental domain structure from point to point could be attributed to an inhomogeneity of the surface properties which might arise from an inhomogeneous distribution of the Fe vacancies in the system. Therefore, the results obtained in the simulations including an easy-axis anisotropy are now consistent with the evolution of the MFM images with an applied magnetic field.

3.3 Conclusion

Therefore, from the analysis of the superconducting and the normal state point contact spectra, it is understood that the Andreev reflection features appear in the presence of a strong background due to the Kondo lattice behavior of Fe_3GeTe_2 . The Kondo-related features interplay with the superconductivity-related features below the T_c of Nb. Since the Kondo anomaly at zero bias contributes to the overall conductance drop at $V = 0$, a modified BTK fit without incorporating Kondo effect is expected to give an overestimate of P_f . In other words, an enhanced P_f needs to be used to take into account the additional suppression of the low-bias Andreev reflection due to the presence of the Kondo lattice background. This explains the apparent discrepancy between the experimentally measured parameters with the estimates using the band structure calculations. We explicitly demonstrate, via large-scale Monte Carlo (MC) simulations, that the ground state consists of filamentary domain structures which show remarkable agreement with the magnetic force microscopy images on Fe_3GeTe_2 . However, the MFM images in presence of an external magnetic field deviates from the in-field calculations within the initial model. We show that inclusion of a uniaxial anisotropy term in the Hamiltonian allows for a consistent description of the results at zero and finite magnetic fields. This helped us identify magnetic anisotropy as an important tuning parameter for the relative stability of different types of topological structures in a spin-orbit coupled itinerant magnet.

3.4 Contributions

- **Fe_3GeTe_2 single crystals:** Chandan Patra, Rajeswari Roy Chowdhury and Ravi P. Singh, Department of Physics, Indian Institute of Science Education and Research (IISER) Pune, PO 411008, India.
- **Bandstructure calculations and analysis:** Basavaraja G and Mukul Kabir Department of Physics, Indian Institute of Science Education and Research (IISER) Pune, PO 411008, India.
- **Montecarlo simulations:** Soumyaranjan Dash and Sanjeev Kumar, Department of Physics, Indian Institute of Science Education and Research (IISER) Mohali, PO 140306, India.

- Some parts of the PCAR and MFM measurements were carried out jointly with Aswini R and Sandeep Howlader, Department of Physics, Indian Institute of Science Education and Research (IISER) Mohali, PO 140306, India.

Bibliography

- [1] H.-J. Deiseroth, K. Aleksandrov, C. Reiner, L. Kienle, and R. K. Kremer, *Eur. J. Inorg. Chem.* **2006**, 1561(2006).
- [2] B. Chen, J. Yang, H. Wang, M. Imai, H. Ohta, C. Michioka, K. Yoshimura, and M. Fang, *J. Phys. Soc. Japan* **82**, 124711 (2013).
- [3] B. Huang, G. Clark, E. Navarro-Moratalla, D. R. Klein, R. Cheng, K. L. Seyler, D. Zhong, E. Schmidgall, M. A. McGuire, D. H. Cobden, W. Yao, D. Xiao, P. Jarillo-Herrero, X. Xu, *Nature* **546**, 270 (2017)
- [4] M. -W. Lin, H. L. Zhuang, J. Yan, T. Z. Ward, A. A. Purotzky, C. M. Rouleau, Z. Gai, L. Liang, V. Meunier, B. G. Sumpter, P. Ganesh, P. R. C. Kent, D. B. Geohegan, D. G. Mandrusbc, K. Xiao, *J. Mater. Chem. C* **4**, 315 (2016)
- [5] Y. Deng, Y. Yu, Y. Song, J. Zhang, N. Z. Wang, Z. Sun, Y. Yi, Y. Z. Wu, S. Wu, J. Zhu, J. Wang, X. H. Chen, Y. Zhang, *Nature* **563**, 94-99 (2018)
- [6] Q. Li, M. Yang, C. Gong, R. V. Chopdekar, A. T. N'Diaye, J. Turner, G. Chen, A. Scholl, P. Shafer, E. Arenholz, A. K. Schmid, S. Wang, K. Liu, N. Gao, A. S. Admasu, S.W Cheong, C. Hwang, J. Li, F. Wang, X. Zhang, Z. Qiu, *Nano Lett.* **18**, 5974 (2018)
- [7] K. S. Burch, D. Mandrus, J.-G. Park, *Nature* **563**, 47 (2018)
- [8] K. F. Mak, J. Shan, D. C. Ralph, *Nat Rev Phys* **1**, 646–661 (2019)
- [9] K. F. Mak, J. Shan, D. C. Ralph, *Nat Rev Phys* **1**, 646–661 (2019)
- [10] C. Gong, X. Zhang, *Science* **363**, eaav4450 (2019)
- [11] Y. You, Y. Gong, H. Li, Z. Li, M. Zhu, J. Tang, E. Liu, Y. Yao, G. Xu, F. Xu, W. Wang, *Phys. Rev. B* **100**, 134441 (2019)

- [12] N. León-Brito, E. D. Bauer, F. Ronning, J. D. Thompson, R. Movshovicha, *J. Appl. Phys.* **120**, 083903 (2016)
- [13] H. L. Zhuang, P. R. C. Kent, R. G. Hennig, *Phys. Rev. B* **93**, 134407 (2016)
- [14] V. Yu. Verchenko, A. A. Tsirlin, A. V. Sobolev, I. A. Presniakov, A. V. Shevelkov, *Inorg. Chem.* **54**, 8598 (2015)
- [15] B. Chen, J.-H. Yang, H. Ohta, C. Michioka, K. Yoshimura, *J. Jpn. Soc. Powder Metall.* **57**, 172 (2010)
- [16] Y. Zhang, H. Lu, X. Zhu, S. Tan, W. Feng, Q. Liu, W. Zhang, Q. Chen, Y. Liu, X. Luo, D. Xie, L. Luo, Z. Zhang, X. Lai, *Sci. Adv.* **4**, eaao6791 (2018).
- [17] M. Zhao, B.-B. Chen, Y. Xi, Y. Zhao, H. Xu, H. Zhang, N. Cheng, H. Feng, J. Zhuang, F. Pan, X. Xu, W. Hao, W. Li, S. Zhou, S. X. Dou, Y. Du, *Nano Lett.* **21**, 6117–6123 (2021)
- [18] J.-X. Zhu, M. Janoschek, D. S. Chaves, J. C. Cezar, T. Durakiewicz, F. Ronning, Y. Sassa, M. Mansson, B. L. Scott, N. Wakeham, E. D. Bauer, and J. D. Thompson, *Phys. Rev. B* **93**, 144404 (2016)
- [19] R. R. Chowdhury, S. DuttaGupta, C. Patra, O. A. Tretiakov, S. Sharma, S. Fukami, H. Ohno, R. P. Singh, *Sci. Rep.* **11**, 14121 (2021)
- [20] E. Tuuli, K. Gloos, *Low temp Phys* **37**, 485 (2011)
- [21] R. J. Soulen Jr., M. S. Osofsky, B. Nadgorny, T. Ambrose, P. Broussard and S. F. Cheng, *J. Appl. Phys.* **85**, 4589 (1999)
- [22] W. K. Park, J. L. Sarrao, J. D. Thompson, L. H. Greene, *Phys. Rev. Lett.* **100**, 177001 (2008)
- [23] M. Fogelström, W. K. Park, L. H. Greene, G. Goll, M. J. Graf, *Phys. Rev. B* **82**, 014527 (2010)
- [24] W. K. Park, P. H. Tobash, F. Ronning, E. D. Bauer, J. L. Sarrao, J. D. Thompson, L. H. Greene, *Phys. Rev. Lett.* **108**, 246403 (2012)
- [25] Y.-F. Yang, *Phys. Rev. B* **79**, 241107(R) (2009)
- [26] M. Maltseva, M. Dzero, and P. Coleman, *Phys. Rev. Lett.* **103**, 206402(2009)
- [27] U. Fano, *Phys. Rev.* **124**, 1866 (1961)

- [28] Y. De Wilde, J. Heil, A. G. M. Jansen, P. Wyder, R. Deltour, W. Assmus, A. Menovsky, W. Sun, and L. Taillefer *Phys. Rev. Lett.* **72**, 2278 (1994)
- [29] A. Nowack, A. Heinz, F. Oster, D. Wohlleben, G. Güntherodt, Z. Fisk, and A. Menovsky, *Phys. Rev. B* **36**, 2436(R)(1987).
- [30] L. Jiao, S. Howard, S. Ran, Z. Wang, J. O. Rodriguez, M. Sigrist, Z. Wang, N. P. Butch, V. Madhavan, *Nature* **579**, 523–527 (2020)
- [31] G. E. Blonder, M. Tinkham, and T. M. Klapwijk, *Phys. Rev. B* **25**, 4515 (1982).
- [32] R. C. Dynes, V. Narayanamurti, and J. P. Garno, *Phys. Rev. Lett.* **41**, 1509 (1978).
- [33] A. Wexler, *Proc. Phys. Sov.* **89**, 927 (1966).
- [34] J. Bardeen, L. N. Cooper, J. R. Schrieffer, *Phys. Rev.* **108**, 1175 (1957).
- [35] L. Aggarwal, S. Gayen, S. Das, R. Kumar, V. Su, C. Felser, C. Shekhar, and G. Sheet, *Nat. Commun.* **8**, 13974 (2016).
- [36] S. Howlader, S. Saha, R. Kumar, V. Nagpal, S. Patnaik, T. Das, G. Sheet, *Phys. Rev. B* **102**, 104434 (2020).
- [37] I. I. Mazin, *Phys. Rev. Lett.* **83**, 1427 (1999)
- [38] L. Cai, C. Yu, L. Liu, W. Xia, H.-A. Zhou, L. Zhao, Y. Dong, T. Xu, Z. Wang, Y. Guo, Y. Zhao, J. Zhang, L. Yang, L. Yang, W. Jiang, *Appl. Phys. Lett.* **117**, 192401 (2020).
- [39] H. Wang, C. Wang, Z.-A. Li, H. Tian, Y. Shi, H. Yang, J. Li, *Appl. Phys. Lett.* **116**, 192403 (2020).
- [40] D. S. Kathyat, A. Mukherjee, and S. Kumar, *arXiv:2003.11245* (2020).
- [41] S. Kumar and P. Majumdar, *Eur. Phys. J. B* **46**, 315 (2005).

The near room temperature vdW ferromagnet Fe_4GeTe_2

Metallic 2-D ferromagnet, Fe_4GeTe_2 , crystallizes in a trigonal lattice structure with the space group $R\bar{3}m$ [1]. The side view of the crystal structure of Fe_4GeTe_2 is shown in Figure 4.1 (a) with lattice parameters, $a = b = 4.04 \text{ \AA}$ and $c = 29.14 \text{ \AA}$. The Fe atoms are labeled Fe-I and Fe-II, owing to the two inequivalent Wyckoff sites they occupy. It has a middle Ge layer with Fe-I and Fe-II dumbbells placed alternately above and below its plane. Two hexagonal layers of Te encapsulate these Fe_4Ge layers from top and bottom, forming Fe_4GeTe_2 layer, and a van der Waals gap of the order of 3.03 \AA separates these layers. Within the Fe_nGeTe_2 family, Fe_4GeTe_2 is very special because it displays a rich magnetic phase diagram with novel thermodynamic phase transitions even within the ferromagnetic phase. The system shows a ferromagnetic transition at $T_{\text{Curie}} = 270 \text{ K}$ that is followed by a spin-reorientation transition below $T_{\text{SR}} \approx 110 \text{ K}$ [2–4]. This is not seen in any other member of the family [5, 6]. From the magnetization experiments, it is believed that at T_{SR} , the system undergoes a dramatic change in magnetic anisotropy – from an in-plane (ab -plane) magnetic anisotropy at $T > T_{\text{SR}}$ to an out of plane anisotropy (perpendicular to the ab -plane) at $T < T_{\text{SR}}$. The temperature-dependent magnetization far below T_{Curie} shows multiple anomalous features that are extremely sensitive to the direction and strength of the applied magnetic field. Heat capacity measurements and detailed entropy analysis suggest that the transition at T_{SR} is a thermodynamic phase transition [3]. Studies have demonstrated that reducing the thickness of Fe_4GeTe_2 to a few layers enhances perpendicular magnetic anisotropy and strengthens its hard ferromagnetic nature [1]. These findings indicate that the magnetism in Fe_4GeTe_2 is remarkably diverse and intricate due to the spin reorientation transition. Although the magnetic properties of Fe_4GeTe_2 have been partially explored, the influence of different scattering mechanisms on electronic transport has not been thoroughly investigated. The coexistence of numerous quantum phenomena establishes Fe_4GeTe_2 as an

exceptional and significantly more complex electronic system compared to other known 2D ferromagnets .

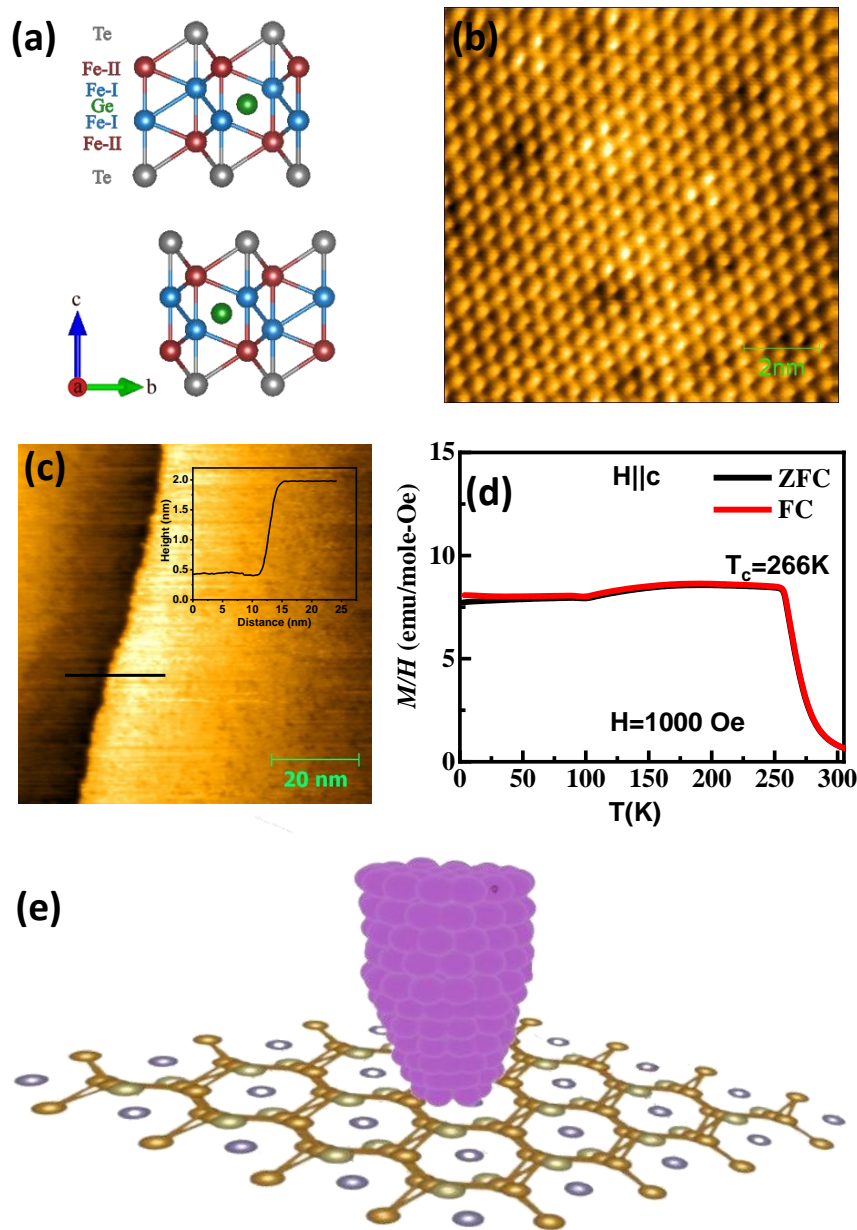


Figure 4.1: (a) Crystal structure of Fe₄GeTe₂. (b) STM topograph of 7.7 nm × 7.7 nm area taken on the cleaved surface of Fe₄GeTe₂ at sample bias $V_b = 0.82$ V and tunneling current $I_t = 200$ pA. The atoms are clearly resolved. (c) STM topograph of area 80 nm × 80 nm showing step taken at $V_b = 0.9$ V and tunneling current $I_t = 120$ pA. The height of the step is shown in the inset. (d) Temperature dependence of the dc magnetization of Fe₄GeTe₂ in zero fields and field cooled state taken at $\mu_0 H = 1000$ Oe for H||c. (e) Schematic showing a tip and sample forming a point contact.

4.1 Sample details

High-quality single crystals of Fe_4GeTe_2 were synthesized using the technique of chemical vapor transport where I_2 was used as a transport agent [2]. The stoichiometric mixture of the ingredient elements along with the transport agent, in a molar ratio $\text{Fe}:\text{Ge}:\text{Te} = 4.5:1:2$, in powder form, was sealed in a vacuum-sealed quartz tube and was placed in a two-zone horizontal tube furnace maintained at a source temperature of 750°C and growth temperature of 700°C for one week. As a result, large shiny high-quality single crystals of Fe_4GeTe_2 with lateral dimensions of eight millimeters were procured. The single crystalline phase of the samples was confirmed by room temperature X-ray diffraction (XRD) measurements. Large size ($2\text{ mm} \times 2\text{ mm}$) single crystals of Fe_4GeTe_2 were used for our measurements. Due to the layered structure of the crystals, the samples were cleaved prior to the low-temperature experiments. An atomic resolution image (captured at 77 K) of the Te-terminated surface of one of our crystals is shown in Figure 4.1(b). Such atomic resolution was obtained everywhere on the surface confirming the good surface quality. In Figure 4.1(c) we show a larger area image where a unit cell step of height 1.6 nm is seen. As shown in Figure 4.1 (d), the crystals show a ferromagnetic transition near 300 K . Further discussion on the temperature and magnetic field dependence of magnetization are discussed elsewhere [2].

4.2 Measurement of transport spin polarization

It is important to know the measure of spin polarization at the Fermi surface of the near-room temperature vdW ferromagnet for its use in realistic applications. Using the technique of spin-polarized PCARS [7], we have measured the transport spin polarization of Fe_4GeTe_2 by considering its mesoscopic junctions with conventional superconductors Nb and Pb. We found that Fe_4GeTe_2 is capable of generating a highly spin-polarized transport current owing to a spin-split band structure along with a higher Fermi velocity of the majority spin channel.

4.2.1 PCARS on junctions of Fe_4GeTe_2 with Nb and Pb

In Figure 4.2, we show six representatives normalized Andreev reflection spectra (dI/dV vs. V) captured at 1.6 K on Fe_4GeTe_2 with superconducting Nb tips. One generic feature of all those spectra is a heavily suppressed Andreev reflection [8,9]. Ideally, the conductance enhancement at zero-bias is expected to be 200%, but in the Nb/ Fe_4GeTe_2 , the enhancement is only $\sim 2\%$. We have followed the algorithm discussed in subsection (1.3.4) to determine P_f from the Nb/ Fe_4GeTe_2 Andreev reflection spectra. The black lines over the colored experimental data points in Figure 4.2 shows the best fit to each individual spectrum with the modified BTK theory discussed above. Owing to the high surface quality of the crystal

surface, we could establish ballistic (non-thermal) point contacts free from contact heating-related artifacts. The analysis (Figure 4.4(a)) reveals a very high degree of intrinsic spin polarization (P_t) approaching $\sim 51\%$. As it is usually seen for Nb point contacts, P_t decays with increasing barrier strength Z possibly due to spin-flip scattering at less transparent barriers [10].

To check the reproducibility of such a high value of P_t , we also performed Andreev reflection spectroscopy with Pb tips. The corresponding experimental spectra (color plots) and the modified BTK fits (black lines) are shown in Figure 4.3. Unlike for Nb/Fe₄GeTe₂ junctions, high Z contact was not found for Pb/Fe₄GeTe₂ junctions. However, the analysis of the spectra (Figure 4(a)) for Pb/Fe₄GeTe₂ reveal $P_t \sim 49\%$ for low Z contacts, thereby confirming that the measured high spin polarization is intrinsic to Fe₄GeTe₂. Here it should also be noted that due to the unavailability of a high-temperature elemental superconductor, our measurements were performed below the critical temperature of Nb ($T_c \sim 9$ K) and Pb ($T_c \sim 7.2$ K). It was earlier shown that the transport spin polarization of itinerant ferromagnets varies with temperature in the same way as the bulk magnetization [11]. As it can be seen from Figure 4.1(d), the bulk magnetization does not vary noticeably near room temperature confirming that the transport spin polarization (P_t) of Fe₄GeTe₂ is approximately 50% up to such temperatures.

4.2.2 Bandstructure calculations

Now it is important to understand the origin of such a large spin polarization. To shed light on that, we calculated the degree of transport spin polarization of the van der Waals ferromagnet Fe₄GeTe₂ within the first-principles density functional theory as implemented in the Vienna Ab-initio Simulation Package (VASP) [12–15]. The wavefunctions are described within the projector augmented wave formalism [16], with 700 eV cutoff for the kinetic energy. The local density approximation [17] is used to describe the exchange-correlation energy and non-local optB86b correlation functional to account for the interlayer van der Waals interactions [18]. We sampled the first Brillouin zone with $17 \times 17 \times 5$ Monkhorst-Pack k -mesh [19] and optimized the crystal structure until the forces were below $1 \text{ meV } \text{\AA}^{-1}$.

Fe-I is covalently bonded to Ge and has a magnetic moment of $1.66 \mu_B$, considerably lower than Fe-II ($2.47 \mu_B$). The weighted average of $2.06 \mu_B/\text{Fe}$ corresponds well with the experimental value of $1.8 \mu_B/\text{Fe}$ [1, 2]. The spin-polarized electronic structure analysis and density of states [Figure 4.4 (b)-(c)] indicate metallic nature, which along with the non-integer magnetic moments, imply the itinerant ferromagnetism. The electronic structure shows several flat bands near the Fermi level, indicating enhanced effective mass, suggesting a strong electron correlation. The states of the majority spin channels near the Fermi level are composed of d_{yz} , d_{z^2} , and d_{xz} orbitals of Fe-I and d_{z^2} of Fe-II hybridized with p orbitals

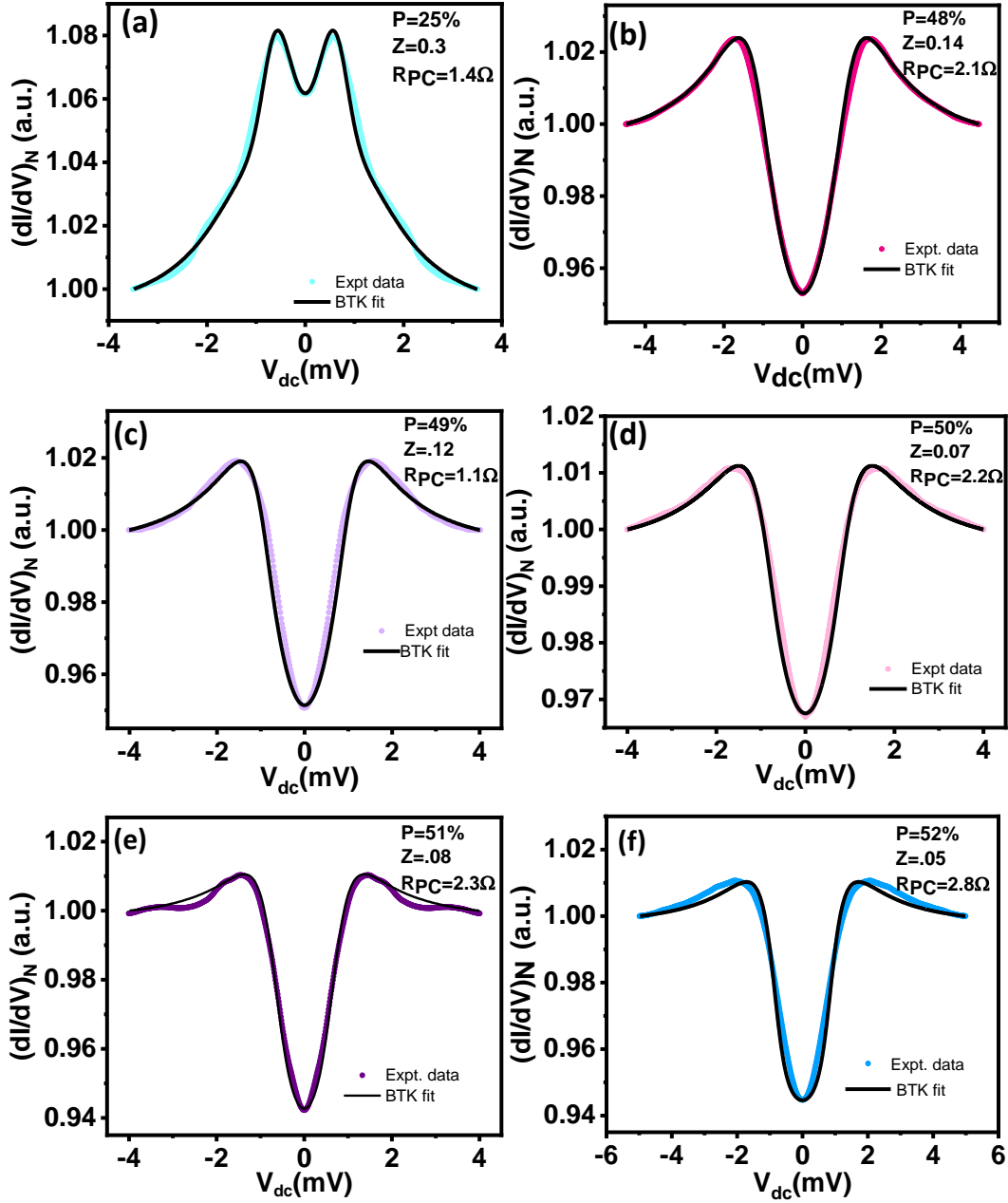


Figure 4.2: (a)-(f) Six fitted ballistic spectra using Nb tip with different values of barrier strength (Z) and spin polarisation (P_I).

of Te. Whereas d_{xy} and $d_{x^2-y^2}$ of Fe-I and d_{z^2} of Fe-II constitute the states for the minority spin channel.

Since Andreev reflection spectroscopy measurements are essentially transport measurements, they are sensitive to the spin polarization at the Fermi energy and not that of the whole spin-polarized bands. In this context, the more relevant quantity is transport spin polarization which essentially gives a direct estimate of the spin-polarized current (the transport spin polarization), a truly relevant quantity for spintronic applications. Within the classical Bloch-Boltzmann transport theory, the transport spin polarization in terms of spin-dependent

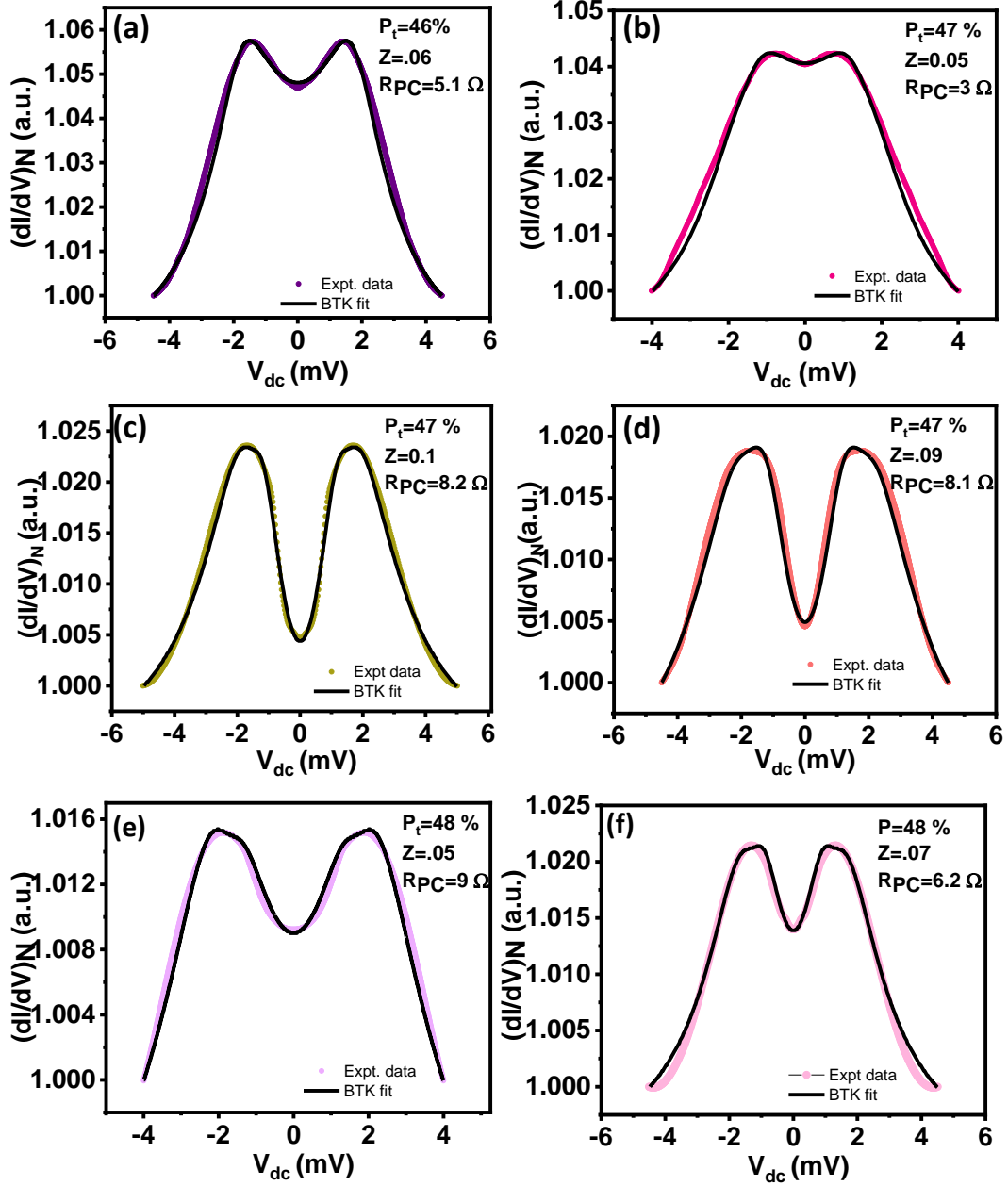


Figure 4.3: (a)-(f) Six fitted ballistic spectra using Pb tip with different values of barrier strength (Z) and spin polarisation (P_t).

currents takes the form [9],

$$P_t^n = \frac{\langle N(E_F)v_F^n \rangle_{\uparrow} - \langle N(E_F)v_F^n \rangle_{\downarrow}}{\langle N(E_F)v_F^n \rangle_{\uparrow} + \langle N(E_F)v_F^n \rangle_{\downarrow}},$$

where v_F is the spin-polarized Fermi velocity. Calculated P_t^n corresponds to the spin-polarization without considering the contribution of the Fermi velocity mismatch between the up and down bands ($(n = 0)$) and the transport spin polarization in the ballistic ($n = 1$) and diffusive ($n = 2$) regimes of transport. We found the average Fermi velocity of the ma-

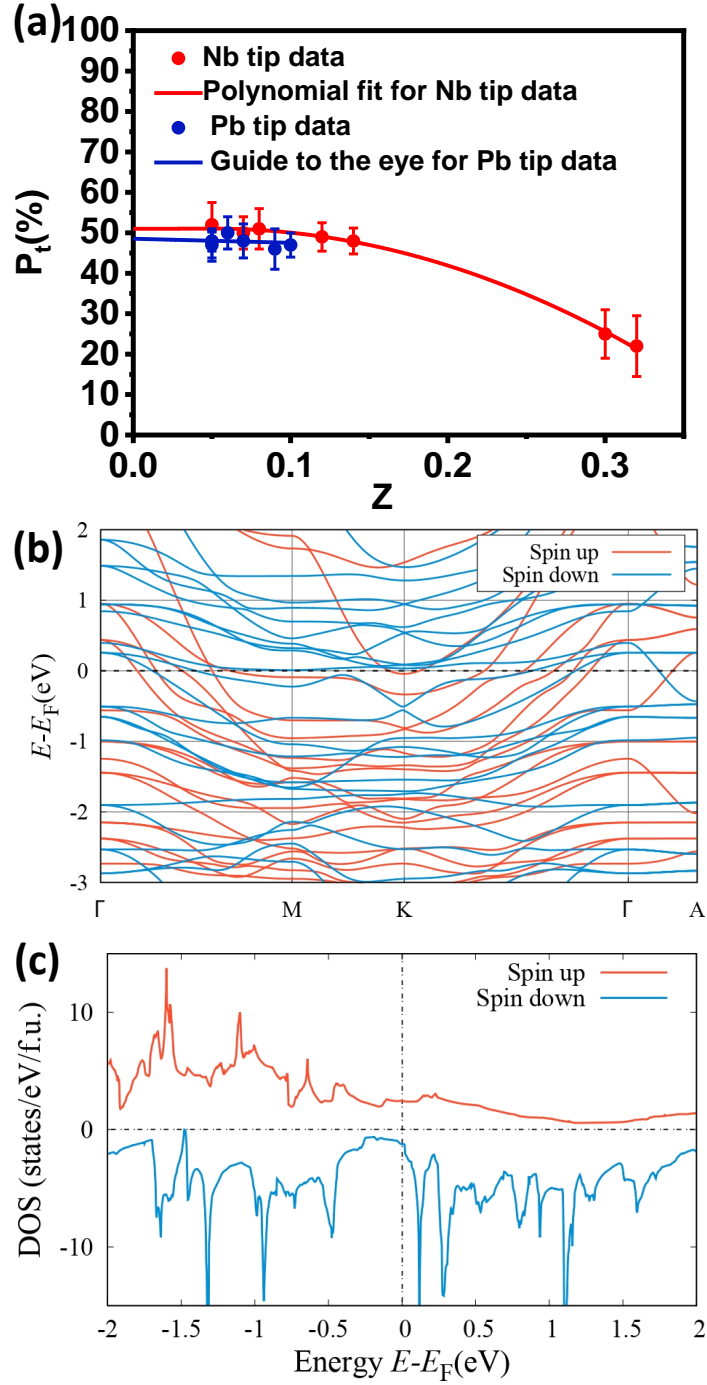


Figure 4.4: (a) P_t vs Z for point contact junctions of Fe_4GeTe_2 with Nb and Pb tips. The error bars depict the range of P_t for which a reasonable fit could be obtained using a modified BTK theory. (b) Spin-polarized band structure and (c) density of states calculated for the ferromagnetic state.

majority spin channels to be $v_{F\uparrow} = 4.37 \times 10^5 \text{ m s}^{-1}$ and a considerably lower value for minority spin channels, $v_{F\downarrow} = 1.88 \times 10^5 \text{ m s}^{-1}$. The calculated spin-polarized density of states at the Fermi level for the majority carriers is $N_{\uparrow} = 2.47 \text{ states/eV/f.u.}$, which is 96% greater than the N_{\downarrow} . This significant imbalance in the Fermi velocities and density of states of the two

channels results in a large value of transport spin polarization (P_t) of 64% in ballistic and 82% in the diffusive regimes.

The comparison of the calculated P_t with our experimental results further confirms that our point contact measurements provided a value near the ballistic limit which is consistent with the ballistic spectral features that we obtained from experiments (Figure 4.2 & 4.3). The minor difference ($\sim 8\%$) can be attributed to the fact that there is no way that the role of the parameter Z can be included in the calculations. A finite Z is unavoidable in experiments and that gives rise to a lower estimate of P_t . In addition, the broad non-linear background of the spectra may include an error in the estimate [20]. The origin of discrepancy can also be due to the presence of flat bands near the Fermi energy that can lead to correlation effects and hence affect the estimate of transport spin polarisation. After considering all the factors, the measured spin polarization exceeding 50% for Fe_4GeTe_2 makes it an extremely important candidate for spintronic applications.

4.3 Emergent Kondo lattice behavior in Fe_4GeTe_2

Specific heat measurements performed on Fe_4GeTe_2 indicated a large effective mass enhancement owing to the high value of the Sommerfeld coefficient ($177.64 \text{ mJ/mol-K}^2$) [2]. In addition, the electronic band structure of the ferromagnet shows several flat bands near the Fermi level, indicating enhanced effective mass, suggesting a strong electron correlation. While Kondo lattice behavior has been reported in Fe_3GeTe_2 through STS, ARPES [21], and PCARS [20] measurements, such reports have not been found in Fe_4GeTe_2 yet. We have shown through PCARS and STS measurements the existence of a heavy fermionic state in Fe_4GeTe_2 .

We conducted temperature-dependent measurements on $\text{Fe}_4\text{GeTe}_2/\text{Nb}$ point contact junctions, as presented in Figure 4.5. The temperature of the junction was gradually increased from the superconducting state of Niobium to its normal state, and we observed the spectral features across a wider bias range, as depicted in Figure 4.5(a). As the temperature approached the normal state of Nb, the magnitude of the dip associated with the superconducting state of Nb at zero bias decreased, and completely disappeared at $\pm 1.5 \text{ mV}$. However, a significant central dip structure persisted even above 9K. Furthermore, the normal state spectra exhibited broad anti-symmetric conductance peaks around $\pm 25 \text{ mV}$. Upon closer examination of the anti-symmetric double-peak structure in the conductance spectra, we identified characteristic features of Fano resonance, indicating the presence of a hybridization gap. According to the two-channel model, these conductance features might arise from the interference between two current paths: one through the channel of itinerant electrons and the other through quasiparticles with a significantly higher mass resulting from the interaction between the spins of d -electrons and itinerant electrons' spins. We then investigated

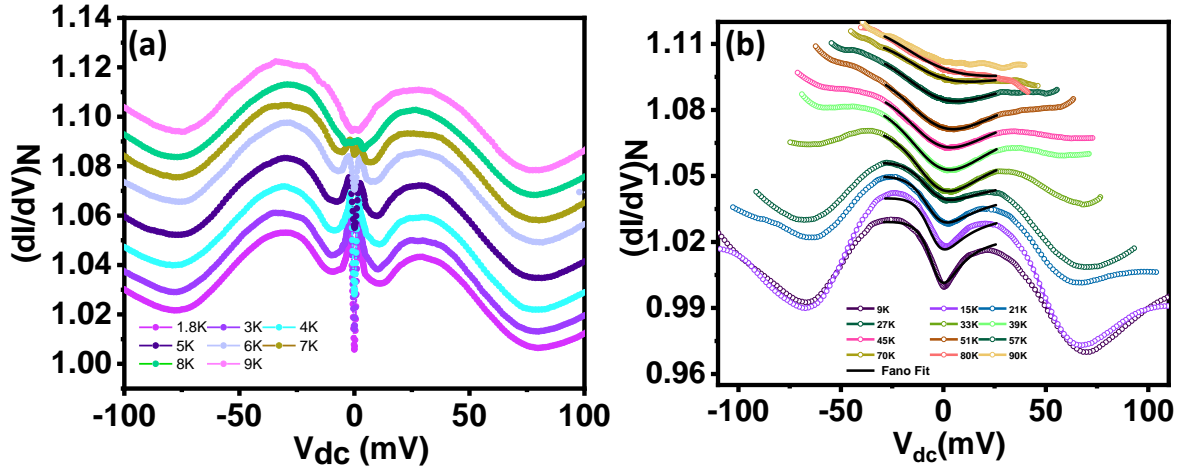


Figure 4.5: (a) The evolution of the conductance spectra, with temperature, obtained for a Fe_4GeTe_2/Nb point contact junctions. A clear anti-symmetric double-peak structure below and above the superconducting transition temperature of Nb can be seen at a higher bias. (b) The temperature evolution of the normal state was obtained for the same point contact junction. The spectra are shifted vertically with respect to the spectrum at the lowest temperature for clarity.

the temperature evolution of the normal state spectrum, as shown in Figure 4.5(b). The double-peak structure gradually diminished as the temperature increased, but the dip at zero bias persisted at high temperatures and became unresolved as the temperature approached 100 K. Similar characteristics have been observed in point contact measurements for other Kondo lattices, such as URu_2Si_2 [24].

In order to further establish the Kondo lattice behavior of Fe_4GeTe_2 , STS measurements were performed on Fe_4GeTe_2 . Prior to the STS measurements, STM topography was performed on the cleaved surface of Fe_4GeTe_2 . The atomically resolved topographic image was obtained using W tip on an area of $10.5 \text{ nm} \times 10.5 \text{ nm}$ at sample bias $V_b = -0.5 \text{ V}$ and tunneling current $I_t = 490 \text{ pA}$, shown in Figure 4.6(a). Two types of triangular defects (bright (marked 1) and dark (marked 2)) were spotted. Such distribution of defects was found in many regions on the surface of Fe_4GeTe_2 . A further theoretical investigation is required to establish the origin of such defects in Fe_4GeTe_2 . To probe the density of states of the defects and defect-free region (marked 3), conductance measurements based on the lock-in modulation technique were performed. Three representative dI/dV spectra obtained on the marked regions are shown in Figure 4.6 (b-d). Two anti-symmetric peaks at $\pm V$ can be seen which are reminiscent of Fano-lineshape. This lineshape serves as a characteristic signature of the presence of Kondo lattice behavior in the system. Such behavior was seen in all three marked regions ruling out the origin of such lineshape due to a single magnetic impurity.

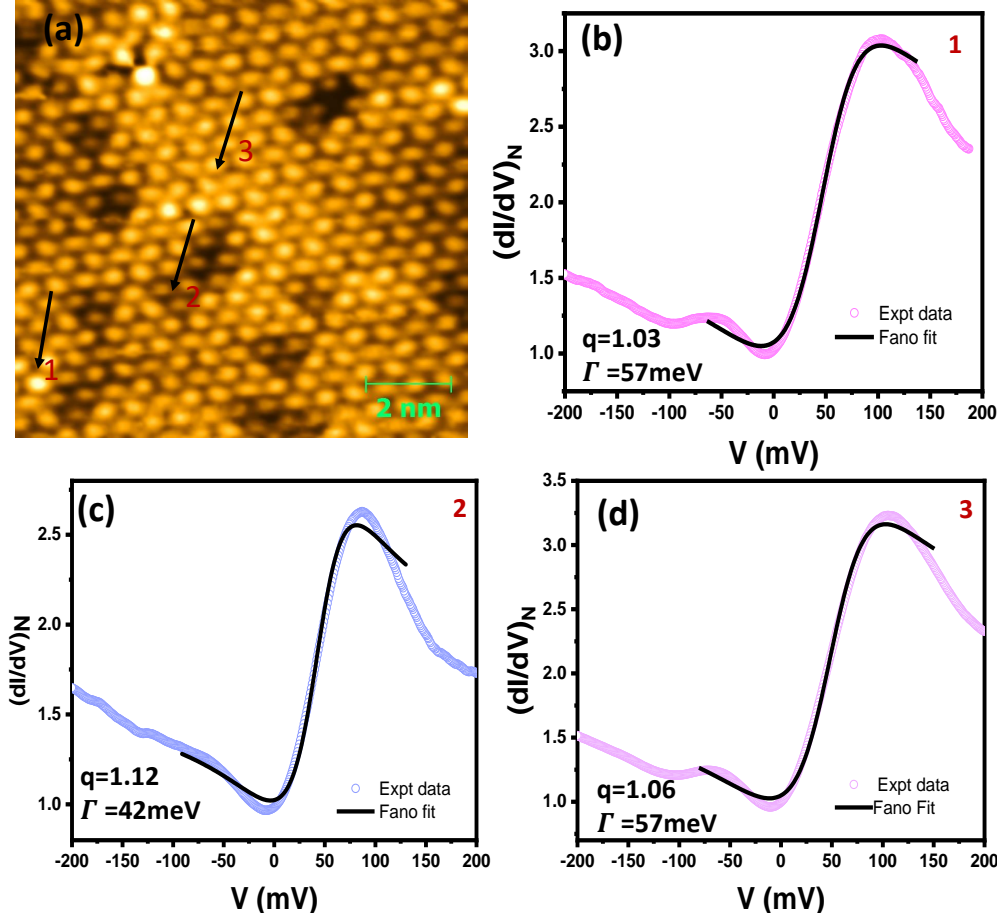


Figure 4.6: (a) STM topograph of area $10.5 \text{ nm} \times 10.5 \text{ nm}$ area taken on the cleaved surface of Fe_4GeTe_2 at sample bias $V_b = -0.5 \text{ V}$ and tunneling current $I_t = 490 \text{ pA}$. Both dark and bright defects can be seen in the topograph. (b)-(d) dI/dV spectra taken at tip positions marked by the black arrows in (a). The spectra fit well with a Fano lineshape.

The line shape was generated using the formula [22]:

$$dI/dV \propto \frac{(\varepsilon + q)^2}{1 + \varepsilon^2}; \varepsilon = \frac{eV - \varepsilon_0}{\Gamma} \quad (4.1)$$

Here, V is the dc bias, q is the asymmetry factor, ε_0 is the position of the resonance in the energy scale, Γ is the resonance at HWHM (half width at half maximum). Such a lineshape in the dI/dV measurements was obtained on other regions of Fe_4GeTe_2 as well. Therefore, the spectroscopic measurements on Fe_4GeTe_2 reveal that it exhibits a Kondo lattice behavior like sister compound Fe_3GeTe_2 .

4.4 Stripes and bubbles

4.4.1 MFM results on Fe_4GeTe_2

To characterize the local magnetic properties in itinerant ferromagnet Fe_4GeTe_2 , temperature-dependent magnetic force microscopy was performed. The measurements were performed in the zero field cooled state and also in the field-cooled state where field cooling was performed in the presence of the stray field of the tip.

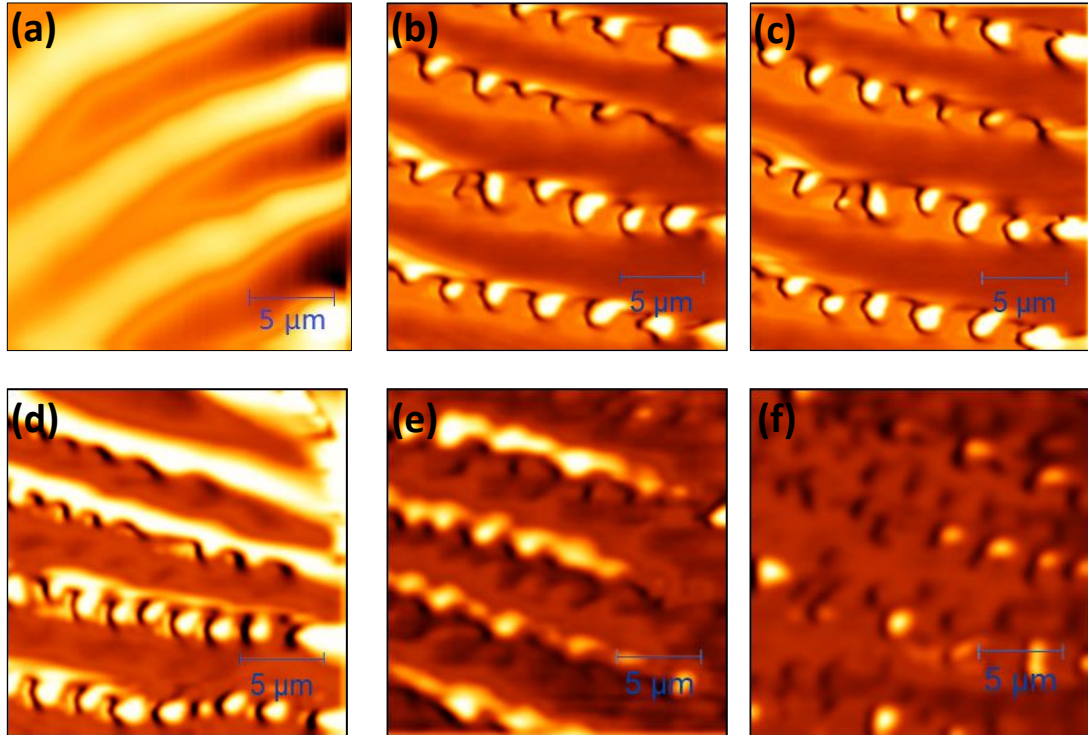


Figure 4.7: MFM dual pass phase images taken on a cleaved single crystal of Fe_4GeTe_2 where (a)-(b) was taken at 70 K in the zero field cooled and field cooled state. (c)-(f) were taken in the field-cooled state at sample temperatures of 80 K, 90 K, 100 K, and 110 K respectively. The field cooling was done in the presence of the stray field of the MFM cantilever.

At a temperature of 70 K in the zero field cooled state, Fe_4GeTe_2 exhibits stripy domains, as depicted in Figure 4.7(a). The width of these domains is approximately $1.5 \mu\text{m}$, which is larger than the stripe width observed in Fe_3GeTe_2 . The ground state domain structure is strongly related to the Dzyaloshinskii-Moriya (DM) term of the microscopic model described in subsection (3.2.1) in the model. If the Hamiltonian contains a DM term having a single direction of the DM vector, then one expects a simple spiral state consisting of domains running parallel to each other, as observed in Figure 4.7(a). The anisotropic DM terms, on the other hand, allow the spirals to orient along any direction and lead to filamen-

tary domains, as seen in Fe_3GeTe_2 in zero field cooled case. To obtain deeper insights into the magnetic state of Fe_4GeTe_2 , we field-cooled the crystal under the field of the cantilever and then performed imaging at 70 K. In this state, the stripes were observed to break into bubble-like structures, forming a lattice with long-range order. Although the lattice of these bubbles bears resemblance to a conventional skyrmion lattice, the individual bubble sizes are much larger, measuring $1.5 \mu\text{m}$. This size is an order of magnitude larger than the typical skyrmion size observed in other systems. The significant bubble size can be attributed to the presence of easy axis anisotropy within the ferromagnetic material, particularly along the c-axis below 110 K. We then gradually increased the temperature and noted that the bubbles began to vanish around 110 K, as illustrated in Figure 4.7 (b-f). This indicates a spin re-orientation transition, leading to a change in the direction of magnetic anisotropy from out-of-plane to in-plane in the ferromagnet.

4.5 Conclusion

In conclusion, we have performed spin-resolved Andreev reflection spectroscopy on the van der Waals ferromagnet Fe_4GeTe_2 using superconducting Nb and Pb tips. The measurements reveal a very high degree of transport spin polarization exceeding 50% in Fe_4GeTe_2 . This result is remarkable as the magnitude of spin polarization is almost two times more than the conventional elemental ferromagnets. The high transport spin polarization along with good metallic character and high Curie temperature of Fe_4GeTe_2 makes the system an important candidate for application in low-power spintronic devices. We have given direct evidence of the presence of Kondo lattice behavior in Fe_4GeTe_2 through STS and PCARS measurements. A field-induced transition from the stripy phase to the magnetic bubbles was imaged through magnetic force microscopy which may be related to the topologically stable magnetic structures, such as the Skyrmions. The measurements establish the richness of Fe_4GeTe_2 making it a unique platform for investigating the interplay between topology, magnetism, and electronic structure.

4.6 Contributions

- **Fe_4GeTe_2 single crystals and Figure 4.1 (d):** Satyabrata Bera, Suman Kalyan Pradhan and Mintu Mondal, School of Physical Sciences, Indian Association for the Cultivation Of Science, Jadavpur, Kolkata-700032.
- **Bandstructure calculations and analysis:** Basavaraja G and Mukul Kabir, Department of Physics, Indian Institute of Science Education and Research (IISER) Pune, PO 411008, India.
- Some parts of the (i) PCAR and MFM measurements were carried out jointly with Monika

Bhakar, Nikhilesh Mehta, and Neeraj Saini, and (ii) the STM measurements were carried out with Mohd. Monish, Department of Physics, Indian Institute of Science Education and Research (IISER) Mohali, PO 140306, India.

Bibliography

- [1] J. Seo, D. Y. Kim, E. S. An, K. Kim, G. Y. Kim, S. Y. Hwang, D. W. Kim, B. G. Jang, H. Kim, G. Eom, S. Y. Seo, R. Stania, M. Muntwiler, J. Lee, K. Watanabe, T. Taniguchi, Y. J. Jo, J. Lee, B. I. Min, M. H. Jo, H. W. Yeom, S. Y. Choi, J. H. Shim, and J. S. Kim, *Science Adv.* **6**, eaay8912 (2020).
- [2] S. Bera, S. K. Pradhan, Md S. Khan, R. Pal, B. Pal, Sk Kalimuddin, A. Bera, B. Das, A. N. Pal, M. Mondal *arXiv:2206.12552v1*.
- [3] S. Mondal, N. Khan, S. M. Mishra, B. Satpati, and P. Mandal *Phys. Rev. B* **93**, 156802 (2004).
- [4] S.R. Kim, I. K. Park, J.-G. Yoo, J. Seo, J.-G. Kim, J.-H. Park, J. S. Kim, K. Kim, G. Lee, and K.-T. Ko, *ACS Appl. Nano Mater* **5**, 1034110347 (2022).
- [5] A. F. May, C. A. Bridges, and M. A. McGuire, *Phys. Rev. Mater.* **3**, 104401 (2019).
- [6] H. Zhang, R. Chen, K. Zhai, X. Chen, L. Caretta, X. Huang, R. V. Chopdekar, J. Cao, J. Sun, J. Yao, R. Birgeneau, and R. Ramesh, *Phys. Rev. B* **102**, 064417 (2020).
- [7] Soulen Jr., R. J.; Byers, J. M.; Osofsky, M. S. ; Nadgorny, B.; Ambrose, T.; Cheng, S.F.; Broussard, P. R.; Tanaka, C. T. ; Nowak, J. ; Moodera, J. S.; Barry, A.; Coey, J.M.D., *Science* **282**, 85 (1998)
- [8] G. E. Blonder, M. Tinkham, and T. M. Klapwijk, *Phys. Rev. B* **25**, 4515 (1982).
- [9] I. I. Mazin, *Phys. Rev. Lett.* **83**, 1427 (1999).
- [10] A. Sirohi, C. K. Singh, G. S. Thakur, P. Saha, S. Gayen, A. Gaurav, S. Jyotsna, Z. Haque, L. C. Gupta, M. Kabir, A. K. Ganguli, and G. Sheet, *App. Phys. Lett.* **108**, 242411 (2016).
- [11] Sourin Mukhopadhyay and Pratap Raychaudhuri *Phys. Rev. B* **75**, 014504 (2007).

- [12] P. Hohenberg and W. Kohn, *Phys. Rev. B* **136**, B864 (1964).
- [13] W. Kohn and L. J. Sham, *Phys. Rev. B* **140**, A1133 (1965).
- [14] G. Kresse and J. Hafner, *Phys. Rev. B* **47**, 558(R) (1993).
- [15] G. Kresse and J. Furthmuller, *Phys. Rev. B*, **54**, 11169(1996).
- [16] P. E. Bloch, *Phys. Rev. B* **50**, 17953 (1994).
- [17] J. P. Perdew and A. Zunger, *Phys. Rev. B* **23**, 5048 (1981).
- [18] J. c. v. Klimeš, D. R. Bowler, and A. Michaelides *Phys. Rev. B*. **83**, 195131 (2011).
- [19] H. J. Monkhorst and J. D. Pack *Phys. Rev. B* **13**, 5188 (1976).
- [20] D. Rana, R. Aswini, G. Basavaraja , C. Patra, S. Howlader, R. R. Chowdhury, M. Kabir, R. P. Singh, and G. Sheet *Phys. Rev. B* **106**, 085120 (2022).
- [21] Y. Zhang, H. Lu, X. Zhu, S. Tan, W. Feng, Q. Liu, W. Zhang, Q. Chen, Y. Liu, X. Luo, D. Xie, L. Luo, Z. Zhang, X. Lai, *Sci. Adv.* **4**, eaao6791 (2018).
- [22] U. Fano, *Phys. Rev.* **124**, 1866 (1961).
- [23] M. Maltseva, M. Dzero, and P. Coleman, *Phys. Rev. Lett.* **103**, 206402(2009).
- [24] W.K. Park, S.M. Narasiwodeyar, E.D. Bauer, P.H. Tobash, R.E. Baumbach,F. Ronning, J.L. Sarrao, J.D. Thompsonban L.H. Greene *Philosophical Magazine* **94**, 3737–3746 (2014).

Tunneling into a weakly coupled array of Majorana wires

The Majorana modes in solid-state systems have the potential to be applied in fault-tolerant quantum computing [1–7]. One of the possible signatures of such modes is the appearance of a zero-bias conductance peak (ZBCP) in tunneling experiments. However, it is known that mere observation of a ZBCP does not provide a solid signature of Majorana-bound states [8–17]. This is mainly because a ZBCP in tunneling spectroscopy involving superconductors can appear in the topological trivial regime as well for a number of non-Majorana sources. Possible topologically trivial sources of ZBCP are Andreev bound states, Kondo effect, and weak antilocalization [18–22]. Only in the topologically non-trivial regime, the ZBCP can be considered a signature of Majorana fermions. This makes ZBCP-based detection of Majorana modes somewhat ambiguous. In this context, we theoretically considered an assembly of Majorana nanowires placed on an *s*-wave superconductor and calculated the tunneling conductance between normal electrodes mounted on the wires and the assembly (array) of the wires [23]. Our key observations are (a) when the number of wires in the assembly is N , and N is even, N conductance peaks symmetric about the bias $V = 0$ appear, (b) when N is odd, a ZBCP, along with the conductance peaks symmetric about $V = 0$ also appears. Hence, in our scheme, simply by changing the number of transport-active wires (e.g., through a mechanical switch or by local top gating) it will be possible to probe the Majorana states unambiguously through controlled appearance and disappearance of the ZBCP by making N odd and even, respectively. In order to find more control parameters to distinguish the topological origins of ZBCP from the non-topological origins, a detailed study of the effect of tilting of the applied external magnetic field on the differential conductance of Majorana arrays for both uncoupled and coupled cases has been presented. A richer phase diagram pertaining to the rotation of the field and other control parameters has been obtained and we have found the possible transport signatures of such a phase diagram.

5.1 The Model

Our model setup is shown schematically in Figure 5.1. The setup consists of an array (in the $x - y$ plane) of N parallel nanowires, lying in close proximity to an s -wave superconductor, with Zeeman field (V_z) applied along the \hat{z} direction. As a consequence of the superconducting proximity effect, a superconducting gap (Δ) is induced in the wires. The model also includes inter-wire tunneling which is facilitated by the underlying superconductor. The Hamiltonian for the system described above can be written as :

$$H = H^{\parallel} + H^{\perp} \quad (5.1)$$

where H^{\parallel} is the Hamiltonian describing intra-wire dynamics while H^{\perp} describes the inter-wire dynamics. In the mean-field approximation, these two Hamiltonians can be expressed as:

$$H^{\parallel} = \sum_{\vec{r}} \left[\Psi_{\vec{r}}^{\dagger} (-\mu \tau^z + \Delta \tau^x - V_z \sigma^z) \Psi_{\vec{r}} + \Psi_{\vec{r}}^{\dagger} \left(-t_x + \frac{i\alpha\sigma^y}{2} \right) \tau^z \Psi_{\vec{r}+\delta_x} + H.c. \right] \quad (5.2)$$

$$H^{\perp} = \sum_{\vec{r}} \left[\Psi_{\vec{r}}^{\dagger} \left(-t_y - \frac{i\beta\sigma^x}{2} \right) \tau^z \Psi_{\vec{r}+\delta_y} + H.c. \right] \quad (5.3)$$

where in the Nambu basis $\Psi_{\vec{r}}^{\dagger} = \{c_{\vec{r}\uparrow}^{\dagger}, c_{\vec{r}\downarrow}^{\dagger}, c_{\vec{r}\downarrow}, -c_{\vec{r}\uparrow}\}$; $c_{\vec{r}\sigma}^{\dagger}$ ($c_{\vec{r}\sigma}$) is the fermionic operator that creates (annihilates) a particle at lattice site $r = \{i, j\}$ with spin σ . δ_x and δ_y represent the nearest neighbour lattice vectors in x and y directions respectively. t_x gives the hopping matrix element along the wires (chosen to be along x), α is the Rashba spin-orbit coupling, μ is the chemical potential, t_y is the weak inter-wire hopping matrix element, β is the weak spin-orbit coupling term between the wires in the transverse direction. It is understood that the effective inter-wire coupling between the wires can be significant only when the distance between the wires is less than a coherence length in the superconductor underneath.

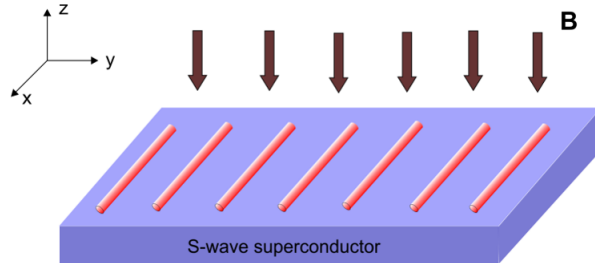


Figure 5.1: (a) Schematic illustrating an array of parallel Rashba nanowires lying in proximity to s -wave superconductor and with Zeeman field V_z applied along z direction.

The Hamiltonian (5.1) can be written in the momentum space as:

$$H = \frac{1}{2} \sum \Psi_k^\dagger h(k) \Psi_k \quad k = (k_x, k_y)$$

$$h(k) = \varepsilon_k \tau^z + \alpha \sin(k_x) \tau^z \sigma^y - V_z \sigma^z + \Delta \tau^x + \beta \sin(k_y) \tau^z \sigma^x \quad (5.4)$$

where $\varepsilon_k = -2t_x \cos(k_x) - 2t_y \cos(k_y) - \mu$, σ and τ are Pauli matrices in spin space and particle-hole basis respectively. The uncoupled wires ($t_y=0$; $\beta=0$) can be tuned into two phases: (a) trivial phase, when $V_z < \sqrt{\Delta^2 + (\mu + 2t_x)^2}$ and (b) topological phase when $V_z > \sqrt{\Delta^2 + (\mu + 2t_x)^2}$. Here, $\mu + 2t_x$ is the chemical potential measured w.r.t. bottom of the conduction band. We have chosen $t_x = t$ as the energy unit for our calculations. Now, the Hamiltonian can be written as:

$$H = \sum_j \int dk_x [\varepsilon_j(k_x) \Psi_{k_x, j}^\dagger \Psi_{k_x, j} + \alpha \sin(k_x) \Psi_{k_x, j}^\dagger \sigma_y \Psi_{k_x, j} - V_z \Psi_{k_x, j}^\dagger \sigma_z \Psi_{k_x, j} + \Delta \Psi_{k_x, j}^\dagger (i \sigma_y) \Psi_{-k_x, j}^\dagger + h.c.] + \sum_j \int dk_x [-t_y \Psi_{k_x, j}^\dagger \Psi_{k_x, j+1} - i \beta \Psi_{k_x, j}^\dagger \sigma_x \Psi_{k_x, j+1} + h.c.] \quad (5.5)$$

where $\varepsilon_j(k_x) = -2t_x \cos(k_x) - \mu$. From this, the spectrum of the system is obtained as :

$$E^2 = V_z^2 + \Delta^2 + \varepsilon_k^2 + |\gamma_k|^2 \pm 2\sqrt{(V_z \Delta)^2 + (V_z^2 + |\gamma_k|^2) \varepsilon_k^2} \quad (5.6)$$

where $\gamma_k = \alpha \sin(k_x) i + \beta \sin(k_y)$.

The energy dispersion as a function of k_x is calculated for the trivial case when $V_z = 0$ for an assembly of five uncoupled (Figure 5.2 (a)) and weakly coupled (Figure 5.2 (c)) wires. For $V_z = 0.85t$ the system is in a topological regime. In this regime, the dispersion of five uncoupled (Figure 5.2 (b)) and weakly coupled wires (Figure 5.2(d)) are also shown. Periodic boundary conditions along x direction and open boundary conditions along y direction are enforced which makes the momentum along x a good quantum number. The results presented in Figure 5.2 are consistent with the earlier calculations on weakly coupled Majorana wires [24].

Figure 5.3 illustrates the variation of the energy spectra with the Zeeman field V_z . Figure 5.3 (a) and (b) show the variation for an assembly of 3 and 4 uncoupled wires respectively while Figure 5.3 (c) and (d) show the variation for an assembly of 3 and 4 weakly coupled wires respectively, in the topological regime. When the wires don't have any inter-wire coupling ($t_y = 0$; $\beta = 0$), as expected, it is seen that for $V_z > \Delta$ ($\Delta = 0.6t$ in this case), we obtain zero energy states indicating the topological regime. When there is non-zero inter-wire coupling ($t_y \neq 0$; $\beta \neq 0$), the spectra get modified due to the mixing of states, and the

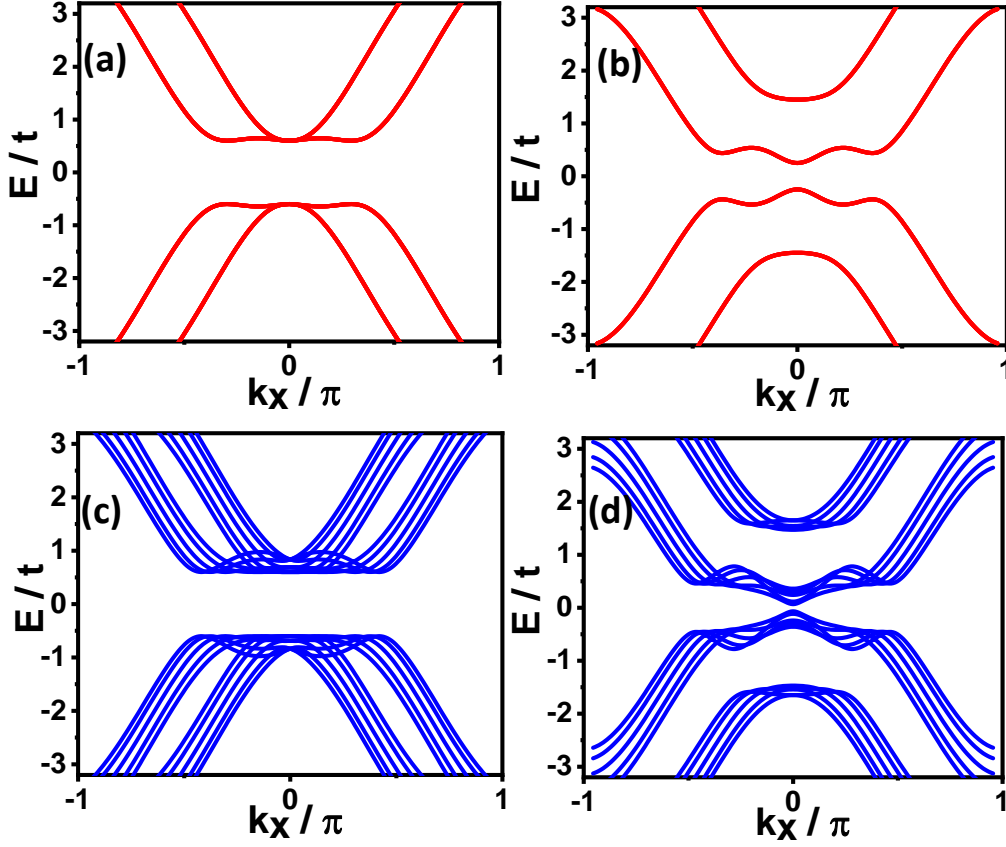


Figure 5.2: Energy dispersion for an assembly of five Majorana wires as a function of the momentum along the wires, (k_x): for uncoupled (in red) (a) trivial regime ($V_z = 0$, $t_y = 0$, $\beta = 0$) (b) topological regime ($V_z = 0.85t$, $t_y = 0$, $\beta = 0$) and coupled (in blue) (c) trivial regime ($V_z = 0$, $t_y = 0.3t$, $\beta = 0.3t$) (d) topological regime ($V_z = 0.85t$, $t_y = 0.3t$, $\beta = 0.3t$) is shown. The other parameters used for calculations are $\alpha = 1 t$, $\mu = -2 t$ and $\Delta = 0.6 t$.

topological regime is achieved for a higher value of Zeeman field ($V_z > 0.75t$ in this case). Furthermore, it is also observed that for 3 wires, states at $E = 0$ appear along with states that emerge at finite energy near zero energy symmetric about $E = 0$. On the other hand, for a 4-wire assembly, no zero energy states can be seen but four peaks around $E = 0$ are seen. We will later see that these lead to an odd-even rule in the conductance which is the focal theme of this article.

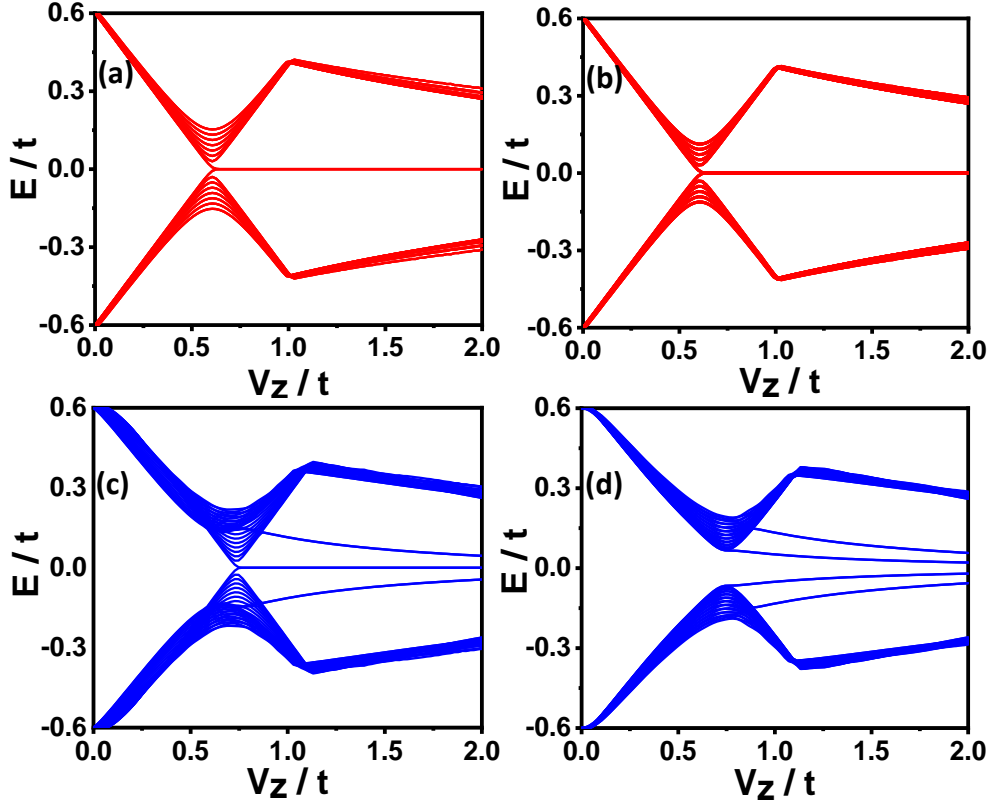


Figure 5.3: Plot of energy spectrum as a function of Zeeman field in the topological regime for : (a), (b) $N= 3$ and 4 uncoupled (in red) wires respectively, both hosting zero energy states beyond $V_z= 0.6t$ (c), (d) $N= 3$ and 4 coupled (in blue) wires where, for $N= 3$, a zero energy state can be seen beyond $V_z > 0.75t$ while no such state appears for $N=4$. The number of states near zero energy is equal to N in both cases. The lowest 48 levels have been plotted. The parameters used for plotting both uncoupled and coupled cases in the topological regime are mentioned in Fig. 5.2.

5.2 Tunneling Conductance

Now, we design a thought tunneling experiment to investigate the possible role of inter-wire coupling in transport through the aforementioned Majorana wire assembly. A schematic representation of the said setup is shown in Figure 5.4 (a). A normal lead is attached to one end of each semi-infinite semiconducting nanowire with strong Rashba coupling proximitized by an s-wave superconductor in the presence of an externally applied magnetic field. The interface between the metal electrode and each wire falls in the tunneling regime of transport. The normal lead has the same Hamiltonian (equation 5.2) as the nanowire except for the superconducting term (Δ). Also, the chemical potential of the normal lead is chosen to be greater than the superconducting gap so that the normal lead remains topologically trivial. The tunnel barrier at the interface of each N - S junction is modeled by adding additional onsite energy of strength $10t$ on one end (left) of each wire. We have assumed semi-infinite nanowires for our calculations to exclude finite-size effects.

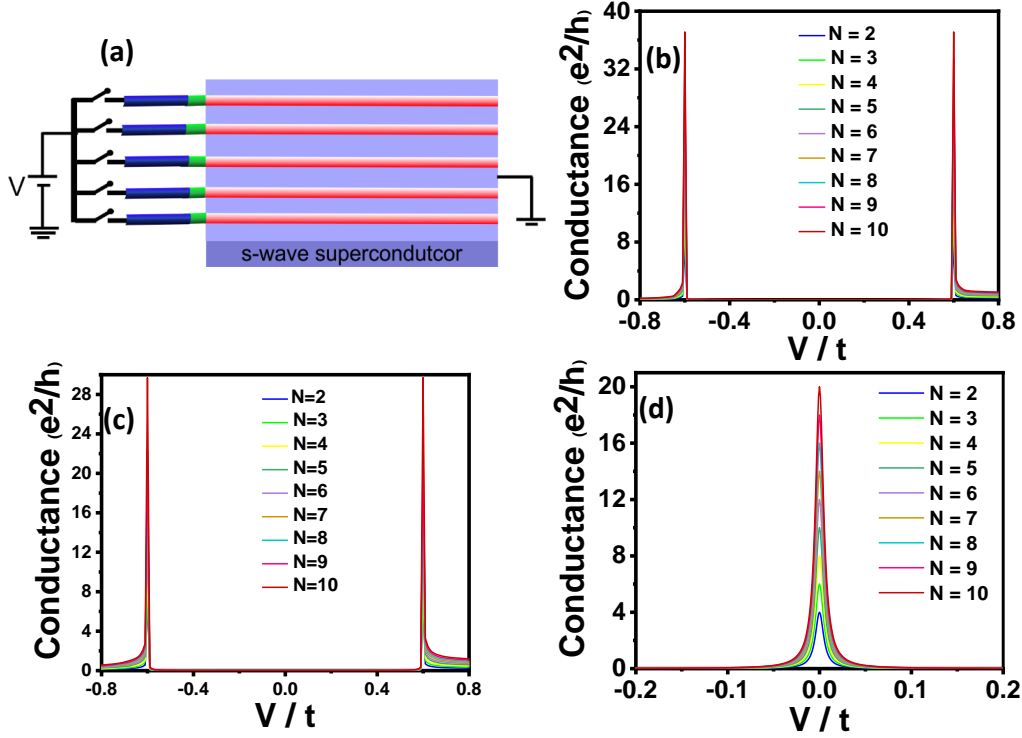


Figure 5.4: (a) Schematic for measuring tunneling conductance of array of Majorana wires. The normal leads (in blue) are connected to Majorana wires (red) with a tunnel barrier (green) at the interface of the junction. A bias V is applied to the normal leads. Using a mechanical switch, the number of transport active wires can be controlled. The plot of zero temperature differential conductance vs applied bias V of a different number of wires for (b) trivial uncoupled case (c) trivial coupled case (d) topological uncoupled case.

The zero-temperature tunneling conductance of the array is calculated using the S -matrix method. By computing the reflection matrix at the N-S junction, tunneling conductance can be found; where the reflection matrix (r) is expressed in terms of electron and hole scattering channels at energy E as :

$$r = \begin{pmatrix} r_{ee} & r_{eh} \\ r_{he} & r_{hh} \end{pmatrix} \quad (5.7)$$

where r_{ee} (r_{eh}) refers to the normal (Andreev) reflection amplitudes. For N conducting channels in the lead the zero temperature differential conductance can be evaluated using the Blonder-Tinkham-Klapwijk (BTK) formula [25] (in the units of e^2/h):

$$G_0(V) = dI/dV = [N - Tr(r_{ee}r_{ee}^\dagger - r_{eh}r_{eh}^\dagger)]_{E=V} \quad (5.8)$$

We have employed KWANT, a numerical transport package in Python, to calculate the components of the reflection matrix [26].

5.2.1 Tunneling conductance of uncoupled wires:

Figure 5.4 (b) shows the differential conductance vs applied bias V when there is no inter-wire coupling in the non-topological (trivial) regime. The differential conductance resembles the zero temperature density of states of a conventional superconductor with coherence peaks appearing at induced superconducting gap energy $\pm\Delta$. As expected, the magnitude of conductance at $\pm\Delta$ increases monotonically with an increase in the number of wires. Figure 5.4 (c) depicts the differential conductance when there is inter-wire coupling in the non-topological (trivial) case for N number of wires. Unlike the trivial uncoupled case, enhancement of magnitude of conductance at $\pm\Delta$ is not monotonic with an increase in the number of wires. Figure 5.4 (d) shows the plot of conductance vs applied bias V for the uncoupled topological phase where each Majorana bound state contributes a conductance of $2e^2/h$ to the total differential conductance. Up to this part, the number of wires only contributes to the overall scaling of the absolute magnitude of the differential conductance. However, more interesting physics emerges when the weak coupling between the wires is also introduced in the topological regime.

5.2.2 Tunneling conductance of weakly coupled wires:

As it can be seen in Figure 5.5, in the topological regime, turning on the weak coupling between the wires has resulted in N conductance peaks, symmetric about bias $V=0$. The most important feature here is the emergence of a ZBCP when N is odd (Figure 5.5 (b), 5.5 (d), 5.5 (f), and 5.5 (h)). On the other hand, for even values of N (Figure 5.5 (a), 5.5 (c), 5.5 (e), 5.5 (g), and 5.5 (i)), ZBCP doesn't appear. This is due to Majoranas at the edges of wires hybridizing into bonding and anti-bonding orbitals when weakly coupled. While, in an even number of cases all the Majoranas are coupled pairwise leading to only satellite peaks in the conductance (around $V=0$), in the case of an odd number of wires one Majorana is left unpaired that contributes a conductance of $2e^2/h$ at zero bias.

5.2.3 Effect of finite temperature and dissipation

From the experimental point of view, it is important to study the effect of finite temperature and dissipation on the conductance of weakly coupled Majorana wire arrays. The finite temperature differential conductance profiles of normal lead- Majorana wire array junction can be calculated by convoluting the zero temperature differential conductance given by equation (5.8) with the derivative of Fermi distribution function $f(E)$ as follows:

$$G(V) = - \int_{-\infty}^{+\infty} dE G_0(E) \frac{df(E-V)}{dE} \quad (5.9)$$

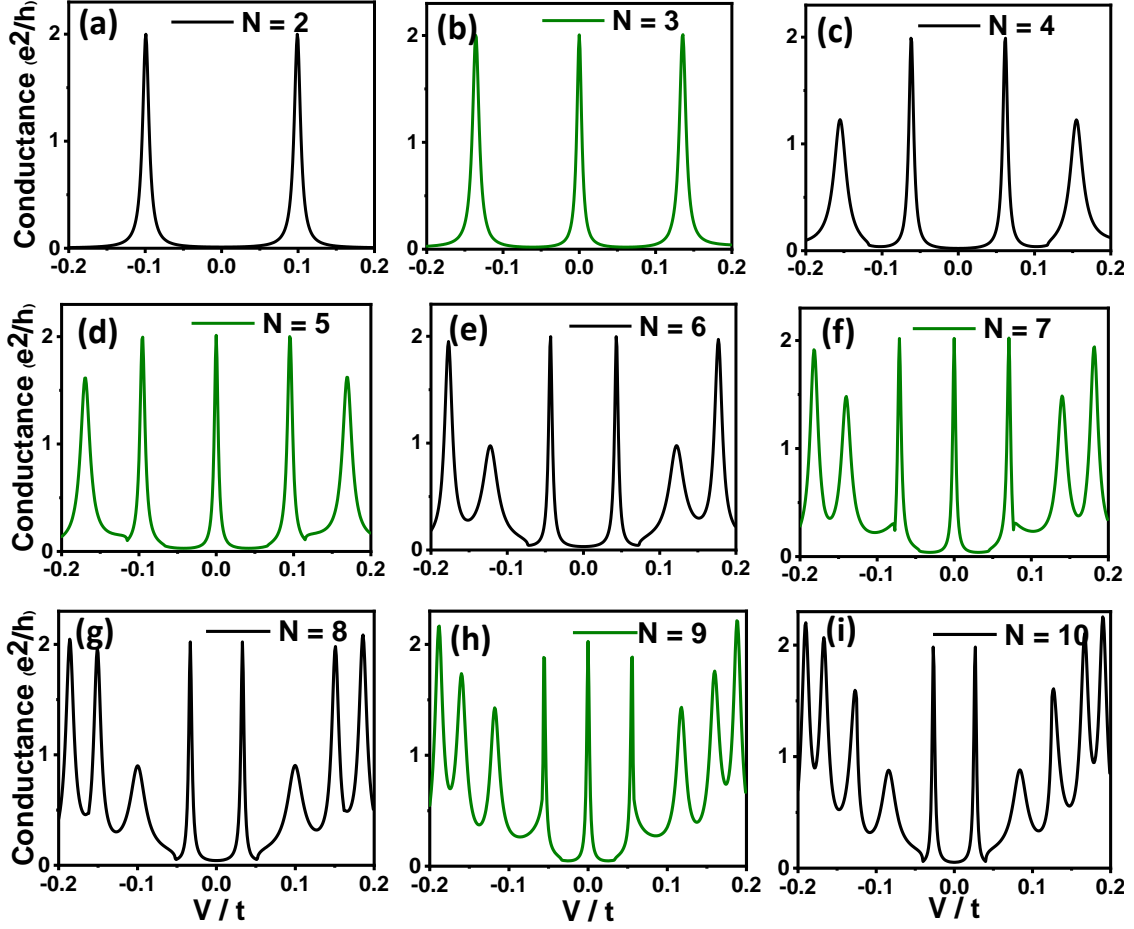


Figure 5.5: Plots of differential conductance vs applied bias for $N = 2$ to 10 weakly coupled Majorana wires in the topological regime ($V_z = 0.85t$; $t_y = 0.3t$; $\beta = 0.3t$) is shown. Plots (b), (d), (f), and (h) show that the ZBCP peak appears only in the case of conductance of an odd number of wires (shown in green) while no such peak is observed at zero bias for the case of (a), (c), (e), (g) and (i) plots depicting the conductance of even number of wires (shown in black).

Results of tunneling conductance of 2 and 3 weakly coupled wires at different temperatures are shown in Figure 5.6 (a) and (b) respectively. It can be seen that an even-odd effect in the differential conductance remains prominent even at finite temperatures making this technique of detecting Majoranas experimentally an efficient one. Temperature plays the role of broadening the finite energy conductance peaks as well as the ZBCP appearing for an odd number of wires. The magnitude of conductance at finite bias as well as at zero bias decreases with an increase in temperature. In addition, the conductance profile becomes almost flat as the temperature becomes equal/greater than the induced gap in the nanowires due to the proximity effect.

Another factor that can lead to the broadening of the conductance profile is dissipation. The possible sources of dissipation in such systems can arise from (a) the formation of vortices in the substrate s -wave superconductor beyond a certain magnitude of Zeeman field,

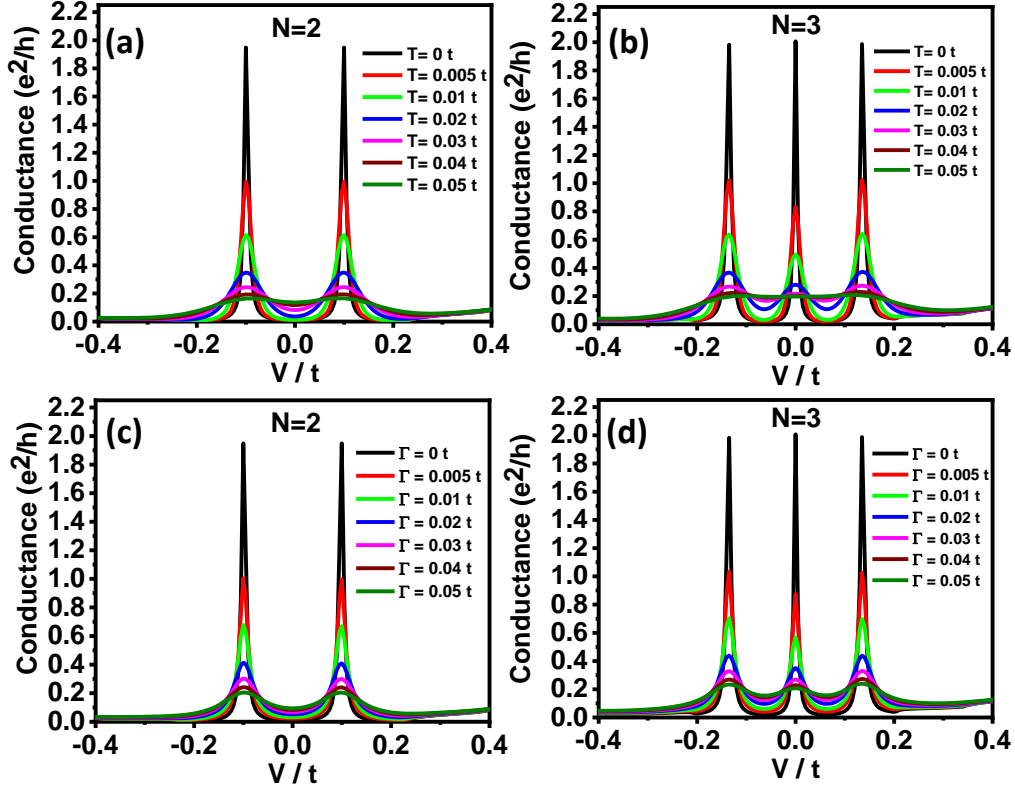


Figure 5.6: (a)-(b) Tunneling conductance of 2 and 3 weakly coupled wires respectively, at different temperatures without any dissipation. (c)-(d) The zero temperature tunneling conductance of 2 and 3 weakly coupled wires respectively, for different values of dissipation.

(b) the presence of disorder in both the semiconducting nanowire and parent superconductor leading to low energy sub-gap states and (c) possibility of inverse proximity effect due to normal lead being coupled to the superconducting nanowire. The dissipation contribution in our system has been modeled, based on previous works [27, 28], phenomenologically by adding an imaginary onsite energy term ($i\Gamma$) to Hamiltonian of the superconducting nanowire given by equation (5.2). The results for tunneling conductance for different values of Γ have been shown in Figure 5.6 (c) and (d) respectively. It should be noted that the role played by dissipation is quantitatively similar to the role of temperature here. In practice, these two effects may not be distinguishable from each other.

5.3 Role of t_y and β in odd-even effect

Now, since we have two additional control parameters (t_y and β) in the problem, it is important to investigate the contribution of each parameter in the conductance measurements in the topological regime. The energy spectrum *vs.* t_y for an assembly of 4 and 5 wires has been shown in Figure 5.7 (a) and (b) respectively for the case when there is no transverse spin-orbit coupling (β) present. Variation of energy spectrum with β by setting inter-wire

hopping (t_y) to zero for the same assembly of wires has been studied in Figure 5.7 (c) and Figure 5.7 (d) respectively. It is evident from the energy spectra in Figure 5.7 that the zero energy state is present at all values of t_y when $\beta = 0$ for even as well as odd numbers of transport active wires. The even-odd effect discussed here originates dominantly from finite β indicating that this parameter plays a vital role in causing effective coupling between the neighboring edge Majoranas of the transport active wires. The same can be verified from the differential conductance maps: (i) as a function of applied bias V and t_y when $\beta = 0$ shown in Figure 5.8 (a)-(b) for 4 and 5 wires respectively and (ii) as a function of applied bias V and β when $t_y = 0$ shown in Figure 5.8(c)-(d) again for 4 and 5 wires respectively. The edge Majoranas are uncoupled when β is close to zero leading to differential conductance nearly equal to $8 e^2/h$ in the case of 4 wires and $10 e^2/h$ in the case of 5 wires. As β is turned on, the effective coupling occurs between the neighboring edge Majoranas leading to four contour lines in the conductance map at finite applied bias V in an array of 4 wires and five in the conductance map of 5 wires out of which four occur at finite energy and one specifically at zero energy with quantized conductance of $2 e^2/h$.

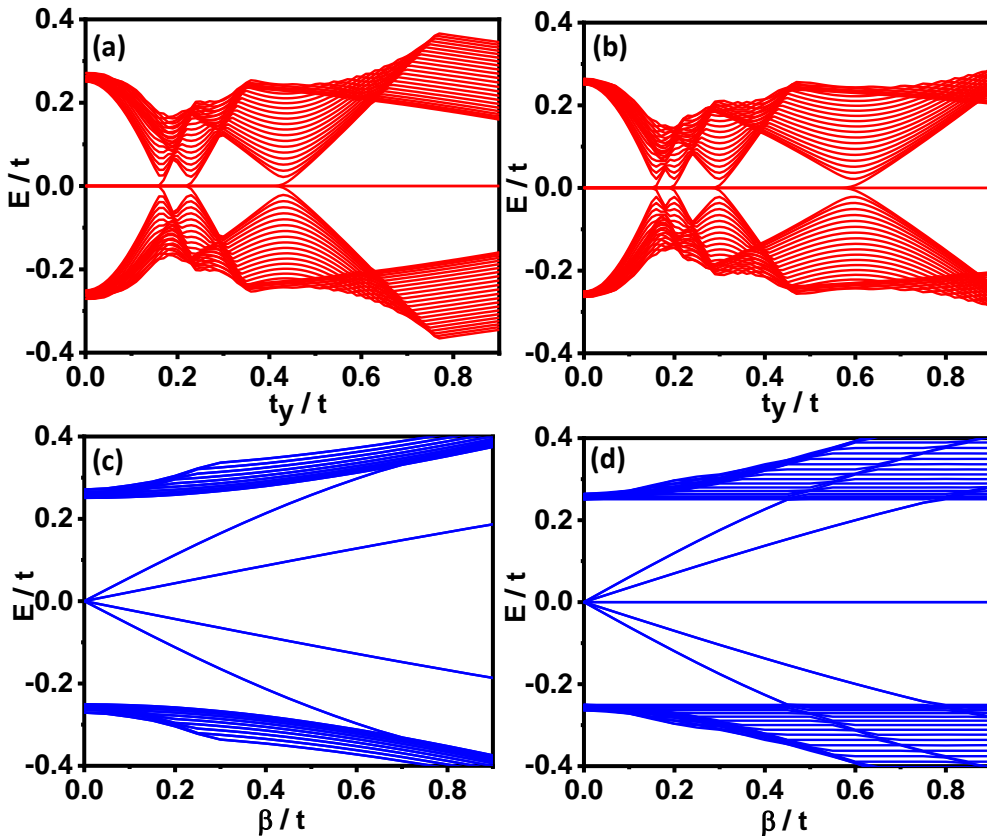


Figure 5.7: Plot of energy spectrum in the topological regime as a function of (a) t_y when $\beta = 0$ for an assembly of 4 wires (b) t_y when $\beta = 0$ for an assembly of 5 wires (c) β when $t_y = 0$ for an assembly of 4 wires (d) β when $t_y = 0$ for an assembly of 5 wires. The lowest 48 levels have been plotted. The even-odd effect can be predominantly seen when β is finite.

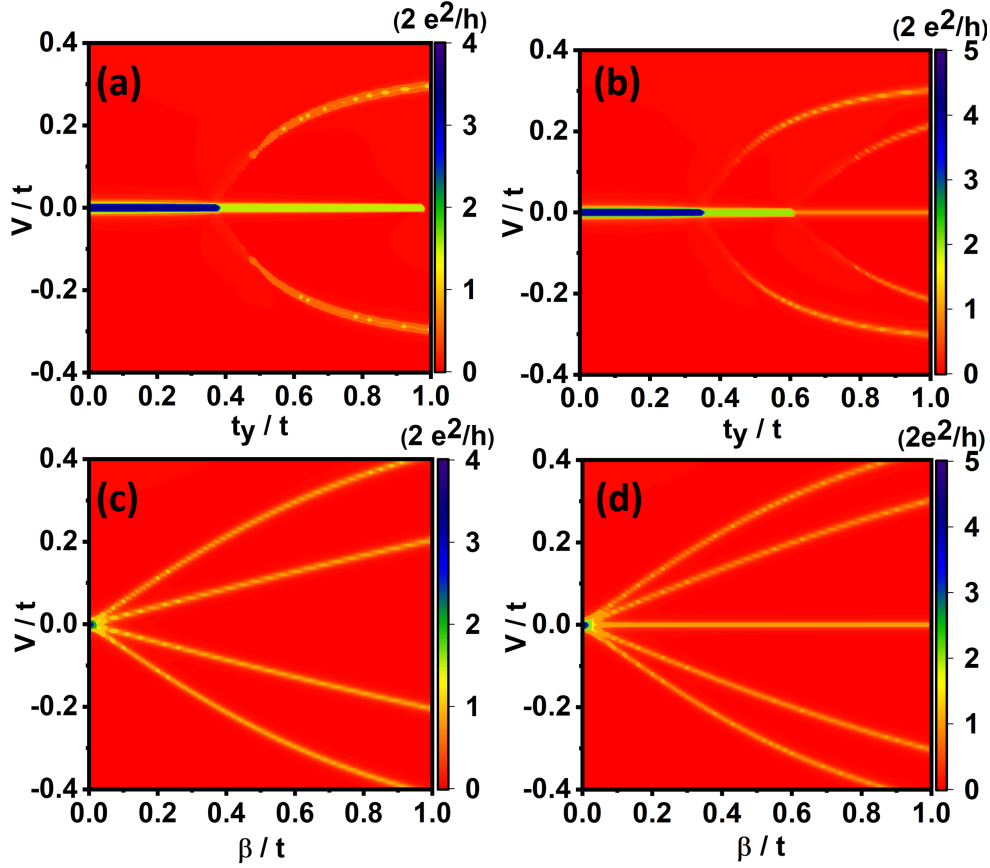


Figure 5.8: The differential conductance, on the color scale, map as a function of (a) t_y when $\beta = 0$ for an assembly of 4 wires (b) t_y when $\beta = 0$ for an assembly of 5 wires (c) β when $t_y = 0$ for an assembly of 4 wires (d) β when $t_y = 0$ for an assembly of 5 wires.

5.4 Relevance of bonding and anti-bonding

As shown in Figure 5.5, when weakly coupled, an odd N of wires allows an unpaired MBS and hence a quantized ZBCP of magnitude $2e^2/h$ as a result, while for an even N the MBSs combine into regular fermion states yielding $N/2$ resonant states below and above the zero-bias point, respectively, as a consequence of the formation of bonding and antibonding states. The formation of the bonding and anti-bonding states in solids can be understood from the simple example described as follows: Let us first consider that there are two states at zero energy and δ is the coupling between these two states. The simple Hamiltonian for such a system can be written as :

$$H = \begin{pmatrix} 0 & \delta \\ \delta & 0 \end{pmatrix} \quad (5.10)$$

The energy eigenvalues of such a Hamiltonian come out to be $\pm\delta$, leading to two finite energy states around zero energy. The same can be calculated for a system with three zero

energy states for which the Hamiltonian can be expressed as :

$$H = \begin{pmatrix} 0 & \delta & 0 \\ \delta & 0 & \delta \\ 0 & \delta & 0 \end{pmatrix} \quad (5.11)$$

Note that the coupling has been allowed for only the nearest neighbor states. Solving equation (5.11) for energy eigenvalues results in three solutions out of which two come at finite energy (one at positive energy and second at negative energy) and one is left at zero energy.

Note that the above explanation of bonding and anti-bonding can't be straightforwardly applied in the present case of weakly coupled Majorana wire. There are two limitations in applying equations 5.10 and 5.11 for coupled Majorana wires. Firstly because the wires are coupled along their entire length, one cannot neglect that there are always $2N$ zero energy states at zero coupling. Secondly, the internal structure is lost. There is clearly a difference between coupling with $\beta=0$ and with $\beta \neq 0$ as can be seen in Figures 5.7 and 5.8. Mathematically this corresponds to a broken symmetry for $\beta \neq 0$. Hence, there is a need to figure out the same understanding in simple terms for Majoranas.

5.5 μ - V_z phase diagram

It is also important to find out in which portion of a larger parameter space, the odd-even argument presented here will be valid. In order to study that, the differential conductance plot with chemical potential (μ) ranging from $-4t$ to $4t$ and external Zeeman field (V_z) ranging from $0.5 t$ to $1.25 t$ has been shown in Figure 5.9 for both uncoupled and weakly coupled assembly of wires. Uncoupled and weakly coupled cases have been studied for both even and odd numbers of wires to find out how the phase diagram changes as the number of transport active wires and coupling changes. In the uncoupled case, for $V_z > \sqrt{\Delta^2 + (\mu + 2t_x)^2}$, the topological regime can be achieved leading to a quantized conductance of $2e^2/h$ per Majorana mode at zero bias. The introduction of transverse coupling (t_y and β) leads to a far richer phase diagram in the $\mu - V_z$ space. For 4 wires (Figure 5.9(c)), we find different regions where ZBCP can appear and these regions are topologically distinct from each other. However, no ZBCP is seen for a range of $|\mu|$ close to $2 t$. This is the range where ZBCP will appear for an odd number of wires. We show a representative phase diagram with 5 weakly coupled wires in Figure 5.9(d). Here, we find that the ZBCP is present in the region around $|\mu|$ close to $2 t$. The results in Figure 5.9 has been shown for the case when $\beta = 0.3 t$ and $t_y = 0.3 t$. The size of the parameter space for which this odd-even effect can be realized increases with the increase in the Zeeman field. Scanning through such a parameter space is experimentally possible as the chemical potential can be tuned by electric gates and the

Zeeman field can be tuned by a superconducting magnet.

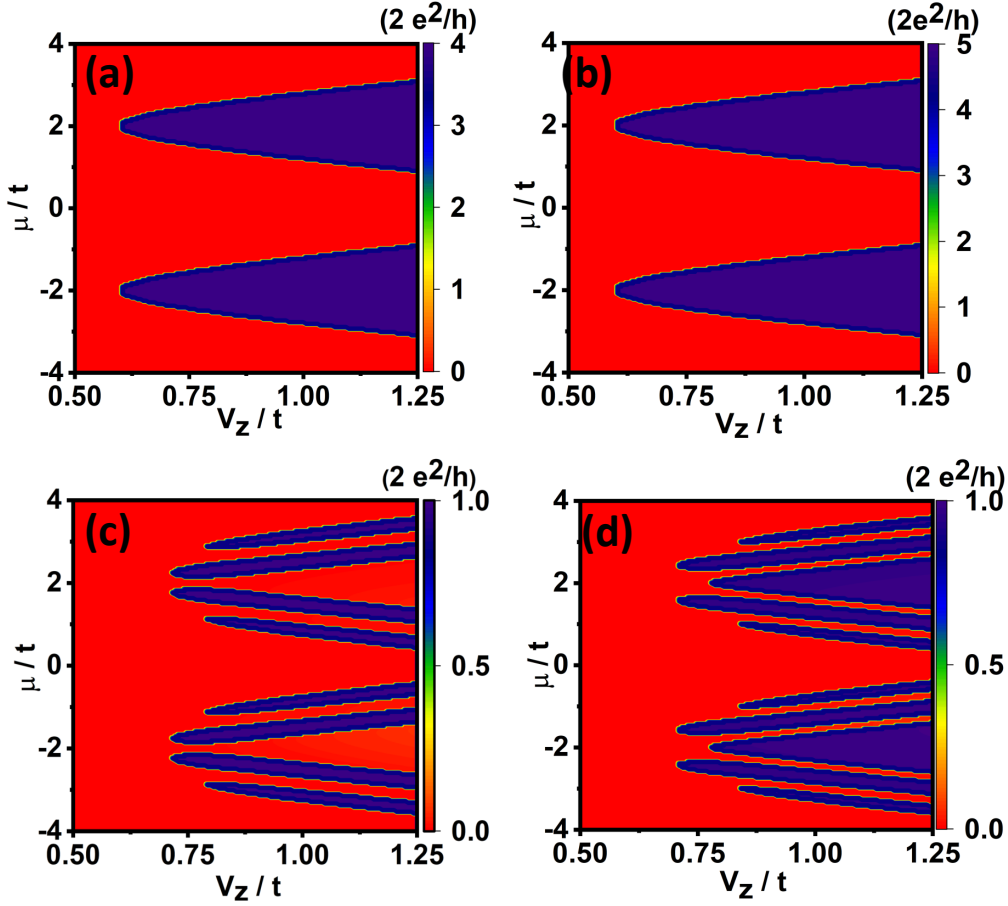


Figure 5.9: The differential conductance at zero bias, on the color scale, map as a function of a chemical potential μ and Zeeman field V_z (a) for an assembly of 4 uncoupled wires (b) for an assembly of 5 uncoupled wires (c) for an assembly of 4 weakly coupled wires (d) for an assembly of 5 weakly coupled wires.

5.6 Effect of tilted magnetic field

Since the odd-even effect studied in Ref. 23 is investigated under a strong magnetic field there are possibilities of magnetic field-induced splitting of localized states in a real system which might give rise to potential ambiguities. In order to understand and address such issues we have investigated the field-angle dependence of the tunneling conductance within the model. To include the effect of the magnetic field the model Hamiltonian in equation (5.1) can be rewritten as

$$H = \sum_{\vec{r}} (\Psi_{\vec{r}}^\dagger (-\mu \tau^z + \Delta \tau^x - \vec{V}_{Zeeman} \cdot \vec{\sigma}) \Psi_{\vec{r}}) + \sum_{\vec{r}} (\Psi_{\vec{r}}^\dagger (-t_x + \frac{i\alpha \sigma^y}{2}) \tau^z \Psi_{\vec{r}+\delta_x} +$$

$$\Psi_{\vec{r}}^\dagger \left(-t_y - \frac{i\beta\sigma^x}{2} \right) \tau^z \Psi_{\vec{r}+\delta_y} + H.c.) \quad (5.12)$$

where $\vec{V}_{Zeeman} = \frac{g\mu_B\vec{B}}{2}$. The external magnetic field B is parametrized in spherical coordinates as, $\vec{B} \cdot \vec{\sigma} = B_x \sin(\theta) \cos(\phi) \sigma_x + B_y \sin(\theta) \sin(\phi) \sigma_y + B_z \cos(\theta) \sigma_z$; θ being the polar angle measured with respect to z -axis and ϕ is the azimuthal angle measured with respect to the x -axis. The magnitude of the magnetic field is taken to be the same in all directions.

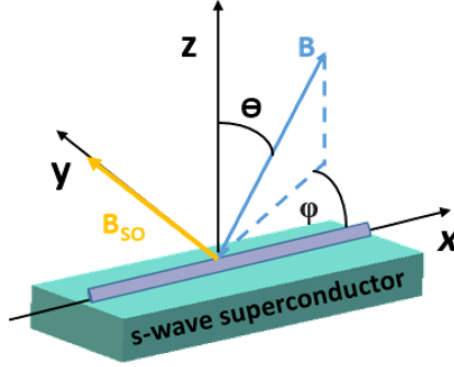


Figure 5.10: Schematic showing a parallel array of semiconducting Rashba spin-orbit coupled nanowires lying in proximity to an s-wave superconductor.

5.6.1 Single nanowire

We start our discussion with the case of a single wire. The schematic of the system along with the chosen set of coordinates is shown in Figure 5.10. Setting the Zeeman field in such a way that the system is in the topological regime, the variation of energy spectrum w.r.t different field orientations is studied. In Figure 5.11(a), the results are shown for energy spectrum versus field angle ϕ when θ is fixed at 90° . It can be seen that when the direction of the applied magnetic field is perpendicular to the effective field that is generated due to spin-orbit coupling, *i.e.* when ϕ is an integer multiple of π (for $\theta = 90^\circ$), a state of topological nature at zero energy exists. Such a state exists till the critical angle (ϕ_c) is reached. ϕ_c depends upon the strength of the induced superconducting gap and the Zeeman field beyond which (even though the condition for the topological non-trivial regime is met) no state at zero energy exists. As per the numerical calculations found in literature [29, 30], ϕ_c can be evaluated using the sine rule or projection rule, given by $\sin \phi_c = \frac{\Delta}{V_{Zeeman}}$. Using the value of $\Delta = 0.6t$ and $V_{Zeeman} = 0.85t$, the critical angle comes out to be 44.5° in our case. It can be shown that the critical angle decreases as the Zeeman field value is increased. We

have also studied the evolution of the energy spectrum w.r.t θ by fixing ϕ at 0° , as shown in Figure 5.11(b). We find that the zero energy state exists for all values of θ . The reason is that for this case the external field is always perpendicular to the spin-orbit field direction. It is evident that for the topological condition to be realized in 1-D wire, the direction of the applied magnetic field should be effectively perpendicular to the field that is generated due to the inter-wire spin-orbit coupling. This effect can be further understood by looking at the energy dispersion of the system.

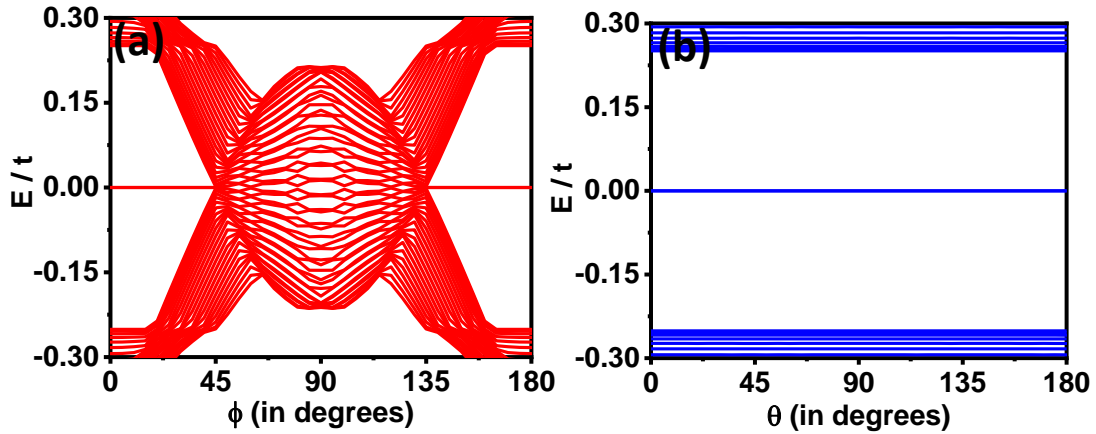


Figure 5.11: (a) The evolution of the energy spectrum with ϕ for V_{Zeeman} being fixed at $0.85t$ and θ being set to 90° is shown. The spectrum is symmetric for positive and negative values of ϕ . (b) The variation of the energy spectrum with θ for V_{Zeeman} being fixed at $0.85t$ and ϕ being set to 0° is shown. A state at zero energy appears for all values of θ . The other parameters used for calculations are $t_x = t$, $\alpha = 1t$, $\mu = -2t$, and $\Delta = 0.6t$.

The energy dispersion for a 1D wire, setting the magnitude of the Zeeman field to $0.85t$, is shown for different orientations of the field in Figure 5.12(a)-(c). When ϕ is 0° , as shown in Figure 5.12(a), the bulk is gapped at zero energy leading to Majorana bound states at the ends of the 1D wire as a consequence of bulk boundary correspondence. It is evident from the dispersion (Figure 5.12(b)) that the bulk energy gap closes partially at $\phi = \phi_c$, where one branch from the positive energy part of the dispersion touches $E = 0$. When ϕ is made equal to 90° , the level crossing can be seen in the energy spectrum (Figure 5.12(c)) resulting in no Majorana at the edges. Setting $\phi = 0$ and varying polar angle θ from 0 to 90° brings no change in the energy dispersion for all values of θ . The energy dispersion comes out to be the same as shown in Figure 5.12(b). From the above results, it is evident that the field angle can be used as another tuning parameter in investigating the topological regime in Majorana nanowires.

All these features of the phase diagram can be captured in field-angle-dependent conductance results. The differential conductance of a single wire has been shown in Figure

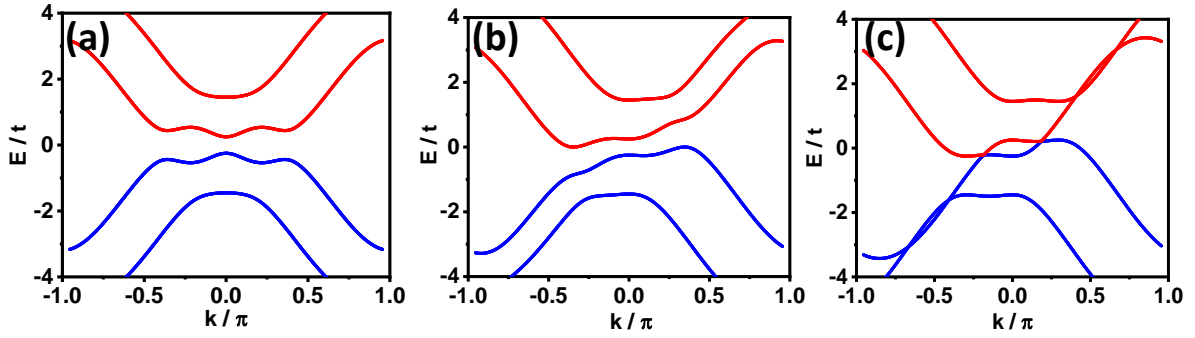


Figure 5.12: (a) The energy dispersion of 1-D nanowire when field angles are $\phi = 0^\circ$ and $\theta = 90^\circ$. The bulk is fully gapped near zero energy. (b) The energy dispersion for critical angle $\phi_c = 44.5^\circ$ when $\theta = 90^\circ$. The gap is partially closed at this orientation, and (c) The energy dispersion for $\phi = 90^\circ$ and $\theta = 90^\circ$. The gap becomes fully closed at zero energy for this orientation of the magnetic field.

5.13 for different orientations of the applied magnetic field. Figures 5.13 (a) and 5.13 (b) are plotted by varying θ while ϕ is fixed at 0. As per expectation from the dispersion results, the zero bias conductance peak remains unchanged in magnitude for all values of θ . Setting the external magnetic field orthogonal to the spin-orbit coupling results in topological phases for all values of θ . Figure 5.13 (c) and (d) are plotted for varying ϕ when θ is fixed at 90° . In this case, the magnitude of the differential conductance at zero energy decreases from the quantized value of $2\frac{e^2}{h}$ as the critical angle is reached and almost becomes zero at $\phi = 90^\circ$. These are all consistent with the observations made earlier by other groups [29, 30]

5.6.2 Array of nanowires

Here we discuss the effect of changing the direction of the magnetic field on the conductance of the arrays. Field-angle dependence of differential conductance for an array of wires without inter-wire coupling (i.e. $t_y = 0; \beta = 0$) has been shown in Figure 5.14. Figures 5.14(a) and (b) show contour plots for differential conductance of 2 and 3 wires respectively as a function of applied bias and the field angle θ when ϕ is fixed at 0° . The zero bias conductance peak shows a constant magnitude of $4\frac{e^2}{h}$ for 2 wires and $6\frac{e^2}{h}$ for 3 wires and so on, for all values of θ . Setting the external magnetic field orthogonal to the spin-orbit direction results in the edge bound states remaining locked at zero energy for all values of θ . The differential conductance vs V spectra with ϕ (θ fixed at 90°) has been shown in Figures 5.14 (c) and 5.14 (d). The magnitude of differential conductance decreases from the quantized value of $4\frac{e^2}{h}$ for 2 wires and $6\frac{e^2}{h}$ for 3 wires as the critical angle, ϕ_c (same as in the case of single wire) is reached and beyond that it almost becomes zero at $\phi = 90^\circ$. Figures 5.14 (e) and 5.14 (f) show the angle dependence of zero bias conductance for N wires where N varies from 2 to 10. It can be concluded from Figure 5.14 that the angle dependence of

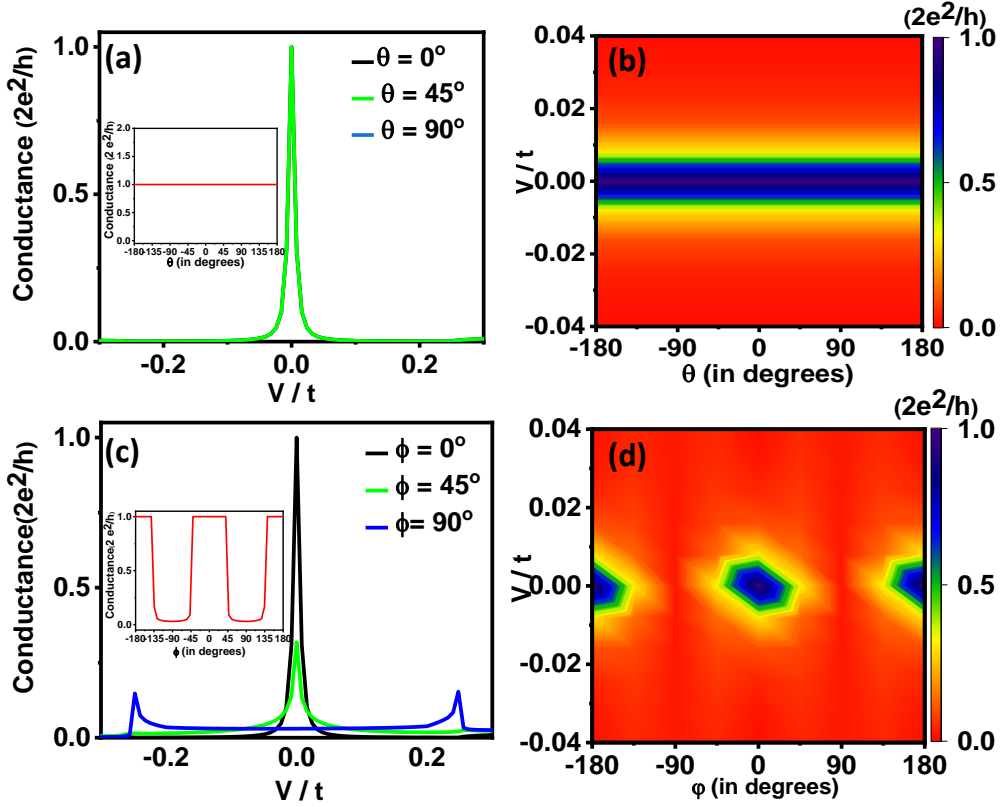


Figure 5.13: (a) The differential conductance (in units of $2\frac{e^2}{h}$) vs applied bias for different values of θ keeping ϕ fixed at 0° . The inset shows that the magnitude of the conductance remains the same for all values of θ . (b) The differential conductance (in the units of $2\frac{e^2}{h}$) of a 1-D nanowire, on the color scale, as a function of applied bias and field angle θ . (c) A plot of differential conductance (in units of $2\frac{e^2}{h}$) vs applied bias for different values of ϕ keeping θ fixed at 90° . The inset shows the variation of differential conductance with respect to field angle ϕ at zero bias. The conductance magnitude decreases from the quantized value of $2\frac{e^2}{h}$ at $\phi=0^\circ$ to nearly zero for $\phi=90^\circ$. (d) The differential conductance (in units of $2\frac{e^2}{h}$) of a 1-D nanowire, on the color scale, as a function of applied bias and ϕ .

differential conductance for uncoupled Majorana wire arrays is the same as in the case of a single wire. The total magnitude of $4\frac{e^2}{h}$ for 2 wires and $N 2\frac{e^2}{h}$ for N number of transport active wires corresponds to each edge Majoranas contributing a conductance of $2\frac{e^2}{h}$ to the total conductance. The observations change dramatically when the weak inter-wire coupling is turned on by setting $t_y = 0.3t$; $\beta = 0.3t$. Figure 5.15 shows the energy spectrum for even and odd numbers of wires for different orientations of the field. Figure 5.15 (a) depicts that the energy spectrum reflects two energy states symmetric about the zero energy for values of ϕ ranging from 0 up to a new critical angle (ϕ'_c) which is around 40° in the weakly coupled case. The energy spectrum, shown in Figure 5.15 (b) has a state at zero energy along with the two states at positive and negative energies for the said values of ϕ when 3 transport active wires are considered. This odd-even effect in the energy spectrum originates from the

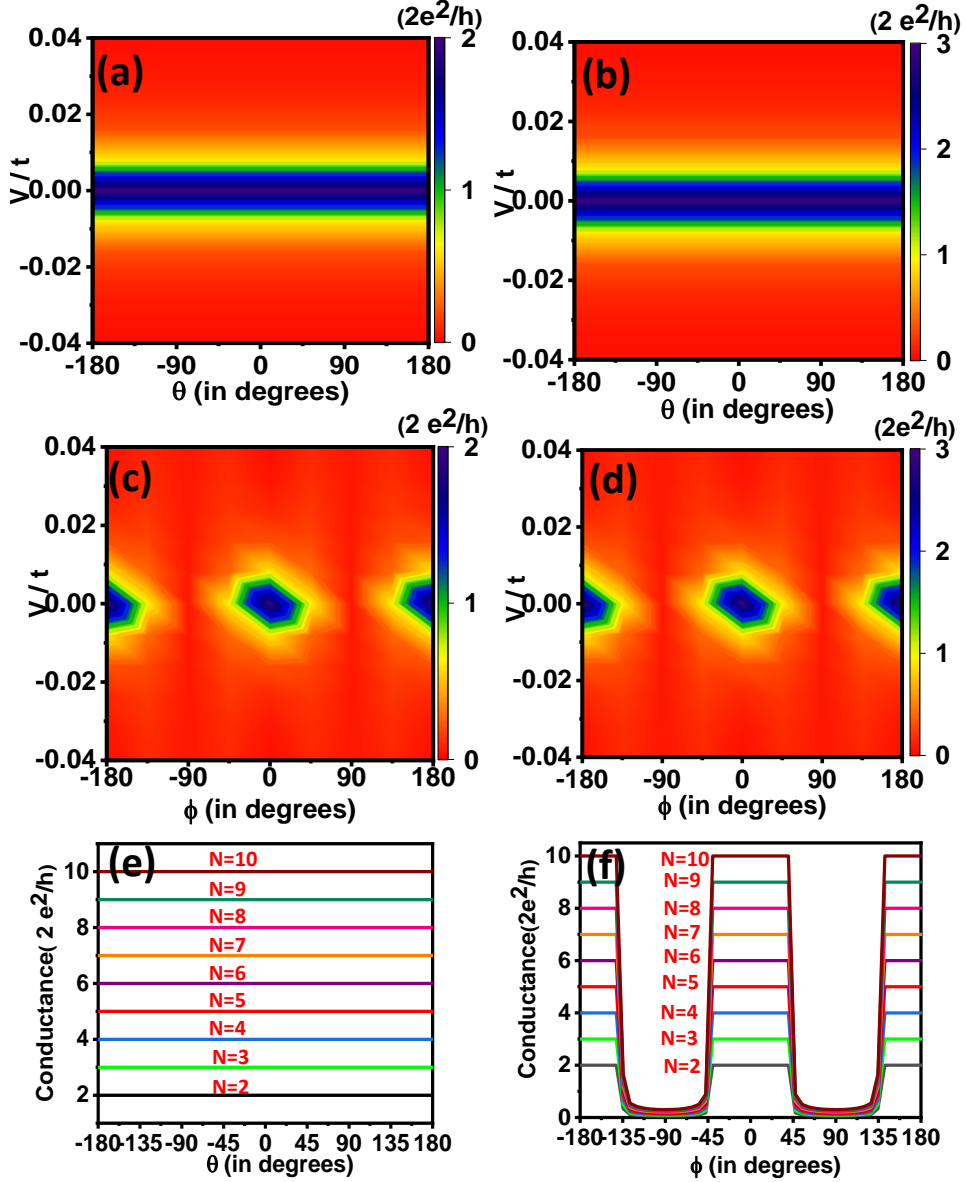


Figure 5.14: (a)-(b) The differential conductance on the color scale, as a function of applied bias and θ for $N=2$ and $N=3$ for uncoupled nanowires respectively. The magnitude of conductance remains constant with variation in θ . (c)-(d) The differential conductance on the color scale, as a function of applied bias and ϕ for $N=2$ and $N=3$ wires respectively. Similar to the conductance of a single wire, the conductance magnitude drops to zero beyond the critical angle with variation in ϕ . (e) Conductance of multiple uncoupled wires at zero bias vs θ and (f) Conductance of multiple uncoupled wires at zero bias vs ϕ . The total conductance of N wires is $2N \frac{e^2}{h}$ at zero bias, for N number of transport active wires, corresponds to each edge Majorana contributing a conductance of $2 \frac{e^2}{h}$.

bonding and antibonding of the end Majoranas upon weak coupling. The physics of bonding and anti-bonding in solids has been discussed in section 5.4. The evolution of the energy spectrum with θ for 2 and 3 wires is shown in Figure 5.15 (c) and (d) respectively.

Figure 5.16 shows the plots of differential conductance vs applied bias for N weakly

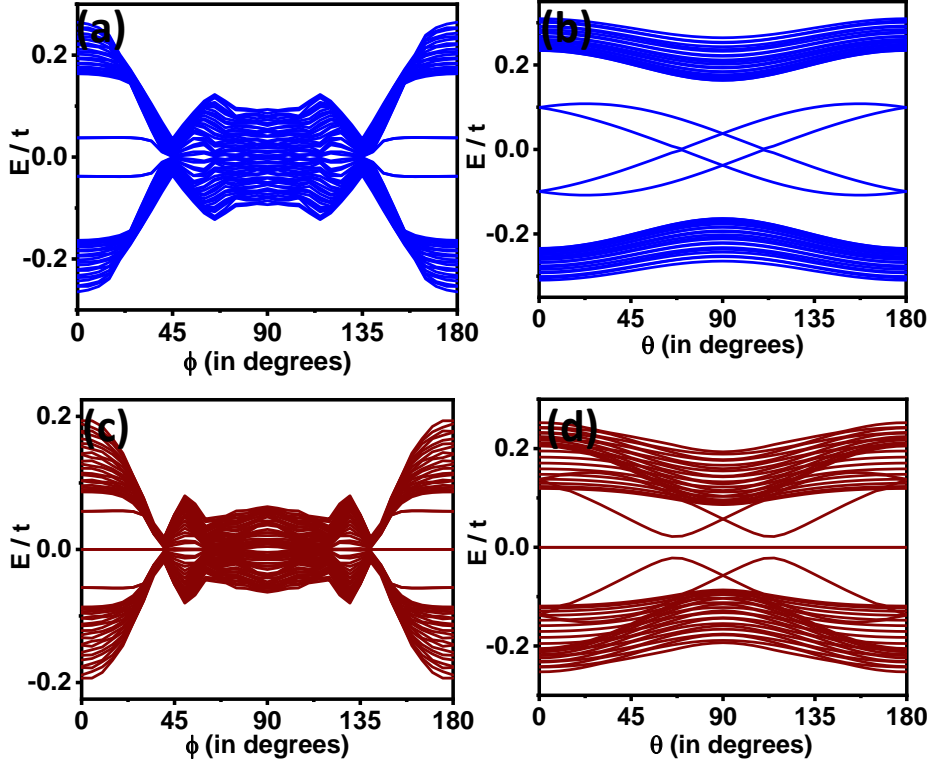


Figure 5.15: The variation of the energy spectrum with ϕ for V_{Zeeman} fixed at $0.85 t$ is shown in (a) and (c) for 2 and 3 wires respectively. It can be seen that a new critical angle exists in the weakly coupled case which is smaller than the critical angle for uncoupled wires. The evolution of the energy spectrum with θ for fixed V_{Zeeman} is shown in (b) and (d) for 2 and 3 wires respectively.

coupled wires (N varying from 2 to 3) for different field angles, specifically 0 , 40° and 90° . First, the results for different values of ϕ (when $\theta = 90^\circ$) have been compared for an even number of wires in Figure 5.16 (a) and for an odd number of wires in Figure 5.16 (b) respectively. Odd-even effect in the conductance can be seen when ϕ is not changed from 0° . The satellite peaks and zero bias peaks amount to the conductance of $2\frac{e^2}{h}$ in this case. The magnitude of both the finite energy peaks in the case of 2 wires and zero bias peak along with finite energy peaks in the case of 3 wires decrease as ϕ approaches ϕ'_c . In addition, the finite energy peak spacing decreases at this angle as can be seen in Figure 5.16 (a). In the case of three wires, since the finite energy peaks exist very close to the zero energy peak, these peaks are not resolved properly and only the zero bias peak with decreased magnitude of conductance can be seen in Figure 5.16 (b) for this orientation. As ϕ is tilted beyond the critical angle the conductance approaches zero in both the even and odd case as shown in Figure 5.16 (a) and 5.16 (b) for $\phi = 90^\circ$. To reiterate, as the critical angle is reached, the bulk gap for the weakly coupled case is partially closed and for $\phi = 90^\circ$, the gap is fully closed with no Majoranas at the edges. Hence, the even-odd effect is not observed at these angles, signifying that this effect can be a solid signature of the presence of Majoranas. To note,

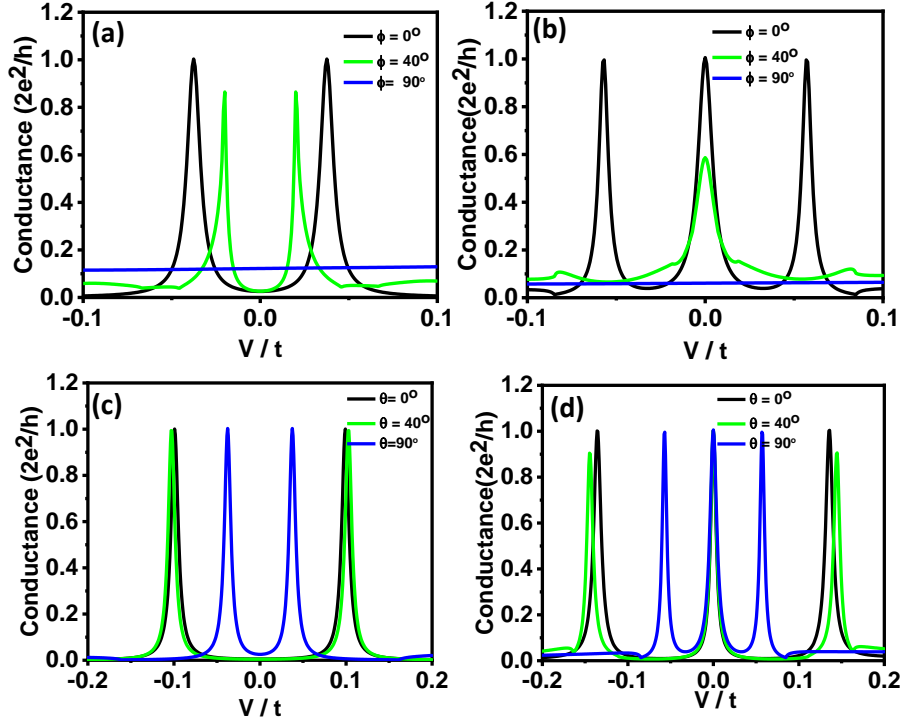


Figure 5.16: The plot of conductance vs the applied bias V for fixed θ and ϕ being set to 0° (shown in black), critical angle 40° (shown in green) and 90° (shown in blue) is presented for 2 and 3 weakly coupled wires in (a) and (b) respectively. For comparison, the variation of the same with fixed ϕ and for θ being set to 0° , 40° , and 90° has been studied for 2 and 3 weakly coupled wires in (c) and (d) respectively. For the weakly coupled regime the parameters used are $t_y = 0.3t$, $\beta = 0.3t$, and the rest of the parameters are the same as mentioned in Figure (1).

such a special field-angle dependence is not expected from non-Majorana sources of ZBCP.

Unlike the above case, the odd-even effect in the conductance can be seen at all the values of θ as shown in Figure 5.16 (c) and (d). However, for $\theta = 90^\circ$ the spacing between the finite energy peaks, symmetric about $V=0$, decreases as N increases. As the number of transport active wires is increased it is possible that for even N , a peak at zero bias may accidentally appear. Such accidental peaks can be differentiated from the ones that appear at zero bias due to unpaired Majoranas in the odd case by checking if they are topologically non-trivial or trivial. Unlike the ZBCP due to Majoranas, the accidental peaks will be sensitive to local perturbations. To get a clearer picture, in Figure 5.17 we show the contour plots illustrating the conductance of N wires (N varying from 2 to 3) as a function of applied bias V and θ and ϕ varying from -180° to $+180^\circ$.

It is now important to study the evolution of differential conductance as a function of tilting angle and other control parameters at zero bias. Figure 5.18 shows contour plots illustrating the variation with respect to inter-wire spin-orbit coupling parameter β ; when inter-wire tunneling t_y is zero for weakly coupled wires in the topological regime. Figures

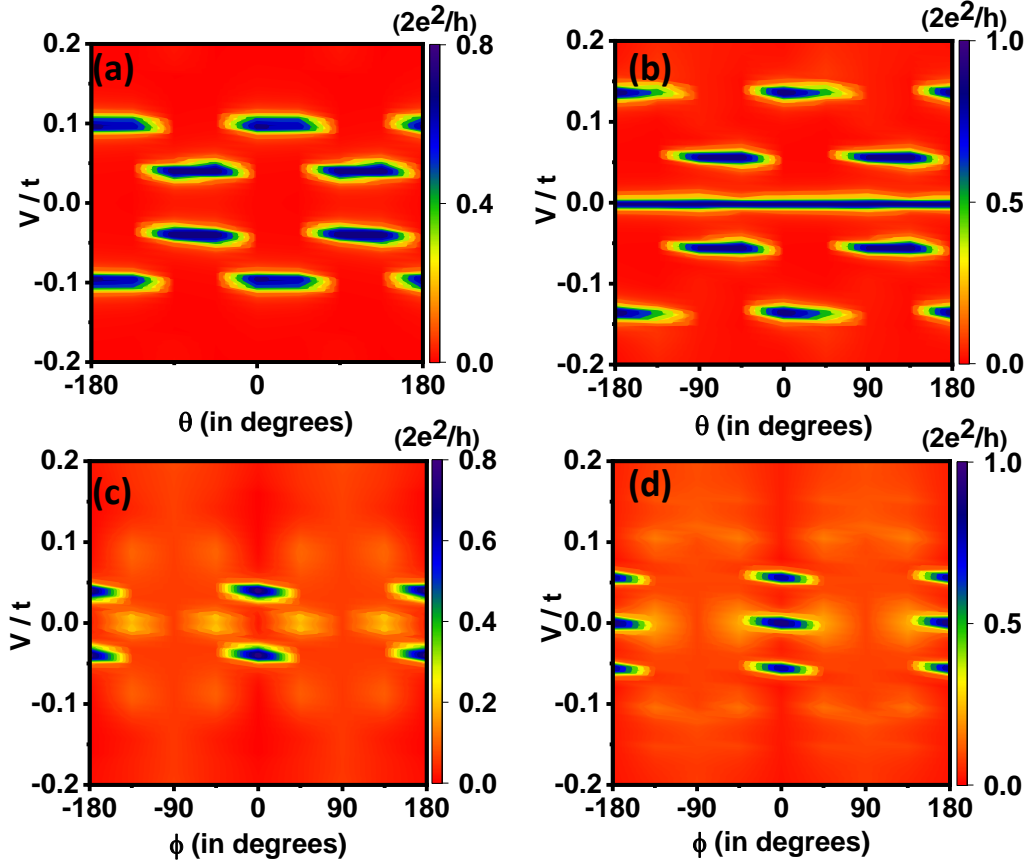


Figure 5.17: (a)-(b) Differential conductance, on the color scale as a function of applied bias and θ for $N=2$ and 3 weakly coupled wires respectively. (c)-(d) Differential conductance, on the color scale as a function of applied bias and ϕ for $N=2$ and 3 weakly coupled wires respectively.

5.18 (a) and 5.18 (b) depict the variation of differential conductance as a function of ϕ and β , when $t_y = 0$ for $N=2$ and 3 wires respectively in the weak coupling limit. Figures 5.18 (c) and 5.18 (d) show the results for the same with variation in θ . As discussed in [23], the wires are uncoupled when β is nearly zero. Non-zero values of conductance can be seen near $\beta = 0$ for ϕ being integral multiples of π . At these values of ϕ , the magnitude of conductance decreases from $4\frac{e^2}{h}$ to zero as β is increased from zero for 2 wires and from $6\frac{e^2}{h}$ to $2\frac{e^2}{h}$ for 3 wires. However, for all values of θ , as the wires are coupled (*i.e.* β becoming non-zero) the conductance drops to zero for both even and odd number of wires.

In Figure 5.19, the results for variation of the conductance spectra as a function of tilt angles (ϕ and θ) and t_y are presented, for the case when β is zero. When θ is set at 90° and ϕ is varied along with t_y , the values of ϕ being equal to the integral multiples of π results in a non-zero value of conductance for t_y less than $0.6t$ for 2 transport active wires, as shown in Figure 5.19 (a). The non-zero value is equal to $4\frac{e^2}{h}$ which is the total conductance when 2 wires are uncoupled. When the number of transport-active wires is three, for the said values of ϕ , the conductance decreases from $6\frac{e^2}{h}$ to $2\frac{e^2}{h}$ as t_y is increased beyond $0.4t$ as depicted in

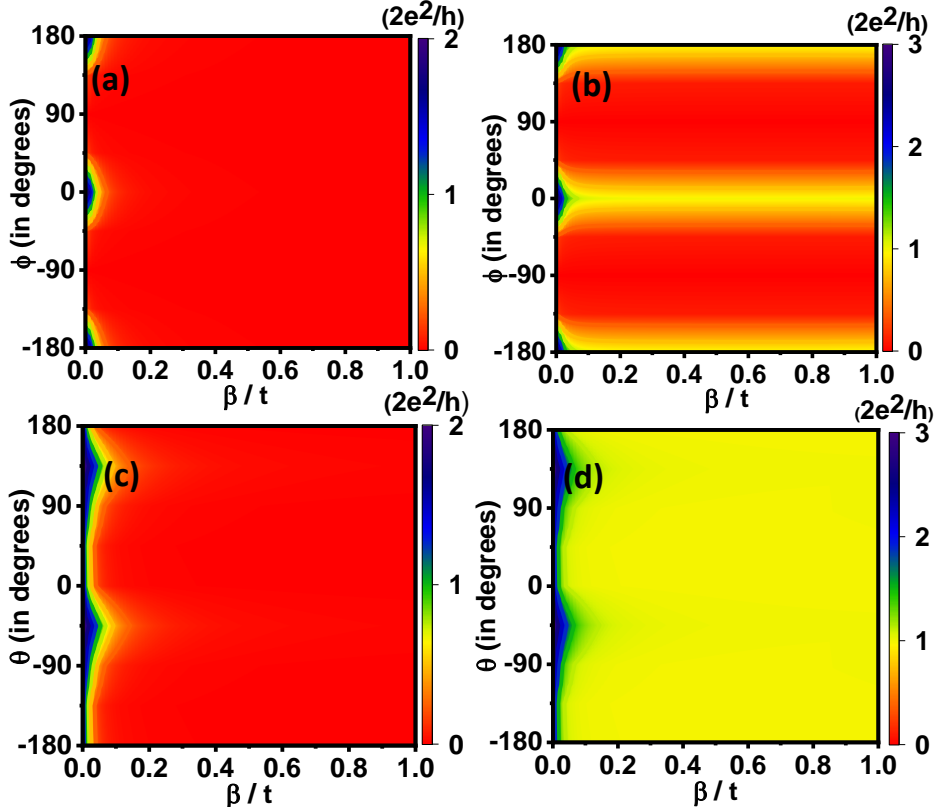


Figure 5.18: (a)-(b) The differential conductance on the color scale, as a function of ϕ and β (when $t_y=0$) for $N=2$ and $N=3$ weakly coupled nanowires respectively. (c)-(d) The differential conductance on the color scale, as a function of θ and β (when $t_y=0$) for $N=2$ and $N=3$ weakly coupled wires respectively. Wires remain uncoupled when β is very small. As β increases the odd-even effect is seen only for certain angles when ϕ is varied keeping θ fixed while for variation with θ , with ϕ fixed, the odd-even effect is prevalent at all values of θ .

Figure 5.19 (b). That shows that as the wires become more coupled i.e. as t_y is increased the even-odd effect becomes more prominent. When ϕ is fixed at 0, the conductance as shown in Figure 5.19 (c) remains at the constant magnitude of $4\frac{e^2}{h}$ for 2 wires for values of t_y less than $0.6t$ and beyond that drops to zero for all θ . This conductance for an odd number of wires decreases from $6\frac{e^2}{h}$ to $2\frac{e^2}{h}$ for all values of θ when t_y is increased beyond $0.4t$ as shown in Figure 5.19 (d).

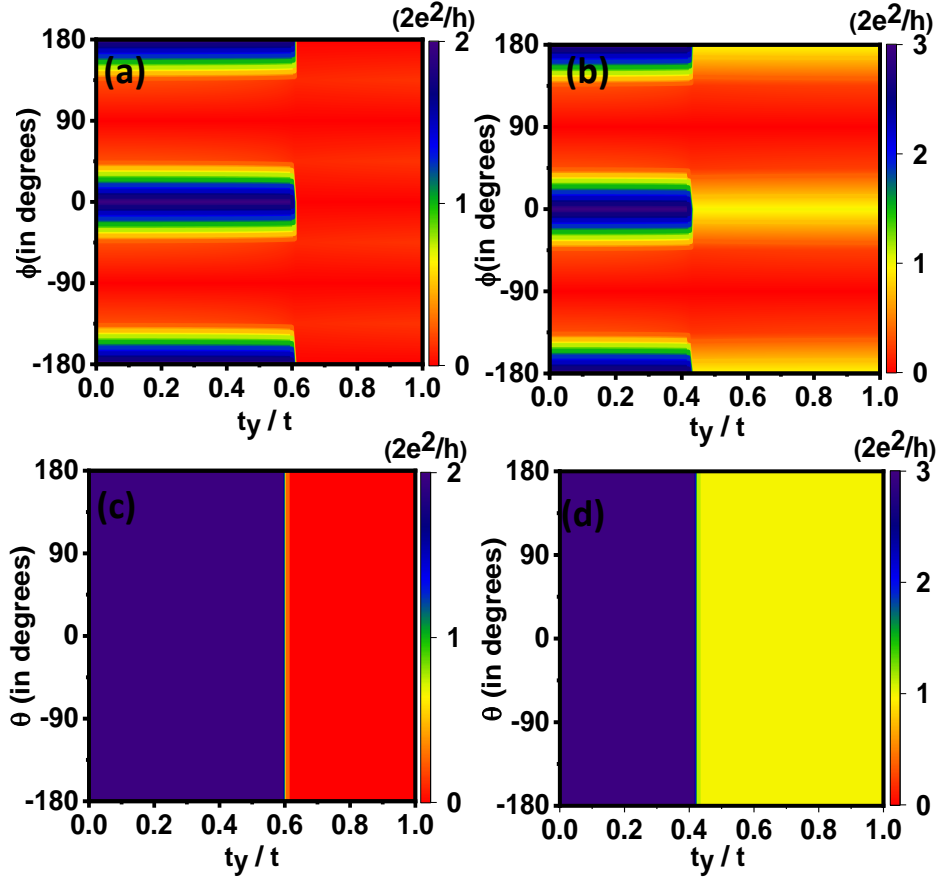


Figure 5.19: (a)-(b) The differential conductance on the color scale, as a function of ϕ and t_y when $\beta=0$ for $N=2$ and $N=3$ weakly coupled nanowires respectively. (c)-(d) The differential conductance on the color scale, as a function of θ and t_y when $\beta=0$ for $N=2$ and $N=3$ weakly coupled wires respectively. An odd-even effect is seen for high values of t_y .

5.7 Conclusion

Therefore, we have presented a scheme where the confirmation of Majorana is not based on the appearance of ZBCP alone, but our calculations provide a detailed protocol based on the number of transport-active nanowires in a single device where depending on whether the number of wires is odd or even, the ZBCP can be switched *ON* or switched *OFF* respectively, in a controlled fashion. We have investigated the effect of tilting of the external magnetic field in and out of the plane of an array of weakly coupled Majorana nanowires. We found a rich phase diagram as a function of tilt angles and other relevant control parameters. The results are important as they can be used to study the tunneling characteristics of the proposed device and identify the origin of the previously observed ZBCP and an odd-even effect of the same from the edge Majorana states vis-a-vis the extrinsic or intrinsic non-topological sources. Hence, the proposed scheme would provide a comprehensive signature of Majorana-bound states and topological superconductivity.

Bibliography

- [1] A. Kitaev, *Annals of Physics* **303**, 2 (2003).
- [2] S. Das Sarma, M. Freedman, and C. Nayak, *Physics Today* **59**, 32 (2006).
- [3] C. Nayak, S. H. Simon, A. Stern, M. Freedman, and S. Das Sarma, *Rev. Mod. Phys.* **80**, 1083 (2008).
- [4] M. Leijnse, and K. Flensberg, *Semicond. Sci. Technol.* **27**, 124003 (2012).
- [5] T.D. Stanescu, and S. Tewari, *J. Phys. Condens. Matter* **25**, 233201 (2013).
- [6] S. R. Elliott, and M. Franz, *Rev. Mod. Phys.* **87**, 137 (2015).
- [7] S. Das Sarma, M. Freedman, and C. Nayak, *Npj Quantum Information* **1**, 15001 (2015).
- [8] R. M. Lutchyn, J. D. Sau, and S. Das Sarma, *Phys. Rev. Lett.* **105**, 077001 (2010).
- [9] Y. Oreg, G. Refael and F. von Oppen, *Phys. Rev. Lett.* **105**, 177002 (2010).
- [10] V. Mourik, K. Zuo, S. M. Frolov, S. R. Plissard, E. P. A. M. Bakkers, and L. P. Kouwenhoven, *Science* **336**, 1003 (2012).
- [11] M. T. Deng, C. L. Yu, G. Y. Huang, M. Larsson, P. Caroff, and H. Q. Xu, *Nano Lett.* **12**, 6414 (2012).
- [12] L. P. Rokhinson, X. Liu, and J. K. Furdyna, *Nat. Phys.* **8**, 795 (2012).
- [13] A. Das, Y. Ronen, Y. Most, Y. Oreg, M. Heiblum and H. Shtrikman, *Nat. Phys.* **8**, 887 (2012).
- [14] A. D. K. Finck, D. J. Van Harlingen, P. K. Mohseni, K. Jung, and X. Li, *Phys. Rev. Lett.* **110**, 126406 (2013).

- [15] H. O. H. Churchill, V. Fatemi, K. Grove-Rasmussen, M. T. Deng, P. Caroff, H. Q. Xu, and C. M. Marcus, *Phys. Rev. B* **87**, 241401 (2013).
- [16] W. Chang, S. M. Albrecht, T. S. Jespersen, F. Kuemmeth, P. Krogstrup, J. Nygrd and C. M. Marcus, *Nat. Nanotechnol.* **10**, 232 (2015).
- [17] J. J. He , J. Wu, T.-P. Choy, X.-J. Liu, Y. Tanaka & K. T. Law, *Nat. Comm.* **5**, 3232 (2014).
- [18] O. A. Awoga, J. Cayao, and A. M. Black-Schaffer, *Phys. Rev. Lett.* **123**, 117001 (2019).
- [19] J. Cayao, E. Prada, P. San-Jose, and R. Aguado, *Phys. Rev. B.* **91**, 024514 (2015).
- [20] C.-X. Liu, J. D. Sau, T. D. Stanescu, and S. Das Sarma, *Phys. Rev. B* **96**, 075161 (2017).
- [21] S. Cho, R. Zhong, J. A. Schneeloch, G. Gu, and N. Mason, *Sci. Rep.* **6**, 21767 (2016).
- [22] D. I. Pikulin, J. P. Dahlhaus, M. Wimmer, H. Schomerus and C.W.J Beenakker, *New J. Phys.* **14**, 125011 (2012).
- [23] D. Rana and G. Sheet, *Journ. of Appl. Phys.* **14**, 131, 084301 (2012).
- [24] C. Qu, M. Gong, Y. Xu, S. Tewari, and C. Zhang, *Phys. Rev. A* **92**, 023621 (2015).
- [25] G. E. Blonder, M. Tinkham, and T. M. Klapwijk, *Phys. Rev. B* **25**, 4515 (1982).
- [26] C. W. Groth, M. Wimmer, A. R. Akhmerov, and X. Waintal, *New J. Phys.* **16**, 063065 (2014).
- [27] C.-X. Liu, J. D. Sau, and S. D. Sarma, *Phys. Rev. B* **95**, 054502 (2017).
- [28] C.-X. Liu, J. D. Sau, T. D. Stanescu, and S. D. Sarma, *Phys. Rev. B* **99**, 024510 (2019).
- [29] S. Rex and A. Sudbø, *Phys. Rev. B* **90**, 115429 (2014).
- [30] J. Osca, D. Ruiz, and L. Serra, *Phys. Rev. B* **89**, 245405 (2014).

Summary

The key accomplishments of the thesis are listed below:

1. The spin-resolved point contact Andreev reflection spectroscopy performed on the mesoscopic junctions of 2-D vdW ferromagnets Fe_3GeTe_2 and Fe_4GeTe_2 with conventional superconductors Nb and Pb revealed a very high degree of transport spin polarization exceeding 50% which is more than the conventional elemental ferromagnets, making them strong candidates for application in all-vdW power-saving spintronic devices.

2. Experimental evidence of emergent Kondo lattice behavior in these ferromagnets demonstrated through point contact and scanning tunneling spectroscopy. The interplay of different quantum orders was investigated.

3. To study the magnetic ground state of Fe_3GeTe_2 and Fe_4GeTe_2 ferromagnetic domain imaging using low-temperature magnetic force microscopy was performed. A field-induced transition from the filamentary/stripy domains to large-size magnetic bubbles was captured. These results were found to be in strong agreement with our theoretical model where we microscopically modeled a triangular lattice itinerant ferromagnet with moderate strength of Rashba SOC and easy-axis magnetic anisotropy.

4. The potential realization of fault-tolerant quantum computing relies on the emergence of Majorana modes in topological superconductors. For a reliable detection method for Majorana modes, we proposed a tunneling setup comprising an array of weakly coupled Majorana nanowires. This setup enables more controlled and effective detection by allowing the manipulation of the presence or absence of a ZBCP based on the parity of the transport active wires. In addition, we investigated the impact of the magnetic field angle on the odd-even effect, which serves as an additional tuning parameter for confirming the Majorana nature of the ZBCP.

6.1 Future Prospects

The discovery of high transport spin polarization in 2-D vdW ferromagnets Fe_3GeTe_2 and Fe_4GeTe_2 opens up new avenues for the development of efficient and power-saving spintronic devices. These materials could be integrated into next-generation spin-based electronics, offering higher performance and energy efficiency compared to conventional ferromagnetic materials. In addition, the spectroscopic signatures of strong correlations in these ferromagnets broaden the limit of ferromagnetic heavy fermionic materials from f- to d-electron systems. Our tunneling setup based on an array of Majorana nanowires, if realized experimentally, can be instrumental in providing a more comprehensive signature of Majorana bound states and topological superconductivity.